Mechanistic and Kinetic Analysis of Anodic Dissolution of Metals (Carbon Steel and Molybdenum) in Solution of Interest by Electrochemical Methods

Thesis submitted in partial fulfillment of the

requirement for the degree of

DOCTOR OF PHILOSOPHY

by

Sayani Adhikari

Roll No. (196107018)

Department of Chemical Engineering

Indian Institute of Technology Guwahati

Guwahati -781039

September 2025

Mechanistic and Kinetic Analysis of Anodic Dissolution of Metals (Carbon Steel and Molybdenum) in Solution of Interest by Electrochemical Methods

Sayani Adhikari

Department of Chemical Engineering
Indian Institute of Technology Guwahati
Guwahati, Assam-781039

STATEMENT

I do hereby declare that the content embodied in this thesis entitled "**Mechanistic and Kinetic Analysis of Anodic Dissolution of Metals (Carbon Steel and Molybdenum) in Solution of Interest by Electrochemical Methods**" is the result of an investigation carried out by me at the Department of Chemical Engineering, Indian Institute of Technology Guwahati, Guwahati, India, under the supervision of **Prof. Prasanna Venkatesh Rajaraman**. In keeping with the general practice of reporting scientific observations, due acknowledgments have been made wherever the work described is based on the findings of other investigators.

Date: **Sayani Adhikari**

Dr. Prasanna Venkatesh Rajaraman
Associate Professor
Department of Chemical Engineering
Indian Institute of Technology Guwahati
Guwahati, Assam-781039, India

CERTIFICATE

This is to certify that the thesis entitled " **Mechanistic and Kinetic Analysis of Anodic Dissolution of Metals (Carbon Steel and Molybdenum) in Solution of Interest by Electrochemical Methods**" submitted by **Sayani Adhikari (Roll No. 196107018)** for the award of the degree of Doctor of Philosophy (Ph.D.), has been carried out under my guidance and supervision. The work documented in this thesis has not been submitted to any other University or Institute for the award of any degree.

Date: **Dr. Prasanna Venkatesh Rajaraman**

Place: Guwahati (Thesis Supervisor)

Dedicated to the Divine Mother,

Mom, Dad, Anil

and Guide

ACKNOWLEDGEMENT

To pursue PhD has been my dream since high school, and turning it into reality is my greatest achievement in my life till now. This journey taught me a lot, which includes both technical and knowledge for life that will help me to move further with my career and also achieve personal goals. It was a period of fluctuating fortunes that broke me several times, but I returned stronger each time. I would never be able to achieve this without the help and support of the precious people in my life. In this moment of triumph, I extend my sincere gratitude to everyone who contributed to the realization of this thesis and the fulfillment of my dream.

First and foremost, I would like to express my sincere gratitude and warmest regards to my supervisor ***Dr. Prasanna Venkatesh Rajaraman***, for imparting the knowledge and guiding me in every possible way. His kindness, politeness, patience, and enthusiasm have motivated me towards the completion of my research work and making this thesis possible. I could not have imagined having a better mentor and supervisor for my Ph.D. journey. It was a great honour to work under him and I will be forever indebted to him for his immense support. I would also like to express my gratefulness to my Doctoral Committee members, ***Prof. G. Pugazhenthi*** (Department of Chemical Engineering), ***Dr. Omkar Deshmukh*** (Department of Chemical Engineering), and ***Dr. Selvaraju Narayansamy*** (Department of Biosciences and Bioengineering) for their priceless time, valuable suggestions and relevant insights throughout my research period.

I express my gratitude to ***Prof. Kaustubha Mohanty***, Head of the Department of Chemical Engineering, for his benevolent support. I am also thankful to the faculty members of the Department of Chemical Engineering, along with other departments of the Indian Institute of Technology Guwahati, for their generousness and assistance. I am also grateful to all the technical staff members of the Department of Chemical Engineering, along with other

departments, for helping me in using the analytical research facilities. I am also thankful to the non-teaching staff of all the departments for their immense help.

I express my gratitude towards IEOT, ONGC, Panvel, Navy Mumbai for providing the financial assistance. I would like to acknowledge the Aries Engineer, Maharashtra, India for metal fabrication. I am also thankful to CSIR-NEIST Jorhat for providing support with XPS analysis. I will also acknowledge ***Dr. Partho Sarathi Gooh Pattader*** (Department of Chemical Engineering) for providing a goniometer to perform contact angle measurements. I am thankful to **Prof. V. Prabhu** for providing equipment support in his lab whenever required.

I sincerely acknowledge Central Workshop, Analytical Lab-Department of Chemical Engineering, and Central Instruments Facility, IIT Guwahati, for providing me with the fabrication and analytical facilities required for my research work.

My heartful thanks and respect to my research family ***Dr. Prince Baranwal, Dr. Apeksha Gupta, Dr. Anusuya Talukdar, Dr. Shravan Kumar, Nikhil Rahul Dhongde, Rushabh Kale, Jeevanantham S, Shaimpu Babu, Vinay Kumar, Rohan Kumar, Mansi Singh, Naveen Kumar, Kunal Gurjar, Murrupurna Anand Kumar***. My deepest gratitude to ***Dr. Barnali Bhui, Dr. Pradeep Sahu, Shekhar Jyoti Pathak, Dr. Roni Mallick, Koushik Jena, Anil Kumar, G. Nagendra Prasad, Deepak Kanumuri, Dr. Arindam Dutta, Jiwajyoti Mahanta***, ***Dr. Shivani Gupta*** for all the care and support. The joyful, friendly, and supportive nature that you all showered in the lab has always helped me carry out my research work smoothly and made my stay memorable.

I would love to acknowledge my best friends in my PhD, ***Dr. Senthil Selvaraju*** and ***Priyanka Mazumder***, who are more of a sibling to me from another mother. It will be less to talk about my parents, my dad***, Prof. Basudam Adhikari,*** and my mom***, Mrs. Jyotsna Adhikari.*** They always stood beside me when I was tired or broken and always supported me throughout. Last,

but not least, I am thankful from the bottom of my heart to the most special person in my life, ***my life partner Mr. Anil K Tripathy***, who always motivated me for my studies and work and has been standing beside me like a pillar throughout.

I thank the divine mother and The Almighty, who has been an invisible support system throughout my life and the source of my positive energy. I thank all the persons in my life whose names have been missed and who have directly or indirectly impacted my life.

Thank You

Sayani Adhikari

ABSTRACT

Oil and gas industries experience failures due to corrosion due to the exposure of the most used material, carbon steel, being exposed to various components such as CO_2, H_2S, NaCl, and volatile fatty acids present in produced water. In spite of the corrosion failures, carbon steel is still used widely because of economic considerations and also a property of the material that the material inhibits corrosion up to some extent from the corrosion product layer. However, due to prolonged exposure and several other factors, loss due to corrosion failure happens. Hence understanding the corrosion mechanism will help to find ways to control and mitigate corrosion.

Semiconductor industries use slurries to planarize materials for microelectronics fabrication. Cu and Ta/TaN have been used conventionally since time, but in the present day, Mo is replacing Cu for interconnect materials due to its suitable properties for semiconductor applications. The planarization process includes oxidizing the metal using a suitable oxidizer, and the oxidized layer is removed by abrasives or a polishing pad. Hence, to achieve the desired planarization designing of the slurry is most important with desired selectivity. To accomplish the desired oxidation, understanding the dissolution mechanism is most important. Several oxidizers are reported for the CMP process of metals, but the dissolution mechanism for Mo has not been explored in detail.

The initial part of the present study is to investigate the dissolution mechanism of Mo in H_2O_2 at alkaline pH. Various electrochemical techniques, such as potentiodynamic polarization and electrochemical impedance spectroscopy, were implemented to study the dissolution mechanism in detail. According to the polarization measurements data obtained, there was no passivation observed in the applied conditions, and active dissolution was observed throughout. Further, the impedance data was acquired at various DC overpotentials, and the EIS data was

further analyzed using electrical equivalent circuit and reaction mechanism analysis. The surface characteristics were also studied using FESEM, and uniform corrosion behavior was observed. The mechanism with three intermediate adsorbates *(Mo^{2+}, Mo^{4+}, Mo^{6+})* and two dissolution paths, including electrochemical and chemical, is proposed to predict the metal surface behavior in an oxidizing medium in the alkaline region. XPS analysis of the corrosion product confirmed the formation of Mo oxides. RMA analysis suggests that the dissolution via the electrochemical reaction pathway is predominant compared to the chemical reaction pathway. Further, the surface coverage of all the intermediate adsorbates is estimated, revealing that oxides of Mo with a +6 oxidation state are mainly occupied on the metal surface. FESEM and XPS measurements substantiated the findings from the RMA analysis.

The second part of the study discusses the dissolution mechanism of Mo in $KMnO_4$ solution under alkaline conditions. If compared with the second part, the etch rate of Mo in $KMnO_4$ was observed to be less than the etch rate of Mo in H_2O_2. However, the polish rate for Mo in $KMnO_4$ was observed to be significantly high. The dissolution mechanism proposed for the H_2O_2 system was used in the $KMnO_4$ system to compare the dissolution behavior of both systems. The potentiodynamic polarization measurements showed a higher rate of change in current density with respect to the potential at higher potential. Through RMA analysis, it was found that the surface coverage was mainly due to Mo (VI) and the surface coverage decreased with an increase in overpotential. FESEM and XPS analysis corroborated with the RMA analysis results.

The third part of the thesis is about comparing the corrosion behavior of various grades of carbon steel in CO_2-H_2S solution at various acetic acid concentrations. Electrochemical techniques and other complementary methods, such as FESEM, contact angle, and XPS measurements, were incorporated to investigate the corrosion behavior of API 5L X52 and X60. The results are evident to suggest that the carbon steel grade strongly influences corrosion

rate as X60 corrodes more than X52 in the system being investigated. The possible mechanism behind the higher corrosion rate observed for X60 is elucidated via analyzing the impedance data acquired at various overpotentials by the reaction mechanism analysis approach. The kinetics of dissolution in the given environment for the carbon steels is also reported. It is observed that X52 possesses higher surface energy due to lower contact angle. This eventually increases the production of corrosion product $FeCO_3$ on the X52 surface. The $FeCO_3$ layer formed on X52 is fine in nature, acts as a protective layer, and decreases the corrosion rate. XPS study confirms a higher fraction of $FeCO_3$ formed on X52.

KEYWORDS: Corrosion, carbon steel, reaction mechanism analysis, acetic acid, carbon dioxide, hydrogen sulphide, anodic dissolution, hydrogen peroxide, molybdenum, chemical mechanical planarization, electrochemical impedance spectroscopy, potentiodynamic polarization.

NOMENCLATURE

English Symbols

C	Capacitance
C_{dl}	Double Layer Capacitance
d	Density
i_{corr}	Corrosion Current or Corrosion Current Density I0
E_{corr}	Corrosion Potential
R	Resistance
R_{ct}	Charge Transfer Resistance
R	Ideal Gas Constant

R_p	Polarization Resistance
R_{sol}	Solution Resistance
T	Temperature
t	Time
Z	Impedance
Z_0	Magnitude of Impedance
Z_F	Faradic Impedance
Z_{Re}	Real Component of Impedance
Z_{Im}	Imaginary Component of Impedance
Z_{total}	Total Impedance z
Z	Impedance

Greek Symbols

α	Transfer Coefficient
β	Tafel Constant
βa	Anodic Tafel Constant
βc	Cathodic Tafel Constant

ABBREVIATION

PP	Potentiodynamic polarization
EIS	Electrochemical impedance spectroscopy
ER	Etch rate
RR	Removal rate
OCP	Open circuit potential
CS	Carbon steel
V	Volt

XPS	X-ray photoelectron spectroscopy
CPE	Constant phase element
EDX	Energy dispersive X-ray
FESEM	Field emission scanning electron microscopy
w.r.t.	With respect to
CR	Corrosion rate
LPR	Linear polarization resistance
ppm	Parts per million
WL	Weight loss
Mo	Molybdenum
EMF	Electro motive force
VFA	Volatile fatty acid
CS	Carbon steel

TABLE OF CONTENT

LIST OF TABLES

LIST OF FIGURES

CHAPTER 1

Chapter I: Introduction

1.1. Background

Corrosion can be defined as the destructive deterioration of metals, usually by electrochemical reaction starting at the surface of the metal. Sometimes corrosion phenomena become an advantage for certain processes like etching for the selective chemical action at the grain boundaries (W Callister Jr and D Rethwisch, 2010). Corrosion is an electrochemical phenomenon, which includes both cathodic and anodic reactions (representing an electrochemical cell). The potential difference results in the formation of localized electrochemical cells where the corroding surface acts as the anode and another area acts as a cathode. This eventually causes the corrosion process to start. Cathodic reactions do not cause any loss to the material, but anodic reactions lead to material loss. The driving force of metallic corrosion is the potential difference between different areas on the metal surface. Corrosion is a day-to-day life problem faced by society in almost every field. The annual cost of corrosion is more than $2.5 trillion worldwide, with India bearing the brunt of costs of about $26.5 billion (Bhaskaran et al. 2014; NACE International 2016). By monitoring the corrosion, this cost can be controlled by avoiding fewer plant failures and losses due to leakage and hence, ensuring the safe functioning of plants. There are several factors affecting the corrosion in various stages of an industrial process. This includes process conditions such as temperature, pressure, flow conditions, and the type of components used. According to an approximate estimation, almost 35 % of corrosion costs can be controlled when appropriate steps are taken (Koch 2017). In addition, being a natural phenomenon, it is impossible to prevent corrosion completely. However, the material can be protected so that the operational time will be increased. Corrosion can also be prevented by several means, such as applying coatings, using corrosion

inhibitors, cathodic protection, etc. (Askari et al. 2018; Xu et al. 2021). To achieve this, a proper understanding of the mechanism and behavior of corrosion of materials in different corrosive environments is required, which can be achieved by investigating the corrosion mechanism of the material (Mars G. Fontana 1987; Ahmed 2006). In studies of metal corrosion, some cases deal with controlled corrosion of materials, such as the chemical mechanical polishing (CMP) process in semiconductor industries. In other instances, the metal is required to be protected from a corrosive environment, e.g., pipeline corrosion in the oil and gas industries. *To cover both types of corrosion cases, the present research work considers the study of metal corrosion in industries belonging to two diverse fields*.

A case of controlled dissolution of metal is observed in the fabrication of integrated circuits in the CMP process. Semiconductors, being an integral part of electronic devices, are facing a significant challenge in the era of miniaturization. The present-day requirement is in the nano-scale range, which makes it more difficult to fabricate the integrated circuits. To reach the requirements, Klaus D. Beyer, in the early 1980s, invented the notion of chemical mechanical planarization (CMP) in IBM (Coetsier et al. 2011). He designed to produce an extremely planarized surface to enable ensuing lithographic imaging without causing significant distortion (Wang et al. 2023a). The CMP is one of the most imperative processes in the semiconductor industry that is necessary to achieve the desired performance of modern microprocessors and memory chips. While fabricating a complicated metal device with a multi-level structure, the difficulties met for non-planarized deposition technology compared to planarization performed using CMP are shown in Figure 1.1. As illustrated in the figure, the non-planarized structure is uneven and unorganized, but the planarized surface is well organized and has an overall uniform desired structure (Seo and Lee 2005). The CMP process involves both physical and chemical actions in the removal of materials.

Physical action is achieved using abrasives and the relative velocity between the surface and polishing pad, in which slurry is distributed with the applied load on the surface being polished. In contrast, chemical action is done using oxidizers and other additives. Metal polishing occurs via metal dissolution, which is an electrochemical phenomenon in the presence of an oxidizer and other chemical additives. Understanding the dissolution behavior of metals in the presence of these chemicals will help to understand the slurry chemistry well. This will eventually aid in formulating the slurry for the CMP of metals to achieve desirable results (Steigerwald et al. 1997).

The miniaturization of electronic devices demands continuous development of advanced materials for interconnects and barrier layers. Molybdenum is a promising candidate for metal interconnects replacing Cu due to its excellent properties, such as high melting point, low bulk resistivity, etc. (Qu et al. 2017). Further, Mo is used in various other applications such as solar cells, thin film in VLSI technology, TFT drivers and switches, which also require polishing of the metal (Seo et al. 2009; Jubault et al. 2011; Feng et al. 2014; Yang et al. 2018). Hence, we focused on the dissolution of Mo in the presence of different oxidisers in alkaline conditions.

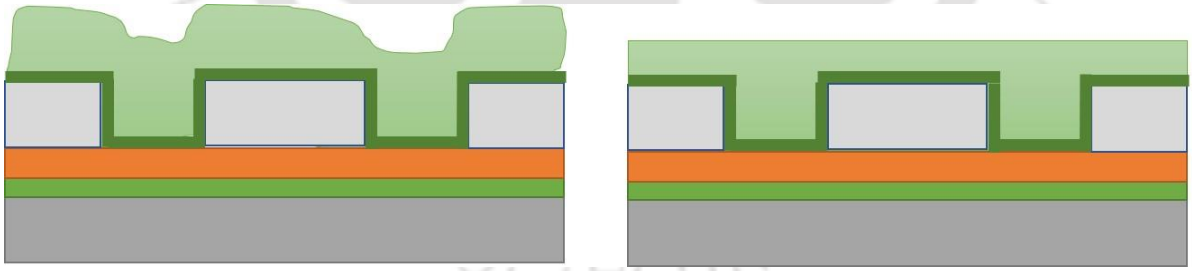

Figure 1.1 Schematic representation of fabrication with (A) without CMP and (B) with CMP

Another case of corrosion study that requires the metal to be protected includes the oil and gas industries. The oil and gas industries experience significant failures of carbon steel due to corrosion

(Ochoa et al. 2015). It is reported that more than 50 % of pipeline failures occur due to corrosion of CO_2 and H_2S [1-3]. Nevertheless, carbon steel is still preferred as a construction material due to its physical properties, which are flexible to use as a material of construction while being more potent than cast iron. The most important parameter responsible for the broad application of carbon steel is the formation of a protective coating on the surface when exposed to the environment. This creates an inhibition effect on the corrosion rate. Also, carbon steel is economically feasible as it has a low material cost compared to wrought iron (Kermani and Harrop 1996; Singh and Mukherjee 2010). In spite of the presence of alloys in the present day that show good corrosion resistance, carbon steel is still widely used in the oil and gas industries for transporting petroleum, natural gas, and produced water over long distances because of its lower cost (Santos and Lo 2014; Dwivedi et al. 2017). According to earlier reports related to carbon steel corrosion in oil and gas industries, corrosion was found to occur due to the transportation of petroleum products and byproducts (Yaro et al. 2015; Al-janabi 2020). The produced water is seen to cause significant corrosion due to the presence of CO_2, volatile fatty acids, sulfides, and other hydrocarbons (Tibbetts et al. 1992; Lin et al. 2017). According to Tibbetts et al. (Tibbetts et al. 1992), produced water is rich in many chemicals. Among them, the presence of volatile fatty acids such as acetic acid and sulfides is significant (Shoesmith et al. 1980; Mueller-Harvey and John Parkes 1987; Brondel et al. 1994). Hence, this work focuses on understanding the various grades of carbon steel corrosion in CO_2-H_2S -acetic acid via electrochemical techniques.

As the corrosion process is an electrochemical phenomenon, understanding the material interaction with a given electrolyte environment is essential. Therefore, researchers rely on electrochemical tests which include electrochemical impedance spectroscopy (EIS), potentiodynamic polarization measurements, cyclic voltammetry, etc., for corrosion investigation. The EIS is a versatile

technique to understand the reactions occurring at the metal/electrolyte interface. The EIS data is more commonly analyzed using electrical equivalent circuit (EEC) fitting. However, EEC fitting has certain drawbacks. In the case of complex reaction systems, the EEC fails to provide detailed information on the reaction mechanism. The parameters obtained from EEC fitting may also be debatable to interpret in cases where intricate equivalent circuits are involved. One more disadvantage of the method includes the inapplicability of the high-frequency points, which is mainly due to the restricted precision of the estimate of the time constant distribution function in the same range (Jeevan Maddala, Krishnaraj Sambath, Vinod Kumar; Lukács and Kristóf 2020). The majority of reported literature on corrosion investigation includes EEC fitting for the data interpretation. To analyze the EIS data in a more detailed manner, another approach, reaction mechanism analysis (RMA), is performed. A mathematical model of impedance is constructed based on the proposed reaction mechanism through the RMA approach. The impedance model is validated using experimental EIS data. The RMA is not only capable of providing a vivid idea about the reaction taking place, it also provides reaction kinetics information and other parameters, including surface behavior in the exposed electrolyte. Thus, in this work, EIS data is analyzed via both EEC and RMA to understand the given electrochemical system.

1.2. Problem Statement

The slurry formulation for the Mo CMP process is of major concern in semiconductor industries. As CMP slurry consists of oxidizers along with other chemical additives, understanding the Mo dissolution in the given oxidizer at a given conditions is of great interest to understand the polishing behavior and to tune the slurry further for achieving desirable results. Among the various oxidizers, H_2O_2 is commonly used for the polishing of many metals, including Mo. Although the dissolution

behavior of many metals, such as Cu, Co, etc., in H_2O_2 has been extensively studied, only limited information is available for Mo dissolution behavior in H_2O_2 solutions.

Our CMP preliminary results show that $KMnO_4$ gives a low Mo etch rate and a significantly high Mo polish rate as compared to H_2O_2. It is really preferred in CMP applications as it reduces CMP issues such as dishing and erosion. Further, alkaline conditions are preferred in the CMP process to avoid corrosion issues. Thus, this study focuses on understanding the dissolution mechanism of Mo in both media in an alkaline regime.

On the other hand, carbon steel is the most preferred material for transportation lines in the oil and gas industries over stainless steel and wrought iron. Carbon steel is classified as low, medium, and high carbon steel based on its carbon content. Among them, medium carbon steel is used for transportation. The tensile strength, hardness, and other properties differ based on the presence of various components (Mn, P, S, V, etc.). Among various grades of carbon steel, API 5L X52 (Karimi Abadeh and Javidi 2019), API 5L X60 (Quej-Ake et al. 2018), API 5L X65 (Madani Sani et al. 2021), API 5L X70 (Quej-Ake et al. 2018) are commonly used in the oil and gas industries [16]. The present work focuses on carbon steel API 5L X52 and API 5L X60 as they are used in the Indian oil and gas industries. The carbon content of both the steels API 5L X52 and API 5L X60 is the same, with more sulphur, vanadium content in API X60 steel, consequently increasing the tensile strength of X60 by more than 1.1 times. For years, research has been going on to improve the mechanical properties of carbon steel by adding several components (Al-Mansour et al. 2009; Wen et al. 2018). Based on the improved mechanical properties of carbon steel X60, it was expected to have better corrosion resistance than steel X52. Nevertheless, it was found that the corrosion rate of X60 is higher than that of X52 in the CO_2 (carbon dioxide) medium (Rihan 2013). However, only limited works have been reported on the corrosion behavior of carbon steels

X52 and X60. A comparative study revealing the failure of X60 over X52 based on the reaction mechanism and kinetics has not been reported to the best of our knowledge. Hence, a systematic study is performed on the corrosion behavior of both the steels to investigate the reaction mechanism in the simulated field that mimics the produced water conditions.

1.3.Motivation

With the rapid progress in technology, the semiconductor industry is also experiencing rapid upgradation in the modern day. This is resulting in slimming and size reduction of electronic devices, causing the ICs to also reduce their size significantly. Cu is used widely as an interconnect by semiconductor industries for many decades for BEOL (back end of the line) processes. However, due to the size shrinkage of ICs (below 10 nm) to reach the present-day requirements, problems are arising in the presence of Cu. Due to its face-centred cubic lattice structure, electron scattering increases when the size is very small, resulting in an increase in resistivity. The cohesive energy decreases, causing unstable microstructures and non-uniform Cu seed layer deposition. On the other hand, Mo is known for its low resistivity, adhesion energy, and low dielectric constant. Mo is also having a more stable microstructure, making it resilient towards both physical stress and chemical corrosion. Further, the passivation behavior reduces the requirement of a barrier layer, lowering the cost of fabrication. Due to these characteristics, Mo is considered a promising candidate for metal interconnects. To employ Mo in these applications, the surface needs to be polished using chemical slurry to avoid patterning issues during the lithography process. However, it was observed that the dissolution behavior of Mo varies across different oxidizers under alkaline conditions during the CMP process. Hence, kinetic and mechanistic investigation of Mo dissolution will help in optimizing the slurry used for the CMP process. Thus, this study is devoted

to understanding the dissolution behavior of Mo in the presence of oxidizers using electrochemical techniques.

The majority of processes in the oil and gas industry use carbon steel as the material of construction. Also, oil recovery can be enhanced by injecting produced water into wells. Besides salts of chlorides and bicarbonates, volatile fatty acids (VFA's) are also found in produced water. Acetic acid is found in higher concentrations than other VFAs such as propionic acid, formic acid, etc. (Kahyarian et al. 2016). These VFAs, along with the presence of CO_2-H_2S, cause damage in the pipelines due to corrosion. There are several works reported on the effect of acetic acid on the corrosion rate of CS in CO_2-H_2S solutions (Singh and Gupta 2000; Santos and Lo 2014; Yaro et al. 2015; Al-janabi 2020; Talukdar and Rajaraman 2020). However, the comparison of the dissolution behavior of various grades of carbon steel has not been reported in an elaborate manner. There are various grades of carbon steel available, yet there is research going on to find a better-performing grade that will be less susceptible to corrosion. However, some cases include where a higher grade of carbon steel performs less than a relatively lower grade. The reason for the lower performing grade is not investigated in detail, although a few works have attributed the behavior to the microstructure of the carbon steel. Hence, the same has been focused on in this study in order to determine the other parameters responsible for the corrosion behavior of the carbon steels of various grades.

The reaction mechanism analysis (RMA) implemented in the study is used to predict the electrode-electrolyte interface reaction using electrochemical impedance spectroscopy. RMA is successfully employed in various fields, including the study of electrolytes, corrosion mechanism study, electro-crystallization, molten salt electrolyte recovery, etc. (Jeevan Maddala, Krishnaraj Sambath, Vinod Kumar; Bechet et al. 1977; Epelboin et al. 1981; Pensado et al. 2001; Baranwal and

Rajaraman 2019; Talukdar et al. 2022; Ghelichkhah et al. 2023). This method of impedance modelling is capable of providing quantitative information on various parameters, including kinetics of hydrogen evolution, oxygen evolution, and mechanistic analysis of catalytic activity. Hence, the present study focuses on the implementation of RMA to understand the electrode behavior in the electrolytic environment under given conditions.

1.4. Aim and Objectives

The overall aim is to study the metallic corrosion behavior (mechanistic reaction pathway and kinetics) in the given electrolyte environment by acquiring EIS data and analyzing the same using a reaction mechanism analysis approach. In the first part of the study, the aim is to inspect the dissolution mechanism of the Mo in H_2O_2 solution interface at alkaline pH. Further, the reasons behind the observed behavior of Mo (high polish rate with low etch rate) in $KMnO_4$ solution during the CMP process by performing a comparative analysis with the Mo dissolution behavior in the more commonly used oxidizer H_2O_2 will be investigated. In the next part of the study, the aim is to compare and investigate the underlying reasons for the varied corrosion behavior exhibited by different grades of carbon steel (X52 and X60) in a simulated electrolyte environment similar to produced water.

To achieve the aim of the thesis, the following objectives are designed

1. To perform anodic polarization and electrochemical impedance spectroscopy at various over potentials in order to investigate the mechanistic reaction pathway and retrieve the kinetic parameters via reaction mechanism analysis approach of Mo dissolution in H_2O_2 and $KMnO_4$ solution at alkaline conditions (pH 10).

2. To perform FESEM analysis to investigate the surface morphology of Mo and the corrosion product formed on the surface after being exposed to the solution of interest.
3. To perform XPS analysis to determine the composition of the corrosion product formed on the metal surface and also to corroborate the XPS findings with the results obtained from the electrochemical investigation.
4. To perform potentiodynamic polarization and electrochemical impedance spectroscopy at OCP and various overpotentials to investigate the corrosion reaction mechanism, and also retrieve the kinetic parameters using the reaction mechanism analysis approach of carbon steels X52 and X60 in the presence of CO_2-H_2S and acetic acid solution.
5. To perform FESEM analysis to investigate the surface morphology of the carbon steels and the corrosion product formed on the surface after being exposed to the solution of interest.
6. To perform a contact angle study to understand the surface nature of the carbon steel surface under various conditions.
7. To perform XPS analysis to determine the composition of the corrosion product formed on the carbon steel surface, and also to substantiate the XPS findings with the results obtained from the electrochemical investigation.

1.5. Hypothesis

i. In the first part of the study, the dissolution reaction mechanism of Mo in the presence of an oxidizer will be postulated.

ii. Using the kinetic data retrieved from impedance data acquired at various overpotentials, the underlying reasons behind the high polish rate but low etch rate observed for $KMnO_4$ solution as compared to H_2O_2 solution will be identified.

iii. In the second part of the study, the dissolution reaction mechanism of Carbon steel in CO_2-H_2S-acetic acid solution will be postulated.

iv. From the kinetic information obtained from EIS data obtained at various overpotentials, the reasons for the higher corrosion rate observed for X60 compared to that of X52 will be identified.

1.6. Contribution of the Study

As mentioned in the earlier part of this chapter, this work includes corrosion investigation of metals in two diverse fields via electrochemical methods. The fundamental aspects that are highlighted through the work will be useful in the application part. May it be the design of a slurry for the CMP process or the choice of material based on the components it is exposed to. Due to the properties of Mo as already discussed before, it will be applied widely as an interconnect to achieve barrierless planarization. Hence, getting a vivid idea about the reaction mechanism in the presence of oxidizers will be helpful in the formulation of slurries for achieving desired results. In this study, the mechanistic reaction pathway and kinetics of Mo dissolution in H_2O_2 and $KMnO_4$ solution is elucidated. Further, this work clearly demonstrates via reaction mechanism analysis of EIS data acquired for two different oxidizers that the desired high polish rate and low etch rate is achieved in the CMP process by understanding the following phenomenon : (i) rate of formation of metal oxides on the metal surfaces (ii) the rate of dissolution of the same from the metal surface and (iii) stability of these oxides in the presence and absence of external force such as pressure applied on the metal being polished. For predicting the corrosion rate of the material in the given environment more precisely and for industrial corrosion mitigation, understanding the dissolution mechanism along with kinetics is critical. In this work, the dissolution behavior (mechanism and kinetics) of two different grades of carbon steel in the same environment is elucidated via

analyzing the EIS data by the RMA approach. This study clearly suggests that the surface characteristics of the carbon steel, such as surface energy and the number of active sites on the surface, also affect the corrosion rate. The nucleation and growth of metal oxides on the metal surface are strongly influenced by these surface characteristics in the given environmental conditions. This would eventually decide the nature of the oxides (fine/coarse) and their passivation behavior on the metal surface. So, to predict the corrosion rate of carbon steel in the given environment more precisely, these factors need to be considered.

1.7. Thesis layout

The first introductory chapter discusses the background, problem statement, motivation, aim and objectives, hypothesis, and contribution of the study. The second chapter provides a comprehensive literature review and identifies the lacunae that this research aims to address. The third chapter details the materials and methods employed to achieve the objectives of the work. The fourth chapter discusses the theoretical background of the experimental methods implemented to achieve the objectives. The fifth chapter discusses the investigation on the anodic dissolution of Mo in alkaline solutions containing oxidizer (H_2O_2) via electrochemical impedance spectroscopy. The mechanistic reaction pathway and kinetics of the considered system are reported. The sixth chapter discusses the anodic dissolution behavior of molybdenum in potassium permanganate solution and compares it with the Mo dissolution behavior in H_2O_2 solution. The seventh chapter discusses the investigation of carbon steels (API 5L X52 and API 5L X60) dissolution in CO_2-H_2S solutions in the presence of acetic acid. Eight chapter summarizes the thesis and provides a concise overview of the study. Finally, the ninth chapter discusses the conclusion drawn from the entire study and suggests possible areas for future research.

The present study focuses on investigating the mechanistic and kinetic behavior of anodic dissolution of metals in diverse industrial conditions (Molybdenum dissolution in semiconductor industries and carbon steel corrosion in oil and gas industries) in suitable media. Various electrochemical and other methods are used to characterize it in a corroded system. In Chapter 2, we have presented a comprehensive literature survey to find the research gap and establish the objectives of the present work.

CHAPTER 2

Chapter II Literature Review

In this section, the literature review is carried out for the corrosion investigation of metals in different electrolytes. The initial part includes the dissolution behavior of molybdenum and other metals in the presence of oxidizers applicable to semiconductor industries. The latter part includes corrosion studies of carbon steel in different media, preferably during transportation in the oil and gas industries. This is followed by a brief inclusion of the use of reaction mechanism analysis applied for the determination of the corrosion reaction mechanism.

The effect of corrosion has existed since the existence of the Earth. However, it took time to name it as a phenomenon. Starting from 23-79 AD, various writers, philosophers, and scientists tried to explain the phenomena(Ahmed 2006). The mechanism of corrosion was first explained by Robert Boyle as corrosion science in the year 1657 through his work (Boyle 1675). Later on, Faraday, with his notable endowment, entrenched corrosion as an electrochemical phenomenon through his quantitative relationship between the chemical and electrochemical aspects (Walsh 1992). The first and second laws of Faraday are the basis for calculating the corrosion rate of metals. Scientists gradually provided many insights, such as introducing a scientific principle to control corrosion. The passivation process of iron was reported by Schonbein (Schonbein C 1936). U. R. Evans, through his classical hypothesis, contributed to the comprehension of the causes of corrosion (Evans 1948). In the later stage, Uhlig (Ahmed 2006), Evans(Evans 1948), and Fontana (Mars G. Fontana 1987) made significant contributions towards the considerable progress of understanding corrosion.

Hence, it is evident that for centuries, scientists have worked hard and kept on providing insight into corrosion. In the present chapter, we will be discussing the corrosion of metals such as carbon

steel in various corrosive environments, including carbon dioxide, hydrogen sulfide, acetic acid, and molybdenum in the presence of various oxidizers.

2.1. Dissolution Behavior of Metals in the Presence of Various Oxidizers

Aluminum (Al) was used as an interconnect material a few decades back (Ozawa 1993). However, due to electromigration problems, Al was replaced with copper (Cu) (Hinode et al. 1987) which is widely used as an interconnect to fabricate integrated circuits (Du et al. 2004; Prasad and Ramanathan 2007; Bernard et al. 2008; Venkatesh and Ramanathan 2010). These metals need to be polished using suitable oxidizers and other additives to meet the requirements of the semiconductor industry. Several works have been reported on the dissolution behavior of metals (copper, cobalt, ruthenium, and tungsten) in the presence of oxidizers (Ein-Eli et al. 2003; Seo and Lee 2005; Jiang et al. 2014b; Paul and Srinivasan 2020). Electrochemical studies on the oxidative dissolution and passivation of copper (Cu) are found (Carpio et al. 1995; Xu et al. 2004; Paul et al. 2005; DeNardis et al. 2010). A strong passivation process on the Cu surface at higher H_2O_2 concentration was observed due to oxide formation at a faster rate at pH 4. Further, when glycine and copper sulphate were added, there was an increase in the dissolution rate of copper (Du et al. 2004; Xu et al. 2017). Similar observations are reported at pH 2 and neutral pH, also (Aksu et al. 2003; Deshpande et al. 2004). A reaction network of Cu in the presence of hydrogen peroxide was proposed. The reaction orders, rate constants, complexation reaction kinetics, and oxide formation were determined by performing experiments and applying analysis theories (Palaparthi and Muldowney 2006). The dissolution of Cu in nitric acid and ammonium hydroxide was also reported. Owing to active dissolution, Cu showed a high dissolution rate in the presence of nitric acid. In the presence of ammonium hydroxide (NH_4OH), the dissolution rate was observed to be decreased, and

via electrochemical studies, the passivation of Cu was confirmed in the presence of NH_4OH (Carpio et al. 1995).

The dissolution behavior of cobalt (Co) in the presence of H_2O_2 is also reported. The passivation behavior of Co was observed at all pH ranges. With increased H_2O_2 concentration, the passivation rate was observed to increase. However, in the presence of glycine at pH 8, both ER and PR were observed to increase due to the formation of Co(III)-glycine complex, which is soluble in nature (Jiang et al. 2014a; Lianjun Hu, Guofeng Pan, Yi Xu, Hao Wang, Yiwen Zhang, Ru Wang 2020; Paul and Srinivasan 2020; Hazarika et al. 2023a).

The dissolution behavior of ruthenium (Ru) in the presence of H_2O_2 illustrates an active dissolution regime with an increase in peroxide concentration due to the formation of soluble Ru oxides (Jiang et al. 2014c). Along with the selection of oxidizers in the case of Ru polishing, the slurry pH also plays a crucial role, since at some conditions, RuO_4 is formed, which is toxic in nature and hence is the most undesirable condition in CMP applications. Effect of potassium periodate (KIO_4) was reported on Ru dissolution at pH 9. At a higher concentration of KIO_4 with increased solubility at an elevated pressure, the removal rate (RR) of Ru was increased. Also, RuO_4 was not formed at the mentioned pH (Peethala and Babu 2011). The effect of potassium iodate (KIO_3) on the dissolution of Ru showed an associative mechanism and an increased RR (Hazarika et al. 2023b). Since Ru is used as the barrier metal, it creates galvanic corrosion with Cu interconnects. Hence, the dissolution behavior of Ru along with Cu in the presence of sodium percarbonate was presented. The experiments were performed at a pH 10, the slurry was designed to control galvanic corrosion of Ru (Turk et al. 2013). The Ru polish rate in the presence of sodium periodate was found to be highest at 7. With further increase or decrease in the pH value, the polish rate (PR) was decreased. EIS measurements at various pH ranges were carried out from acidic to

alkaline regime. At neutral pH the lowest charge transfer resistance was observed (Cui et al. 2012). The dissolution behavior of Cu/Ru/TiN in CMP process in the presence of $KMnO_4$ is also reported. An adequate polish rate was achieved with 10 mM $KMnO_4$. At this concentration, the individual film corrosion was also low (Sagi et al. 2016). The effect of various oxidizers on tungsten CMP is reported, which includes H_2O_2, $Fe(NO_3)_3$, and KIO_3 at natural pH of respective slurries. The experimental observations confirmed the highest RR in the presence of $Fe(NO_3)_3$ and the lowest RR for KIO_3 (Seo and Lee 2005).

The dissolution of W in H_2O_2 was studied, and the mechanism for material removal was reported. The surface roughness decreases towards acidic pH and increases towards alkaline pH. The RR decreases with increasing pH till neutral condition and again increases sharply towards a more alkaline region. In the alkaline region, the material dissolution mechanism is predominant, whereas the removal of the passivation layer is dominated in the acidic region (Wang et al. 2023a). The key literature on the dissolution behavior of various metals in the presence of oxidizers is shown in Table 2.1.

Table 2.1. Key literature on the dissolution behavior of various metals in the presence of oxidizers

Metal	Corrosion Environment	Experimental Conditions	Experimental Methods	Key Findings	Reference
Cu	Aqueous solution of H_2O_2	H_2O_2 concentration: 1, 5, 10 Wt. % pH: 4	ER, CMP, LPR, EIS, XPS, SEM	1. RR was maximum at 1 Wt. % H_2O_2 2. RR decrease with further increase in H_2O_2 conc. 1. Strong passivation at higher H_2O_2 conc.	Du. et al. (Du et al. 2004)
Co	H_2O_2 solution in presence of glycine	H_2O_2 concentration: 1, 2, 4 Wt. % pH: 2, 4, 6, 8, 10, 12 Glycine concentration: 0.1 M	SER, LPR, XPS	1. SER and RR decreased with increasing pH 2. Formation of compact and passive Co oxides 1. Decrease in RR with further increase in H_2O_2 conc.	Jiang et al. (Jiang et al. 2014a)
Ru	KIO_4	KIO_4 concentration: 0.015, 0.03, 0.05, 0.1, 0.15 M pH: 3, 4, 5, 6, 7, 8, 9, 10	SER, RR	1. At higher conc. of KIO_4 RR was increased 2. Toxic RuO4 was not formed	Peethla et al. (Peethala and Babu 2011)
Ru	H_2O_2	H_2O_2 concentration: 1, 1, 2, 4 wt. %	RR, LPR, Zeta potential	1. Various Ru oxides were formed such as $Ru(OH)_3$, $RuO_2.2H_2O$, and RuO_4^{2-} 2. RR increases with increase of K^+ ionic strength 3. KNO_3 is preferred for K^+ ion source over KOH and K_2CO_3	Liang et al. (Jiang et al. 2014b)
Cu/Ru/ TiN	Aqueous solution of $KMnO_4$	$KMnO_4$ concentration: 1, 5, 10, 25, 50 mM pH: 9	RR, LPR, OCP	1. Desired polish rate obtained at 10 mM conc. of $KMnO_4$ 2. Individual film corrosion was low	Sagi et al. (Sagi et al. 2016)
W	H_2O_2, $Fe(NO_3)_3$, KIO_3	Natural pH	RR	1. Highest RR in presence of $Fe(NO_3)$ 2. Lowest RR in presence of KIO_3	Seo et al. (Seo and Lee 2005)

2.2. Dissolution Behavior of Molybdenum in Acidic and Alkaline Environments

Among the above-discussed metals used in CMP semiconductor applications, there are certain limitations in most cases. Hence, an emerging alternative is introduced. Molybdenum (Mo) possesses excellent thermal and electrical properties (Yang et al. 2018, Qu et al. 2017). Due to its high melting point, Mo is mostly stable and harbors strength and stiffness at very high temperatures. It also has high thermal and electrical conductivity and low resistivity. Thus, Mo is utilized in a widespread manner, including electronic device manufacturing, as listed in Table 2.2 (Yoshida and Uemura 1994; Itagaki et al. 1998; Walser et al. 2011). To be more specific, with properties such as high adhesion energy, low electrical resistance, etc., Mo is being considered as a promising candidate in semiconductor industries as an interconnect metal.

Some of the reported works on Mo dissolution behavior are discussed hereafter. Mo is added to alloys to enhance the properties of various steel grades. Since these steels are susceptible to corrosion in various environments, some literatures are reported for the anodic dissolution of Mo in acidic and alkaline environments (Micheal N Hull 1972; Walser et al. 2011; Dai et al. 2020). Mo shows rapid dissolution in the H_2SO_4 system with high surface coverage, and Mo(V) was formed at a rapid rate. The Mo(V) was further oxidized into a soluble form via hydrolysis. The anodic dissolution of Mo in H_2SO_4 solution occurs via the rapid formation of Mo_2O_5 on the metal surface, which is further oxidized and dissolved by hydrolysis (Itagaki et al. 1998).

$$2Mo + 5H_2O \rightarrow Mo_2O_5 + 10H^+ + 10e^- \quad (2.1)$$

$$Mo_2O_5^+ + H_2O \rightarrow Mo_2O_5OH + H^+ \quad (2.2)$$

In the presence of an alkaline KOH medium, the Mo surface was observed to be covered with varying oxide/hydroxide films. The formation of the oxides and hydroxides was majorly dependent

on the overpotential applied. At lower overpotential, Mo(III) was observed, and Mo(V) and Mo(VI) were observed to be formed at higher overpotential (Itagaki et al. 1998). Mo (III) was formed at a lower overpotential based on the following equation. Here, the second reaction is considered to be slow (Micheal N Hull 1972).

$$Mo + 3OH^- \rightarrow Mo(OH)_3 + 3e^- \quad (2.3)$$

$$Mo(OH)_3 + 5OH^- \rightarrow MoO^{2-}{}_4 + 4H_2O + 3e^- \quad (2.4)$$

However, Mo (V) and MoO_3 were formed at a higher voltage range as per the following mechanism (Micheal N Hull 1972).

$$Mo + 4OH^- \rightarrow MoO^{+}{}_2 + 2H_2O + 5e^- \quad (2.5)$$

$$MoO^{+}{}_2 + 2OH^- \rightarrow MoO^{-}{}_3 + H_2O \quad (2.6)$$

$$MoO^{-}{}_3 \rightarrow MoO_3 + e^- \quad (2.7)$$

$$MoO_3 + 2OH^- \rightarrow MoO^{2-}{}_4 + H_2O \quad (2.8)$$

Table 2.2 Various industrial applications of Mo

Type of industry	Application
Iron and steel	Alloy
Glass manufacturing	Electrical heating/ heat booster electrodes
Electronic device manufacturing	**Solid state/ thermionic devices**
Welding and fabrication	Resistance weld electrodes, welding rolls, tips
Energy storage and battery technology	As a battery component in super-batteries
Aerospace, oil and gas, automobile, etc.	Deep hole machining, grinding quills, missile, refractory material
Other	Magnetrons, heat pipes, X-ray tubes, thyristors, crystal growing devices, etc.

2.3. Dissolution Behavior of Molybdenum in the Presence of Various Oxidizers

In the last section we discussed about the anodic dissolution of Mo in acidic and alkaline medium. However, most of them included application of Mo for addition in alloys. The present section focuses on the dissolution behavior of Mo in the presence of various oxidizers. Mo polishing behavior in the presence of H_2O_2 at varying pH conditions was investigated. Active dissolution with a high etch rate (ER) and polish rate (PR) was observed for Mo at alkaline pH (8-10) in the presence of H_2O_2. The ER and PR were even enhanced with the addition of ammonium sulfate. They predicted the formation of ammonium molybdate to be responsible for the better removal of Mo via electrochemical studies and XPS analysis (Fei Chen, Xu Zeng, Jing-Bo Xu, Hai- Sheng Lu 2012). The chemical reaction between Mo and H_2O_2 is suggested as follows (Saji and Lee 2012; Qu et al. 2017) based on the products observed in XPS analysis.

$$Mo_2O_5 + H_2O_2 \rightarrow 2MoO_3 + H_2O \qquad 2.9$$

$$MoO_3 + 2OH^- \rightarrow MoO_4^{2-} + H_2O \qquad 2.10$$

In the alkaline pH and presence of H_2O_2, the addition of colloidal Si decreased both the removal rate and static etch rate of Mo. They also observed the adsorption of the colloidal Si particles on the oxidized Mo film. The formation of silico-molybdic acid due to the reaction between Mo oxide and colloidal Si was confirmed through Raman spectroscopy (Feng et al. 2015). The inhibitory effect of colloidal Si in the CMP process of Mo was also confirmed by Qu et al. (Qu et al. 2017). However, the addition of ammonium sulfate enhanced both the static etch rate and polish rate. The increase in the SER and RR by the addition of ammonium sulfate was due to the formation of $(NH_4)_2MoO_4$, which was highly soluble in nature (Qu et al. 2017). The addition of glycine in H_2O_2-based solutions under alkaline conditions also decreased the RR and ER of Mo. With the increase

in glycine concentration, the dissolution rate decreased. The reduced reaction rate due to the addition of glycine was confirmed through OCP measurement. Glycine molecules got adsorbed on the Mo surface, inhibiting the formation of Mo oxide and eventually lowering the dissolution rate (Feng et al. 2014). As reported by Yang et al.(Yang et al. 2018), the rate of Mo oxide formation was retarded since the glycine Zwitterion was electrostatically adsorbed on the surface. This eventually acted as a hindrance between the metal surface and the oxidizer. This led to the retarded oxidation reaction to predominate and resulted in the inhibition of the Mo dissolution, which also provided a more smooth surface (Yang et al. 2018). The effect of H_2O_2 concentration and pH on Mo dissolution was reported. An increase in H_2O_2 concentration increased the ER and RR. The highest ER was observed at pH 10. However, the highest RR was observed at pH 2 and 10. Mostly peroxo-Mo complex was formed with H_2O_2, which was responsible for the increasing ER with increasing H_2O_2 concentration (Ryu et al. 2021). The key literature on the anodic dissolution of Mo in the presence of oxidizers is illustrated in Table 2.3.

Table 2.3 Key literature on the anodic dissolution of Mo in the presence of oxidizers

Metal	Corrosion Environment	Experimental Conditions	Experimental Methods	Key Findings	Reference
Mo	Aqueous solution of H_2O_2 and glycine	H_2O_2 concentration: 5 Vol. % pH: 9 Glycine conc.: 0, 1, 10, 100 mM	SER, CMP, PP,	1. SER and RR decrease with the increase of glycine conc. 2. Active-passive-transpassive behavior observed in anodic dissolution	Yang et al. (Yang et al. 2018)
Mo	H_2O_2 solution in presence of colloidal silica	H_2O_2 concentration: 0, 1, 3, 5, 10 Wt. % pH: 2, 4, 6, 8, 10, 12	SER, PP, XPS	1. SER is constant in the acidic regions and increases towards alkaline but further decreases at higher alkaline conditions. 2. Anodic dissolution increases with an increase in H_2O_2 conc.	Qu et al. (Qu et al. 2017)
Mo	H_2O_2 and Ammonium sulphate solution	H_2O_2 concentration: 1, 5, 10 Wt. % pH: 8, 9, 10	SER, PP	1. High SER and polish rate at alkaline pH 2. Addition of ammonium sulfate increased both SER and polish rates. 3. Increase in corrosion current with increasing H_2O_2 conc.	Feichen et al. (Fei Chen, Xu Zeng, Jing-Bo Xu, Hai-Sheng Lu 2012)
Mo	Aqueous solution of H_2O_2	H_2O_2 concentration: 2.5, 5 Wt. % pH: 2, 4, 6, 8, 10	SER, RR, PP, XPS	1. High SER and RR at higher pH 2. High SER, anodic current with increase in H_2O_2 conc.	Ryu et al. (Ryu et al. 2021)

2.4. Corrosion Behavior of Carbon Steel in the presence of CO_2, H_2S, and acetic acid

Carbon steel is the most preferred material in the oil and gas industry despite the presence of other higher-performing alloys. Carbon steel is often reported to form a protective layer on the surface when exposed in to a corrosive environment. The protective layer prevents the material from corrosion up to a certain extent. In the following section, we are going to discuss how carbon steel behaves in the presence of various corrosive agents such as CO_2, H_2S, and acetic acid, both individual and synergistic effects.

2.4.1. Corrosion of Carbon Steel in the Presence of CO_2

CO_2 gas dissolves in water and produces carbonic acid. The carbonic acid is extremely corrosive to carbon steel. In dry conditions, CO_2 gas will not have any effect on carbon steel, but when it finds an aqueous base, it corrodes the metal (Cui et al. 2006; Rustandi et al. 2013; Ochoa et al. 2015; Alam et al. 2016).

Dissolution of CO_2 gas in aqueous phase:

$$CO_2(g) \leftrightarrow CO_2(aq) \quad (2.11)$$

$$CO_2(aq) + H_2O(l) \leftrightarrow H_2CO_3(aq) \quad (2.12)$$

Dissociation of carbonic acid

$$2H_2CO_3(aq) + 2e \rightarrow H_2(g) + 2HCO_3^-(aq) \quad (2.13)$$

$$2HCO_3^-(aq) + 2e \rightarrow H_2(g) + 2CO_3^-(aq) \quad (2.14)$$

The electrochemical reaction for corrosion is as follows:

Cathodic reaction

$$2H^+(aq) + 2e \rightarrow H_2(g) \quad (2.15)$$

Anodic reaction

$$Fe(S) \rightarrow Fe^{+2}(aq) + 2e \qquad 2.16$$

Overall reaction

$$Fe(S) + CO_2(\text{g}) + H_2O(l) \rightarrow FeCO_3(s) + H_2(g) \qquad 2.17$$

Rustandi et al. (Rustandi et al. 2013) studied the corrosion response of carbon steel API 5L X52 in the presence of saturated CO_2 in sodium chloride (NaCl) solution. They reported corrosion behavior in varying acidic conditions, as well as fluid flow rate, and reported an increasing corrosion rate with decreasing acidity. At lower pH, the corrosion mechanism was predominantly mass transfer controlled, while at higher pH, the corrosion rate was chemically controlled. A study on CO_2 corrosion of API X52 and X60 in salt water by Rihan (Rihan 2013) reported a higher corrosion rate of X60 than X52. The work was carried out at pH 4.4 and 50 °C and in a stirred condition at an impeller speed of 2000 rpm. They observed less ferrite content in the microstructure of X60, which is responsible for the higher corrosion rate. The carbon steel corrosion in the presence of carbon dioxide was studied using the EIS (electrochemical impedance spectroscopy) study and gravimetric measurements (Das Chagas Almeida et al. 2015). A similar reaction mechanism for corrosion in the presence and absence of CO_2 is reported in this study. The corrosion study of carbon steel was performed in the presence of CO_2 gas under 4 MPa pressure in a wide range of temperatures (50-180 °C) (Yin et al. 2009). The corrosion rate was observed to be the highest at 60 °C. There was no significant difference in corrosion rate at higher temperature ranges. The corrosion product layers covered the metal surface uniformly at all temperature ranges, and the product layer thickness decreased towards higher temperatures (Yin et al. 2009). The dependence of carbon steel corrosion on temperature, pressure, and pH was investigated by Nor et

al. An Increase in the partial pressure of CO_2 increased the pH of the electrolyte due to an elevation in the carbonic acid concentration. The corrosion rate was reported to be high at higher temperatures and pH. The increase in the corrosion rate is due to the formation of a less stable corrosion product, iron carbide, under the experimental conditions, which does not provide sufficient corrosion protection. The anodic reaction was observed to be charge transfer controlled since there was no effect of flow on the corrosion rate even at high CO_2 partial pressure (Nor et al. 2011) . The CO_2 corrosion mechanism investigated was based on the anodic and cathodic polarization of mild steel in the presence of CO_2 solutions. The iron dissolution was majorly affected by CO_2 concentration. A mechanistic analysis of CO_2 corrosion predicted the reduction of HCO^-_3 and H_2CO_3 via intermediate steps. The study was conducted in an acidic pH range between 4-6 with a CO_2 partial pressure of 15 bar. They predicted a homogeneous dissociation of the carbonate species within the boundary layer. The mechanism was also validated through a mathematical model based on H^+ ion reduction (Kahyarian and Nesic 2020). Carbon dioxide corrosion of carbon steel in the presence of 1 wt. % NaCl was investigated at 80 °C, and the effect of $CaCO_3$ precipitation on the carbon steel was monitored. Electrochemical studies suggest that the protective $FeCO_3$ layer was removed due to the precipitation of $CaCO_3$ on the metal specimen surface (Rizzo et al. 2020). The key literature on CO_2 corrosion of carbon steel is presented in Table 2.4.

Table 2.4 Key literature on CO_2 corrosion of carbon steel

Material	Corrosion Environment	Experimental Conditions	Experimental Methods	Key Findings	Reference
API 5L X52	CO_2 dissolved in 3.5 % NaCl solution	pH 4,5 and 6 Temperature: 25^oC Turbulent condition at 0, 375, 750, 1500, 3000 rpm	LPR	1. CR decreased with increasing pH 2. At pH4: CR is flow sensitive 3. pH 4: CR is mass transfer-controlled pH 5 & 6: 4. CR is reaction-controlled	Rustandi et al. (Rustandi et al. 2013)
API X52 and X60	Saturated CO_2 in 3 % NaCl solution	pH 4.4 Temperature: 50^oC Turbulent condition at 2000 rpm	LPR, EIS	1. CR of both the steel decreased with time of exposure **2. CR of X60 was higher than X52**	Rihan (Rihan 2013)
Carbon Steel	Saturated CO_2 in 164.8 gpl NaCl solution	pH: 3.96-4.0 Temperature: 50-180^oC	WL, EIS	1. CR increases with increase in temperature 2. At high temperatures the corrosion product film thickness decreases	Yin et al. (Das Chagas Almeida et al. 2015)
Carbon Steel	Saturated CO_2 in chloride ions	CO_2 partial pressure: 20 bar Temperature: 100^oC Cl^- concentration: 0-150 g/L	WL, LPR, SEM, XRD	1. Maximum CR rate was observed with increase in chloride concentration at a constant temperature and CO_2 partial pressure 2. With further increase in chloride concentration a corrosion inhibition was observed Chloride ions can destroy the corrosion product eventually changing the morphology	Liu et al.(Liu et al. 2014)

2.4.2. Corrosion of Carbon Steel in the Presence of H_2S

The corrosion mechanism of carbon steel in the presence of H_2S follows a number of steps. The H_2S is dissociated to H^+ and HS^- ions and the HS^- ions are further dissociated to H^+ and S^{2-} ions as written below.

$$H_2S \rightarrow H^+ + HS^- \quad (2.18)$$

$$HS^- \rightarrow H^+ + S^{2-} \quad (2.19)$$

Fe is oxidized to Fe^{2+} at the anode, and H^+ ions combine at the cathode to release H_2 gas. The Fe^{2+} ions further react with H_2S to produce FeS (via sulfide pathway) and $Fe(HS_2)$ (via bisulfide pathway).

$$2H^+ + 2e \rightarrow H_2 \quad (2.20)$$

$$2H_2S + 2e \rightarrow 2HS^- + H_2 \quad (2.21)$$

$$Fe \rightarrow Fe^{+2} + 2e \quad (2.22)$$

$$Fe^{+2} + H_2S \rightarrow FeS + 2H^+ \quad (2.23)$$

$$Fe^{+2} + 2HS^- \rightarrow Fe(HS_2) \quad (2.24)$$

Liu et al. (Liu et al. 2013) reported the corrosion behavior of carbon steel grade X52 in the presence of H_2S at a temperature range of 20 ^oC to 140 ^oC. They reported that the morphology and corrosion products were affected directly by H_2S concentration at varying temperatures, eventually changing the corrosion rates. They also reported the variation of corrosion products from iron-rich to sulfur-rich components, and sequentially, they can be represented as mackinawite, followed by troilite and pyrrhotite. Abadeh et al. (Karimi Abadeh and Javidi 2019) reported an inhibition in corrosion

rate at 100 ppm of H_2S concentration due to the formation of ferrous sulfide (FeS) as a corrosion product. On investigating the effect of microstructure on CO_2 corrosion of X52, it was observed that the corrosion behavior depends on microstructure in the presence of CO_2. However, in the presence of H_2S, the outer layer was reported to contain $FeCO_3$, whereas S was found along with Fe, C, and O in the inner layer. The corrosion rate was observed to decrease with the appearance of the outer layer, and the ferrous ion concentration was also found to be very high near the carbon steel surface (Gao et al. 2011). Microstructures with more ferrite and cementite are less prone to corrosion. In the presence of H_2S, FeS was formed upon oxidation of the metal, resulting in a reduction of the corrosion rate. With a further increase in H_2S concentration, the corrosion rate increased due to cracks on the product film surface (Ma et al. 2000; Okonkwo et al. 2017). They also observed an increase in the rate of corrosion at an H_2S concentration of 200 ppm and explained it to be the formation of a defect in the corrosion product. Mild carbon steel corrosion in the presence of H_2S shows a distinct cathodic polarization behavior. A cathodic polarization curve consisting of a double wave shape was observed in the presence of H_2S. The direct reduction of H_2S is responsible for this kind of cathodic behavior (Kahyarian and Nesic 2019). The FeS film formation is also significantly responsible for the type of corrosion observed. High temperature and high H_2S concentration accelerate the formation of iron sulfide, which causes the corrosion type to change. The increasing H_2S concentration generates pitting corrosion (Pessu et al. 2016). Qi et al. studied the effect of H_2S on the tensile properties of A35LF2 steel. They observed a decrease in tensile strength of the carbon steel. At very high concentrations of H_2S, hydrogen embrittlement with fracture cracks on the surface was also reported (Qi et al. 2014a). Tang et al. reported significant increase in corrosion of carbon steel with increase in H_2S concentration. According to them the increase in hydrogen evolution reaction rate due to the presence of H_2S was

responsible for the higher corrosion rate. Severe pitting corrosion was observed and the corrosion product was confirmed as mackinawite (Tang et al. 2010). The effect of H_2S on carbon steel corrosion was investigated by Qi et al. They studied the effect of H_2S on carbon steel at a wide temperature range, from room temperature to 90 °C. They observed the corrosion rate to increase with temperature initially which was again decreased with further increase in temperature. At higher temperature a more stable corrosion product cubic FeS was produced which protected the steel surface from further corrosion (Qi et al. 2014b). The key literature on H_2S corrosion of carbon steel is shown in Table 2.5.

Table 2.5 Key literature on H_2S corrosion of carbon steel

Material	Corrosion Environment	Experimental Conditions	Experimental Methods	Key Findings	Reference
X52	H_2S in anaerobic aqueous environment	Temperature: 60°C H2S concentration: 5,10,20,22, 27, 60, 90, 120, 140 g/L	WL, SEM-EDS, XRD	1. CR increased with an increase in temperature up to 90°C decreased at 120°C, and then further increased at 140°C 2. CR increased with an increase in H_2S concentration at 90°C 3. H2S concentration affects the formation of different types of iron sulfides	Liu at al. (Liu et al. 2015)
SAE 1020	H_2S environment	H_2S concentration: 58.9, 198.99, 341.68, 408.44 Temperature: 90°C	LPR, EIS, SEM	1. CR increased with increase in H_2S concentration 2. Cathodic corrosion rate increased 3. Corrosion products formed was mackinawite. 4. Severe localized corrosion observed.	Tang et al. (Fatah et al. 2011)
Low alloy pipeline steel	H_2S environment	Temperature: 25, 40, 60, 90 °C	WL, EIS	1. CR increased upto 40 °C, after that reduced 2. Corrosion products at higher temperature were stable in nature	Qi.et.al. (Liu et al. 2023)

2.4.3. Corrosion of Carbon Steel in the Presence of Acetic Acid (HAc)

Produced water contains volatile fatty acids (VFA), and in VFA, the presence of acetic acid is the majority. Hence, there are several works reported on the corrosion behavior of carbon steel in the presence of acetic acid. Okafor et al. (Okafor et al. 2009) studied the effect of acetic acid on the corrosion of carbon steel at higher temperatures. It was reported that the corrosion rate of carbon steel, API X65 increased with an increase in concentration of acetic acid and temperature. Corrosion behavior in the presence of acetic acid for mild steel was studied by Singh et al. (Singh and Gupta 2000) at high temperatures. They monitored the corrosion rate at various acetic acid concentrations ranging from 5% to 80% and found the corrosion rate to be maximum at 20 %. At 20 % acetic acid concentration, the maximum corrosion rate was at 35 ^{o}C.

Tran et al. (Tran et al. 2013) explained the mechanism for the corrosion behavior of mild carbon steel in the presence of acetic acid in a NaCl medium. It was found that acetic acid is the main source of hydrogen ions that can eventually be responsible for the corrosion of carbon steel X65. Being a weak acid, acetic acid dissociates partially in the solution as follows.

$$HAc \rightleftharpoons H^{+} + Ac^{-} \qquad 2.24$$

The undissociated acetic acid molecule is adsorbed on the metal surface and gets reduced by direct reduction reaction.

$$HAc + e^{-} \rightleftharpoons \frac{1}{2} H_2 + Ac^{-} \qquad 2.25$$

The mechanism undergoing at the cathode is

$$H^{+} + 2e^{-} \rightleftharpoons H_2 \qquad 2.26$$

$$2HAc + 2e^- \rightleftharpoons H_2 + 2Ac^- \quad (2.27)$$

Fe is oxidized at the cathode

$$Fe \rightarrow Fe^{+2} + 2e \quad (2.28)$$

Fe combines with the acetate ion forming iron acetate. The iron acetate is highly soluble and unstable. Hence, it gets dissolved in the electrolyte.

$$Fe^{2+} + Ac^- \rightleftharpoons FeAc^+ \quad (2.29)$$

$$Fe^{2+} + 2Ac^- \rightleftharpoons FeAc_2 \quad (2.30)$$

Table 2.6 Key literature on HAc corrosion of carbon steel

Material	Corrosion Environment	Experimental Conditions	Experimental Methods	Key Findings	Reference
Carbon steel X65	Acetic acid solution	Temperature: 40-80°C NaCl concentration: 1 wt % Acetic acid concentration: 1000 ppm pH: 5	LPR	1. Acetic acid presence does not affect the anodic reaction whereas affects the cathodic reaction 2. CR increases with an increase in acetic acid concentration 3. An increase in temperature increases the CR	Okafor et al. (Okafor et al. 2009)
Mild steel	Acetic acid medium	HAc concentration: 5,10,20,60,80 Temperature: 25,35, 45°C	WL, LPR	1. The most corrosive environment was in 20% HAc concentration 2. CR rate increased with an increase in temperature	Singh et al. (Singh and Gupta 2000)

It was also reported that acetic acid increases the corrosion rate by enhancing the cathodic reaction rate. Kahyarian et al. [59] reported the effect of acetic acid on the corrosion behavior of mild steel.

They worked with carbon steel API 5L X65 in acetic acid solution at varying pH conditions. The presence of acetic acid increased the corrosion rate of the mild steel. The key literature on CO_2-HAc corrosion of carbon steel is included in Table 2.6.

2.4.4. Corrosion of Carbon Steel in the Presence of CO_2, H_2S, and HAc

In the previous sections we discussed about the individual effects of CO_2, H_2S and acetic acid on carbon steel corrosion. In the foregoing section we will look into the works reported on the combined effects of CO_2-H_2S, CO_2-Hac on carbon steel and finally the synergistic effects of all the three components on carbon steel corrosion.

2.4.4.1. Corrosion of Carbon Steel in the Presence of CO_2- H_2S

Abadeh et al. (Karimi Abadeh and Javidi 2019) reported the effect of carbon dioxide on the corrosion of carbon steel X52 in the presence of H_2S and NaCl. They observed a dependence of the microstructure and the corrosion product formed. The corrosion product formed in the presence of H_2S is commonly FeS. They observed an enhanced corrosion rate at temperatures of 40 ^oC and 60 ^oC. The corrosion behavior of carbon steel X60, as reported by Li et al., (Li et al. 2014) explains the dependence on morphological structure as well as the stability of the corrosion product. They observed a decrease in corrosion rate with a slight increase in H_2S concentration in the H_2S-CO_2 system. With a further increase in H_2S concentration, an elevation in corrosion rate was found. The phenomenon, as explained by them, was due to the fall of loosened corrosion film and hence exposure of the steel surface to the corrosive environment (Wen et al. 2018). Fatah et al. (Fatah et al. 2011) studied corrosion behavior for carbon steel X52 by carrying out electrochemical studies in sulfide and CO_2 medium. They observed an increase in corrosion rate with sulfide ion concentration increase and a tendency for pitting corrosion in the presence of sulfide ions. Liu et al. (Liu et al.

2023) compared the effect of H_2S and CO_2 in the presence of saturated brine and saturated vapor for low alloy pipeline steel. They reported that the corrosion effect of H_2S/CO_2 in saturated brine was more than H_2S/CO_2 in saturated vapor due to the formation of different corrosion products (Nešić et al. 2009). A Corrosion study on carbon steel 1018 in hydrogen sulfide at a low level in the presence of CO_2 was carried out by Choi et al. (Choi et al. 2011). They observed a rapid corrosion rate reduction at pH 3 and pH 4 when 100 ppm H_2S was added to CO_2. This was explained to happen due to the formation of corrosion product FeS as a thin film on the metal surface, eventually suppressing the dissolution reaction at the anode (Zhao et al. 2003). Qi et al. (Qi et al. 2014b) studied the temperature effect on carbon steel corrosion in H_2S medium. The corrosion rate was observed to increase initially with elevation of temperature, whereas with further increase in temperature, there was a decrement in the corrosion rate (Ren et al. 2005; Yin et al. 2008). Carbon steel corrosion was investigated in the presence of CO_2 and H_2S environment by Kvarekval et al. (Kvarekval et al. 2005). The partial pressures of CO_2 and H_2S are 10 bar and 30 bar, respectively. The experiments were conducted at 25 °C and 80 °C under flowing conditions with flow velocities of 1, 3, and 5 m/s. A higher corrosion rate was observed in the absence of H_2S due to the absence of a protective corrosion product layer. Pitting corrosion was observed at 5 m/s flow velocity (Kvarekval et al. 2005). The carbon steel corrosion mechanism in the presence of an H_2S-CO_2 environment is reported to depend on temperature. A systematic study of carbon steel corrosion (AISI I020) in the CO_2-H_2S environment revealed an increased corrosion rate due to H_2S. According to them, H_2S hinders the formation of iron carbonate on the metal surface and, in replacement, accelerates the formation of a porous iron sulfide layer. The porous layer cannot protect the steel surface from the corrosive species that contact the surface, eventually accelerating the corrosion rate. Also, under

flowing conditions, the product layer is carried away, inducing the general and localized corrosion of the carbon steel (Zhang et al. 2022). The key literature on CO_2-H_2S corrosion of carbon steel is shown in Table 2.7.

Table 2.7 Key literature on CO_2-H_2S corrosion of carbon steel

Material	Corrosion Environment	Experimental Conditions	Experimental Methods	Key Findings	Reference
API 5L X52	H_2S-CO_2 environment in presence of NaCl	pH: 5.5 NaCl concentration: 1, 3.5, 5 wt% Temperature: 40, 60, 80 ^oC H_2S concentration: 100, 200 ppm	LPR, EIS, SEM-EDS	1. CO_2 corrosion behavior dependent on microstructure 2. At 100 ppm H_2S concentration, the production of corrosion product FeS inhibited CR 3. At 200 ppm H_2S concentration, the CR increased due to defects in corrosion product	Abadeh et al.
API X60	H_2S-CO_2 environment in presence of NaCl	NaCl concentration: 5 wt% Temperature: 60^oC CO2 Concentration 10 mmol/L	WL, LPR, EIS, SEM	1. CR rate decreased with initial increase in H_2S concentration in the range of 0-0.2 mmol/l 2. Increase in H_2S concentration further (0.8-4mmol/L), increased the CR	Li et al. (Losey and Kelly 2007)
X52	H_2S-CO_2 environment in the presence of NaCl	NaCl concentration: 3% Temperature: 40^oC	LPR, EIS, SEM	5. CR increased more than 3 times with an increase in sulfide ion concentration from 0 to 400 ppm 6. Corrosion film produced also contributed to increasing CR	Fatah et al. (Fatah et al. 2011)
Low alloy pipeline steel	Vapor saturated H_2S-CO_2 & H_2S-CO_2-saturated brine environment	Temperature: 75^oC H_2S partial pressure: 0.09 MPa CO_2 partial pressure: 0.64 Mpa	WL	3. CR in vapor saturated environment was lower than in brine saturated environment in constant similar H_2S-CO_2 conditions 4. Low alloy pipeline steel was free of pitting corrosion 5. Corrosion products in vapor saturated H_2S-CO_2 environment were mackinawite and greigite while in the other one was mackinawite and pyrrhotite	Liu.et.al. (Liu et al. 2023)

2.4.4.2. Corrosion of Carbon Steel in the Presence of CO_2- Hac

Yaro et al. (Yaro et al. 2015) reported the corrosion rate of mild steel alloy X65 in produced water containing acetic acid and CO_2. They conducted potentiodynamic polarization and weight loss methods to determine the corrosion behavior. They performed a regression analysis to find the optimal corrosion rate in terms of temperature, pH, and rotation speed. In the absence of protective film, 45.5 °C, 4.8 pH, 2178.5 ppm acetic acid concentration, and in the presence of protective film, 68.7 °C and 7.9 pH are the optimum conditions to achieve optimal corrosion rate. Martinez et al. (Olvera-Martínez et al. 2018) reported an electrochemical method for establishing the effect of acetic acid on the corrosion of carbon steel API X52 in the presence of CO_2 and NaCl under turbulent conditions at 60^{o}C. A significant increase in the corrosion rate was observed with an increase in acetic acid concentration. The effect of acetic acid due to the contribution of hydrogen ions by acetic acid was reported by Okafor et al. (Okafor and Nesic 2007). They reported the corrosion behavior of two carbon steels, X65 and C1018, in the presence of an aqueous medium containing acetic acid in the presence of NaCl and a vapor medium containing acetic acid in the presence of CO_2. An elevation in corrosion rate was observed with an increase in acetic acid concentration due to an increment in the cathodic reaction rate. Dugstad et al. (Arne Dugstad 2006) assumed that the contribution of CO_2 towards the cathodic reaction rate takes place in two different paths. He claimed that H_2CO_3 is reduced directly and dissociates to be a source for H^+ ions. It was observed that CO_2 does not have any significant effect on the anodic reaction at lower acetate concentrations and higher pH range, pH 4-6. The effect of acetic acid and CO_2 on mild steel was investigated by George et al. (George and Nešic 2007). They reported the effect of acetic acid on the mild steel corrosion rate to be more distinct at higher temperatures. In contrast, catastrophic corrosion was expected to occur at

high concentrations of acetic acid. The key literature on CO_2-H_2S corrosion of carbon steel is presented in Table 2.8.

Table 2.8 Key literature on CO_2-HAc corrosion of carbon steel

Material	Corrosion Environment	Experimental Conditions	Experimental Methods	Key Findings	Reference
API 5L X52	Acetic acid solution saturated with CO_2 in presence NaCl	Temperature: 60°C NaCl concentration: 3 wt. % Acetic acid concentration: 100 ppm Flow condition: Turbulent, 1, 100, 1000, 3000, 5000 pH: 4.27, 3.89	LPR	1. CR was observed to increase in addition of acetic acid to CO_2 environment 2. In absence of HAc the corrosion reaction was mass transfer controlled	Martinez et al., (Olvera-Martínez et al. 2018)
API X65	Acetic acid solution saturated with CO_2 in presence of NaCl	pH 3, 4, 5, 6, 7.5, 8, 8.5 Temperature: 40, 50 & 60°C HAc concentration: 1000, 2000 and 3000 ppm Turbulent condition at 1000,1250, 1500 rpm NaCl concentration: 3.5%	WL, LPR, EIS	1. Optimum conditions for optimal corrosion rate were obtained using regression analysis. 2. Corrosion study of the carbon steel was determined at the optimum conditions 3. The primary corrosion product of API X65 mild steel is ferrous carbonate	Yaro et al. (Yaro et al. 2015)

Continued…

Carbon Steel	Saturated CO_2 –Hac in NaCl solution	NaCl concentration: 1, 3.5 wt. % CO_2 pressure: 0.5, 2, 5 bar HAc concentration: 0,0.1,1,10 mM	LPR, EIS	1. Dissociation of H_2CO_3 is a source of H^+ ions. 2. Below 50-60 °C, CO_2 hydration is the rate determining step. 3.HAc serves as an additional source of H^+ ions	Dugstad (Arne Dugstad 2006)

2.4.4.3 Corrosion of Carbon Steel in the Presence of CO_2, H_2S, and Hac

Talukdar et al. (Talukdar and Rajaraman 2020) investigated the corrosion behavior of mild carbon steel in acetic acid and H_2S medium in the presence of CO_2. By employing polarization and electrochemical impedance spectroscopy, they observed the corrosion rate to increase initially with an increase in acetic acid concentration, but a further increase in HAc concentration decreased the corrosion rate. They explained the increase in corrosion rate due to an elevation in cathodic current density at lower acid concentrations. Whereas at higher acid concentrations, the decrement in anodic current density explains the reduction in corrosion rate.

Kvarekval et al. (Kvarekvål and Svenningsen 2017) carried out corrosion studies by weight loss method for carbon steel UNS K03014 in acetic acid and H_2S in the presence of CO_2 and NaCl at 25 °C and 90 °C. They reported the FeS corrosion film to be more protective at 90 °C than 25 °C and also varying corrosion rates in the presence and absence of acetic acid. Veloz et al. (Veloz and González 2002) carried out work on the corrosion behavior of carbon steel SAE 1018 in acetic acid solution in the presence of H_2S. According to their report, the corrosion product film was not observed during the impedance spectroscopy analysis. This was explained by the presence of an

adsorbed complex containing HAc as well as chlorides, along with the presence of acetate ions that were observed to control the corrosion process and eventually prevent the formation of a passive film in spite of the presence of H_2S. The key literature on CO_2-HAc-H_2S corrosion of carbon steel is given in Table 2.9.

From the literature discussed, it is obvious that several works are reported on the individual effects of CO_2, H_2S, and acetic acid on the carbon steel corrosion. However, very limited work is reported on the combined effect of all three components on carbon steel.

Table 2.9 Key literature on CO_2-HAc-H_2S corrosion of carbon steel

Material	Corrosion Environment	Experimental Conditions	Experimental Methods	Key Findings	Reference
Mild steel	CO_2-H_2S-HAc	Temperature: Room temperature NaCl concentration: 3.5 %	WL, EIS, LPR, FESEM	2. The CR increased with increase in HAc concentration initially but with further increase in concentration the CR was decreased. 3. At lower acidic conditions the cathodic current density was increased 4. At higher acid concentration the anodic current density decreased	Talukdar et al. (Talukdar and Rajaraman 2020)
Carbon steel UNS K03014	CO_2-H_2S-HAc	Temperaure: 25, 90 ^oC	WL, SEM	2. The corrosion film formed was FeS 3. The corrosion film was observed to be more protective towards the metal from further corrosion at 90^{o}C in comparison to 25^{o}C	Kvarekval et al. (Kvarekvål and Svennings en 2017)

2.4.5. Corrosion of Various Grades of Carbon Steel

The effect of CO_2-H_2S and acetic acid on carbon steel corrosion is discussed in the previous section. Most of the studies focused on the corrosion behavior of a specific grade of carbon steel in the aforementioned medium. However, only limited works are available on the corrosion behavior of the various grades of carbon steels in the given solution of interest, which is discussed below.

It is reported, based on electrochemical and material loss studies, that the corrosion rate of X60 is higher than that of X52 in saltwater solution in the presence of CO_2. Lower ferrite content in X60 is assumed to be responsible for this behavior (Rihan 2013). Clover et al. (Clover et al. 2005) studied the effect of corrosion resistance of carbon steels with respect to their physical and chemical properties, including X52 and X60, in the presence of oil field formation water. According to them, the difference in elemental composition of the carbon steels was not correlated with the corrosion resistance. However, they reported the dependence of corrosion resistance with respect to the microstructure of the carbon steels. It was observed that ferrite and pearlite bands were present in both X52 and X60 steels, although in X52, they were evenly distributed, and in X60, coarse bands were present. Further, the nature of the corrosion is also different, i.e., pitting corrosion was observed in X52, whereas X60 experienced uniform corrosion (Clover et al. 2005). Li et al. (Li et al. 2019) reported the corrosion behavior of carbon steel C1010 and C1018 in a saturated CO_2 environment in the presence of NaCl at varying temperatures. They reported increased corrosion rate followed by stabilization at constant NaCl concentration for temperatures below 60 °C. At temperatures higher than 60 °C, the corrosion rate initially increases, and after reaching maxima, it continues to decrease. They explained this to be a formation of a dual layer of $FeCO_3$ scale. They also proposed a mechanism for the corrosion product formation on the steel

specimen, with respect to temperature and NaCl concentration in a saturated CO_2 medium. To the best of our knowledge, very limited works are reported on the comparison of the corrosion behavior of carbon steels X52 and X60.

2.5. Modelling of corrosion Reaction Mechanism using Reaction Mechanism Analysis

In the previous sections we discussed about the dissolution behavior of metals in different corrosive environments as reported earlier by numerous researchers. Some of the reported studies included corrosion mechanisms, predicted based on the experimental observations and characterization results obtained (Nešić et al. 2009; Qu et al. 2017; Kahyarian et al. 2020). However, a detailed study of the corrosion reaction mechanism including kinetic behavior is not explored. The basis of this approach is to formulate a mathematical model based on a predicted reaction mechanism and then validate the model using impedance data obtained from EIS experiments (Bechet et al. 1977; Epelboin et al. 1981). EIS is widely applicable for analyzing the electrode-electrolyte interface characteristics and reactions undergoing under similar conditions. Simple reactions can be modelled using EEC fitting, but more complex systems cannot be analyzed using this approach. The reaction mechanism analysis can be applied to complex systems to determine the reaction mechanism, providing quantitative information associated with the reaction. A single system can be modelled using one or more than one mechanism. The formulated model is optimized using sequential programming. The simulated data obtained from the model is validated with experimental data concerning the EIS plot features. The preferred model will be the one that can be validated with the optimal number of parameters. A library of patterns that corresponds to various mechanisms will be required in order to find the choose the preferred mechanism (Jeevan Maddala, Krishnaraj Sambath, Vinod Kumar). Presently, only a few groups are working on the reaction mechanism analysis. Some of the reported works are discussed in this

section. Paul et al. determined the dissolution kinetics of cobalt in the presence of alkaline glycine electrolyte. They proposed a reaction mechanism with four adsorbed intermediates comprising of glycine complex, or hydroxides/oxides of Co. According to their model, the dissolution rate via chemical pathway followed an increasing trend towards higher potential. However, at very high anodic overpotentials, the dissolution rate was constant and reached a saturation. The dissolution rate via the electrochemical pathway exhibited varying behavior. The highest dissolution rate was observed at intermediate overpotentials, whereas a low dissolution rate was observed at both high and low overpotentials (Paul and Srinivasan 2020). Prasad et al. predicted the dissolution model of Cu in arginine- H_2O_2 solution. A two-step dissolution mechanism was proposed with an adsorbed intermediate. According to their mechanism, the corrosion product film formed on the surface of Cu was not stable. Potentiodynamic polarization data revealed active dissolution of the metal that agreed with the RMA findings (Nagendra Prasad et al. 2009). Anodic dissolution mechanism of carbon steel in the presence of ammonium chloride was reported by Baranwal et al. They proposed a multi-step mechanism with three adsorbed intermediates. The reaction mechanism consisted of two electrochemical and one chemical path. Kinetic parameters including surface coverage was determined through the RMA. Dissolution via chemical pathway was predominant at lower overpotentials whereas, electrochemical reaction was predominant at higher overpotentials (Baranwal and Prasanna Venkatesh 2017). Since the reaction mechanism approach includes critical analysis of the electrochemical data and validation of the experimental results are performed based on the model, it created an interest in working with this approach The reaction mechanism analysis approach is also applied in other fields such as catalytic reaction, fuel cell mechanism, medical implants etc. (Amrutha et al. 2017, 2018; Ranjith et al. 2018; Ghelichkhah et

al. 2023). Hence, we focused on the RMA approach to determine the corrosion mechanism in two diversified fields, such as the semiconductor industry and the oil and gas industry.

Through the extensive literature survey carried out based on our research area, the following findings are summarized below:

a) The chemical mechanical polishing aspects of Mo in H_2O_2 are reported by researchers, which suggests the optimal slurry condition for Mo polishing is at an alkaline pH range and 2.5 % H_2O_2 concentration.

b) The Mo polish rate to etch rate ratio in H_2O_2 solution is not at the desired level to minimize the CMP issues, such as dishing and erosion.

c) Carbon steel corrodes more in the presence of CO_2-H_2S and acetic acid compared to when exposed only to the individual components.

d) Carbon steel corrosion in the given solution of interest is strongly influenced by the grade of carbon steel

e) RMA is a rigorous but useful approach to investigating the metal-electrolyte interaction at the surface.

2.6. Lacunae in the Literature Survey

From the critical understanding of the works of literature provided the following lacunae

i. Despite the availability of CMP studies on Mo in the presence of H_2O_2, the dissolution behavior of Mo has not been studied extensively. Although the dissolution mechanism is suggested, it is mainly based on the ex-situ surface characterization techniques, such as XPS, and based on thermodynamic properties. RMA is not employed to investigate the faradaic and non-faradaic reactions occurring at the metal-electrolyte interface

ii. The preliminary results from our research group show that $KMnO_4$ is also a suitable oxidizer for Mo. However, the mechanistic reaction pathway of Mo dissolution in $KMnO_4$ solution is yet to be studied.

iii. In spite of several works reported on the corrosion behavior of carbon steel in the presence of CO_2-H_2S and acetic acid, how the various grades of carbon steel react to the given corrosive medium is not extensively studied. In particular, the kinetics of these systems were not studied. The factors that are attributed to the difference in corrosive behavior observed for various grades of carbon steel are not clearly identified in the literature.

In the next Chapter, we will present the materials used for the experiments performed to achieve the objectives of the thesis work and experimental procedures in detail.

CHAPTER 3

Chapter 3: Materials and Experimental Procedures

3. Experimental Details

This chapter includes a detailed description of the materials used in the experiments of the present investigation, the experimental protocol, and the reaction mechanism analysis approach implemented to conduct this research.

3.1 Materials

99.9 % pure Mo (Tecnisco, India) was purchased and fabricated as per the requirements of the experiment for the initial part of the thesis work (as applied to Chapters 5 and 6).

Two different grades of carbon steel samples API 5L X52 and API 5L X60, were considered in this study for the next part (used for experiments in Chapter 7). The compositions of the same are mentioned in Table 3.1.

Table 3.1. Chemical composition (wt. %) of carbon steel API 5L X52 and API 5L X60

Components of CS (%)	X52	X60
C	0.16	0.16
Mn	1.6	1.6
Si	0.15-0.5	0.45
S	0.007	0.01
P	0.025	0.02
Cu	0.03	-
Ni	0.03	-
Cr	0.025	-
Mo	0.08	-
V	0.06	0.08
Nb	0.04	0.05
Ti	0.02	0.04
Sn	0.02	-
B	0.0005	-
N	0.014	-
Al	0.06	-
Fe	Rest	Rest

The microstructure of the carbon steel samples was analyzed using field emission scanning electron microscopy (FESEM). For the microstructure analysis, the metal samples were polished using emery sheets of grades 180, 320, 600, 800, and finally 1000. After polishing, the metal samples were thoroughly cleaned using a sonicator and treated using Nital solution following the ASTM standard E407. Pure Mo (99.9%) (Tecnisco, India) was purchased and fabricated as per the requirements of the experiments.

All the chemicals used in the experiments, such as NaCl (Himedia), acetic acid (Himedia), sodium thiosulphate (Loba Chemie), hydrochloric acid (Himedia), antimony trioxide (Himedia),

stannous chloride, hydrogen peroxide (30 %, Loba Chemie, India) and potassium hydroxide (Himedia, India), potassium permanganate (Loba Chemie, India) are of AR grade. Sodium thiosulfate is used instead of the direct supply of hydrogen sulfide gas to avoid laboratory hazards. The correlation of sodium thiosulfate to hydrogen sulfide is presented in equations A1-A4 in the Appendix following Kappes et al. (Kappes et al.). All the experiments for Objective 3 (as mentioned in Chapter 7) were carried out in an autoclave reactor (4848 instrument controller, PARR instrument company, USA). The autoclave reactor was made of Hastelloy with a permissible pressure of 150 bar at 22 ºC. The schematic of the experimental setup is illustrated in Figure. 3.1 and a picture of the experimental setup along with the electrode assembly is shown in Figure. 3.2.

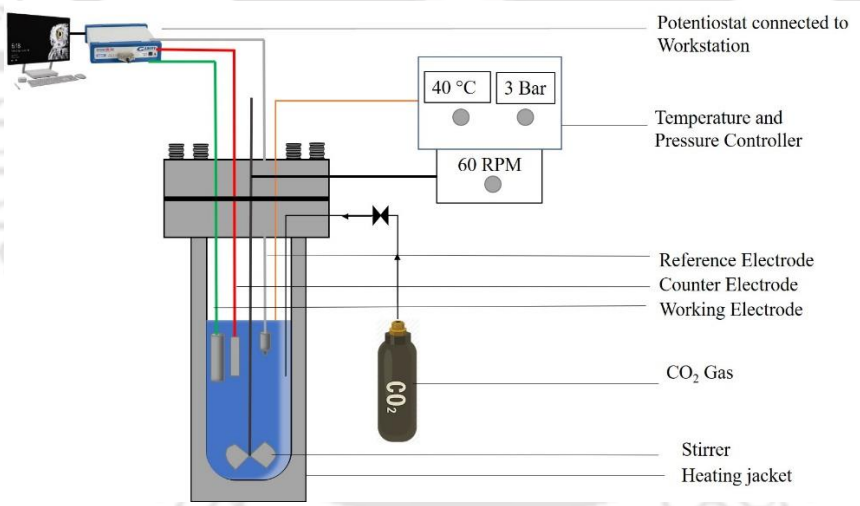

Figure. 3.1 Schematic of experimental setup

Figure. 3.2 Experimental setup showing (a) electrode assembly, (b) overall setup with temperature and pressure controllers

3.2. Experimental Procedures

3.2.1. Etch Rate Measurement

The etch rate measurement was implemented for experiments discussed in Chapters 5 and 6. Preceding all the experiments, the metal specimen was polished using emery sheets of different grades and micro-polished using alumina powder. The polished samples were then degreased with acetone and thoroughly cleaned using Millipore water (resistivity: 18.2 MΩ cm) produced in a Millipore filtration unit (Elix-3, Milli Q, M/S Millipore, USA). A cylindrical Mo specimen (7 mm diameter × 9 mm height) was used for the etch rate experiment. After the sample preparation, the metal specimen was exposed to 0 wt. %, 1 wt. %, 2.5 wt. %, and 5 wt. % H_2O_2 solution at pH 10 for 15 mins. After the experiment, the specimen was collected, cleaned, and dried. The final weight

of the sample was measured in a weighing balance (0.1 mg accuracy, Sartorius BSA224S-CW, Germany), and the etch rate was calculated from the weight loss.

$$Etch\ Rate\ (nm/min) = \frac{Change\ in\ weight\ (g)\times 10^7}{Density\ (g/cm^3)\times time\ (min)\times \text{surface area}\ (cm^2)} \qquad 3.1$$

3.2.2 Polish Rate Measurement

The polish rate experiment was performed for Mo in $KMnO_4$ solution (experiment performed for Chapter 6). A Mo coupon dimensioned to 25 mm in diameter was fabricated for the experiment. The polishing pads used for the experiment were obtained from Buehler (Texmet C PSA pads) of diameter 8 in. The experimental setup (benchtop Labopol-20/Laboforce-50 polisher, Struers, USA) for the polish rate experiment is illustrated in Figure 3.3.

Figure 3.3 Experimental setup including CMP machine for polish rate experiment

3.2.3. Pourbaix Diagram

The Pourbaix plot for Mo-H_2O system was constructed using Medusa® software (applied for Chapter 5).

3.2.4. Electrochemical Experiments

The experimental setup used for Aim 1 (as implemented for Chapter 5) and Aim 2 (mentioned for Chapter 6) is shown in Figure 3.4. Mo embedded in Teflon was used as the working electrode. Ag/AgCl (3 M KCl) from Metrohm was used as the reference electrode, and Platinum wire from Metrohm was used as the counter electrode. The sample preparation method followed for the electrochemical experiments is the same as that described in Section 3.2.1. The electrochemical set-up used for the electrochemical measurement experiments (used in Chapter 7) consisted of a three-electrode cell with a cylindrical carbon steel specimen as the working electrode (1 cm diameter and 1.3 cm height), platinum (P19883, ultradeg high-pressure Corr Instruments, USA) was used as the counter electrode and Ag/AgCl (3 M KCl) (P19882, ultradeg high-pressure Corr Instruments, USA) were used as the reference electrode. A potentiostat workstation (1010, Gamry Instruments Inc., USA) was used to conduct all the electrochemical experiments. All the experiments for Objective 3 (used in Chapter 7) were performed in an autoclave, as shown in Figure 3.1 and Figure 3.2.

Figure. 3.4 Electrochemical experiment set-up

3.2.4.1. Open Circuit Potential (OCP)

The open circuit potential was measured before any electrochemical measurements to ensure the system's stability against the Ag/AgCl (3 M KCl) electrode. The OCP was performed till the system reached a stable potential.

3.2.4.2. Cyclic Voltammetry Study

The cyclic voltammetry of the Mo metal sample (used in Chapter 5) was performed by linear potential sweep between -0.25 V to +0.25 V (w.r.t. OCP) at a scan rate of 100 mV/s.

3.2.4.3. Potentiodynamic Polarization Measurements

The anodic dissolution of Mo metal was measured by performing potentiodynamic polarization measurements from OCP to +500 mV at a scan rate of 1 mV/s (applied in chapters 5 and 6). Whereas, the scan was performed at a potential range of -0.25 V to + 0.5 V vs. OCP, with a scan rate of 1 mV/s for the carbon steel specimen (applicable to chapter 7).

3.2.4.4. Electrochemical Impedance Spectroscopy (EIS) measurements

The EIS for Mo metal specimens in the presence of H_2O_2 and $KMnO_4$ was performed at various overpotentials such as 0.1V, 0.2 V, and 0.3 V (applicable for Chapters 5 and 6). EIS experiments for the carbon steel samples were conducted at OCP and various overpotential values (0.05 V, 0.15 V, and 0.25 V w.r.t OCP) (applicable for Chapter 7). The system was perturbed with an AC voltage of 10 mV rms between a frequency range of 100 kHz to 0.01 Hz with 10 points per decade.

3.2.5. Weight Loss Measurement

The corrosion rate of carbon steel samples in the presence of CO_2-H_2S-acetic acid and 3.5 wt. % NaCl was determined by weight loss measurement experiment (implemented in Chapter 7). Prior to the experiments, the metal samples that were dimensioned to 13 mm diameter and 3 mm thickness were polished using emery sheets of various grades (180, 320, 600, and 1000), followed by micro-polishing with alumina powder of grade 1 and 0.3 μm (Buehler, USA), finally following the ASTM E3 (Standard Guide for Preparation of Metallographic Specimens) method, degreased with acetone followed by thorough cleaning in a sonicator. The samples were immersed in the solution for 24 h. After the experiment, the solution was cleaned using Clarke's solution (ASTM standard G1-03, C3.1) and dried, and the final weight was measured. Clarke's solution is composed of concentrated hydrochloric acid, antimony trioxide, and stannous chloride.

$$CR = \frac{W \times K}{\rho \times T \times A} \qquad 3.2$$

Where CR is the corrosion rate (mm/year), W is the change in weight of test specimen (g), K is the K-factor constant (87500), ρ is termed as density (7.85 g/cc), time (h) expressed as T and the total surface area as A (cm^2).

3.3. Data Validation of EIS and Modelling Methods

3.3.1. Kramers Kronig Transform (KKT)

The impedance data obtained was validated by implementing the Kramers Kronig Transform (KKT) (Gamry) to determine the system's linearity, stability, and casualty. The KKT analysis is important in a way that it provides an independent analysis of the EIS data for validation. The Kramers Kronig correlations are more often the mathematical property or in a more elaborate way, integral equations, that provides a relation between the real and imaginary entities of a complex quantity. For example, in the present study, impedance termed as 'Z' is the complex quantity of a system under a promising condition of linearity, stability, and causality.

Linearity: It refers to the current response from the electrochemical cell, which should be assumed to be linear. To achieve this, the AC amplitude applied to the system should be very small.

Stability: To ensure the stability of an electrochemical system, the output current response should not vary with any change in the input signal w.r.t. time. Eventually, the electrochemical system subjected to analysis should be in a steady state. The important factors responsible for the stability of a system include the conditions of measurements and the frequency range.

Causality: The electrochemical cell used for the experiment should be kept within an enclosed shield to avoid any external disturbances. Also, the output response should be directly proportional to the applied input impulse.

Through the Kramers-Kronig correlation, integral equations are obtained which will help to attain the impedance spectrum of one part when another part of the measured data is known. The data can be received within the 0 to ∞.

$$Z_{\mathrm{Re}}(\omega)-Z_{\mathrm{Re}}(\infty)=\left(\frac{2}{\pi}\right)\int_0^{\infty}\frac{xZ_{\mathrm{Im}}(x)-\omega Z_{\mathrm{Im}}(\omega)}{x^2-\omega^2}dx$$

$$Z_{\mathrm{Re}}(\omega)-Z_{\mathrm{Re}}(0)=\left(\frac{2\omega}{\pi}\right)\int_0^{\infty}\frac{(\omega/x)Z_{\mathrm{Im}}(x)-Z_{\mathrm{Im}}(\omega)}{x^2-\omega^2}dx$$

$$Z_{\mathrm{Im}}(\omega)=-\left(\frac{2\omega}{\pi}\right)\int_0^{\infty}\frac{Z_{\mathrm{Re}}(x)-Z_{\mathrm{Re}}(\omega)}{x^2-\omega^2}dx$$

Where, Z_{Re} and Z_{Im} correspond to real and imaginary entities of impedance, respectively. ω and x correspond to angular frequencies. The real and imaginary impedance values obtained are further compared with the corresponding experimental values retrieved under the same constraints as mentioned above.

3.3.2. Electrical Equivalent Circuit (EEC) Analysis

The EIS plots in the electrochemical study help us to find out the reaction mechanism and physical as well as electrochemical processes that take place in the bulk solution and the metal-electrolyte interface. This is obtained by measuring the charge transfer resistance, electrolyte resistance, and polarization resistance, which includes diffusion resistance, electrical double-layer capacitance, etc. An electrical equivalent circuit simulation is performed to analyze the EIS data quantitatively. This method includes fitting the EIS data with an equivalent electrical circuit analog encompassing several electrical components for instance, inductor, resistor, capacitor, etc. A typical EEC model is represented in Figure 3.5. In the figure, R_1 is a resistance connected in series to a combination of a capacitor (C_1) and a resistor (R_2) in parallel. Mostly for electrochemical systems, R_1 corresponds to the solution resistance, C_1 indicates the double layer capacitance at the electrode-solution interface, termed as C_{dl}, and R_2 is the polarization resistance (R_p) of the system.

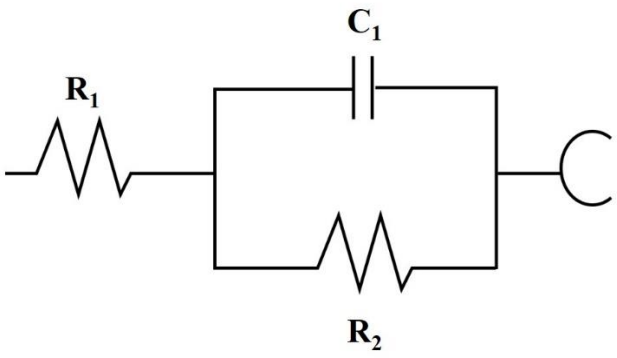

Figure 3.5 A typical Voigt circuit of EEC fitting

3.3.3. Reaction Mechanism Analysis (RMA)

Complex plane plots are obtained through the EIS experiments (Nyquist and Bode plots). The EIS data obtained can be analyzed using electrochemical equivalent circuit fitting. In the case of a simple Nyquist plot obtained, the modelling can be performed using elements such as capacitance, constant phase element, or inductance. However, only quantitative information can be drawn out using the EEC fitting. In most cases, satisfactory comprehensive information on the reaction pathway cannot be found using the EEC fitting. To investigate the reaction mechanism in detail, reaction mechanism analysis is performed. This process involves postulating a mechanism based on the EIS data observed, and the mechanism is simulated. The mechanism is accepted to depict the system under study if the simulated data obtained matches with the experimental data. The RMA parameters are obtained using sequential quadratic programming. There can be several mechanisms for a single system, and several patterns can also be obtained from a single mechanism. The choice of mechanism will be the closest matching pattern with the experimental data with the least errors. In case of good fitting of several models with the experimental data, the mechanism using least number of parameters and lowest error value will be selected.

To develop the mathematical model for the RMA, the following assumptions are considered

a) The double layer capacitance is fixed across the whole voltage range simulated.

b) A linear perturbation is applied (low AC voltage upto a few mV) neglecting the higher order terms.

c) The kinetic parameters and applied voltage are exponentially varied and depicts similar behavior like the tafel constants.

d) The forward reaction has a non-negative component, whereas the reverse reaction has a negative exponent.

e) The surface coverage of the adsorbed species on the specimen surface is restricted to unity following Langmuir adsorption isotherm.

To derive the mathematical model for the reaction mechanism analysis, let us consider the following reaction with both chemical and electrochemical steps for the dissolution of metal M. M is converted to M_{ad1}^{+} via the electrochemical step with reaction rate constant k_1. Since there is an exchange electron, this step is considered electrochemical. The species M_{ad1}^{+} can exist on the metal surface in the form of oxides, sulfides, chlorides, or hydroxides with a +1-oxidation state (Figure. 3.6). M_{ad1}^{+} is dissolved in the solution as M_{sol}^{+} with a reaction rate constant k_2. This step is a chemical dissolution with no electron exchange.

$$M \xrightarrow{k_1} M_{ad_1}^{+} + e \xrightarrow{k_2} M_{sol}^{+} \qquad 3.3$$

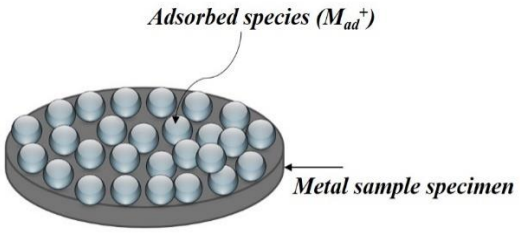

Figure. 3.6 Schematic diagram for adsorbed species on a metal surface

Applying an unsteady state mass balance over the adsorbed species θ_1

$$\tau \frac{\mathrm{d}\theta}{\mathrm{d}t} = k_1(1-\theta) - k_2\theta \qquad 3.4$$

Here τ is the total site per square unit of area. θ is the surface coverage of the species M_{ad1}^{+} and (1-θ) is the site remaining vacant. Since, an unoccupied site is required near the species M_{ad1}^{+} for the reaction to proceed.

The kinetic rate constant for a respective reaction is expressed as

$$k_i = k_{i0} e^{b_i V} \qquad 3.5$$

b_i can be written as

$$b_i = \pm \frac{\alpha n F}{RT} \qquad 3.6$$

For equations 3.5 and 3.6, in the case of forward reactions, i is (1 - 2), and for reverse reactions, i is -1. V is the DC voltage, α is the transfer coefficient and with a magnitude within 0 - 1; n is the number of electrons involved. In anodic dissolution process, b is positive for forward reactions and negative for reverse reactions. F is Faraday's constant; T is temperature in K, and R is the universal gas constant.

Under steady state conditions, equation 3.4 will become 0, hence,

$$\tau \frac{\mathrm{d}\theta}{\mathrm{d}t} = k_1(1-\theta) - k_2\theta = 0$$

$$k_1(1-\theta_{ss}) = k_2\theta_{ss}$$

Solving the above equation,

$$\theta_{ss} = \frac{k_1}{k_1 + k_2} \qquad 3.7$$

This is steady-state fractional coverage. The subscript ss is used to indicate steady state. The rate constants evaluated here are at DC overpotentials.

For a Faradaic reaction, the unsteady-state current density can be written as

$$J = nFk_1(1-\theta) \qquad 3.8$$

Differentiating the above equation 3.8 will provide the Faradaic impedance at the interface between metal specimen and the respective electrolyte.

$$\frac{dJ}{dV} = nF\left[k_1\left(-\frac{d\theta_{ss}}{dV}\right) + (1-\theta_{ss})\frac{dk_1}{dV}\right]$$

$$\left(Z_{F,m/s}\right)^{-1} = R_{ct}^{-1} - nF\left[k_1\left(\frac{d\theta_{ss}}{dV}\right)\right] \qquad 3.9$$

Where, $R_{ct}^{-1} = nF\left[k_1(k_1 b_1 \theta_{ss})\right]$ 3.10

R_{ct}^{-1} is the charge transfer resistance.

At steady state equation 3.8 can be written as

$$J_{ss} = nFk_1(1-\theta_{ss}) \quad 3.11$$

The rate constant can be expressed using Arrhenius equation

$$k_i = k_{i0}e^{b_i V} \quad 3.12$$

Differentiating the above equation with respect to V,

$$\frac{dk_1}{dV} = k_{10}b_1 e^{b_1 V} \quad 3.13$$

This can also be written as,

$$\frac{dk_1}{dV} = k_1 b_1 \quad 3.14$$

Finally, the total impedance can be written as

$$Z_{total} = R_{sol} + \frac{1}{\left(Z_{F,m/s}\right)^{-1} + Y_0\left(j\omega\right)^{n_1}} \quad 3.15$$

In the above equation, R_{sol} is the solution resistance, Y_0 and n_1 are CPE parameters, ω is the angular frequency, and is termed as $2\Pi f$.

3.4. Characterization Techniques

3.4.1. Field Emission Scanning Electron Microscopy (FESEM)

The surface morphology of the metal specimen and corrosion product was captured by FESEM (Zeiss, Sigma, Germany) images. We can determine the type of corrosion and visualize product morphology through the FESEM analysis. To perform the analysis, the metal sample was polished using emery sheets (180, 320, 600, 800, and 1000 grit) followed by micro polishing using alumina powder on a Buehler pad. After polishing, the samples were thoroughly cleaned using Millipore water in a sonicator and dried. Finally, the samples were exposed to the corrosive environment for the stipulated time. Later, the sample was removed from the solution, cleaned using Clarke's solution, and the sample was ready to take the micrograph images.

3.4.2. Contact Angle Measurement

The contact angle measurement was performed to obtain the physical property of the metal specimen (implemented for experiment in Chapter 7). The measurement was performed in a Goniometer (HO-IAD-CAM-01B, Holmarc opto-mechatronics) using the sessile drop technique. A 2 μL liquid droplet was dropped on the sample specimen surface using a micropipette. The liquid droplet consisted of water, methylene iodide, and the solution used for corrosion study. Within 1s of the droplet settling, the contact angle was measured using a camera and the Holmarc software. The sample preparation for contact angle measurement is the same as discussed in Section 3.2.1.

3.4.3. X-ray Photoelectron Spectroscopy (XPS)

The composition and oxidation state of the corrosion product species produced were determined using XPS analysis. The XPS analysis was carried out in the ESCALAB Xi + model of Thermo Fisher Scientific Pvt. Ltd., UK, equipped with a monochromatic Al Kα X-ray source radiation of

1486.6 eV. The analysis was performed in an XPS plot size of 500 μm with a constant pass energy of 50.0 eV, 0.2 nm/s, and 2 mm × 2 mm were the sputtering rate and area, respectively. The analysis was performed at room temperature. The sample preparation is the same as discussed in Section 3.2.1. The metal specimen was exposed to the corrosive medium at 0.25 V (for carbon steel) and 0.3 V (for Mo) for 1 h to obtain the corrosion product. The XPS data was deconvoluted using Origin software.

The upcoming chapter discusses about the theoretical background of the experiments performed to achieve the objectives of the thesis work.

CHAPTER 4

Chapter 4: Theoretical Background Experimental Procedures

This chapter discusses the theoretical background of the experimental procedures implemented for the experiments performed in this thesis work.

4.1 Electrochemical Methods to Investigate Corrosion

The methods used to investigate the corrosion behavior of metals are discussed hereafter.

4.1.1. Open Circuit Potential (OCP)

The potential developed between two terminals of any electronic device when no external current is applied or flowing through it is the open-circuit potential. The variation of open circuit potential with time is determined by considering the potential between the electrodes immersed in the electrolyte (working electrode and reference electrode). OCP is also termed as the corrosion potential or mixed potential. The rapid change in corrosion potential indicates an enhancement in the anodic reaction, which eventually indicates the formation of corrosion film (Sahrani et al. 2008). The OCP determination with respect to varying time is important to understand the effect of the electroactive substance present in the electrolyte during the formation or disintegration of any chemical bond during its charge transfer state. Typically, before performing any electrochemical measurement, the OCP of that system is determined. An OCP plot, as reported usually, is illustrated in Figure. 4.1. The potential will stabilize after some time, as shown in Figure 4.1. However, the stability time varies with the system. Stable OCP means the working electrode has achieved equilibrium with the corrosive environment, and hence, further electrochemical measurements can be performed with the system. The corrosion current (I_{corr}), also termed the total current (I_{total}), is expressed as the summation of the oxidation current and reduction current. The potential corresponding to I_{corr} is termed as E_{corr}. The oxidation current is the absolute current

generated at the anode, which is the rate of electrons released from the metal surface ($M - ne^- \rightarrow M^{n+}$). Reduction current refers to the anodic current generated at the cathode and is the rate of electrons accepted by the aqueous species ($M^{n+} \rightarrow M - ne^-$). It is evident from this information that, at the corrosion potential, the rate at which electrons are released (formation of corrosion products) corresponds to the rate at which aqueous oxidants are removed from the aqueous solution (Mars G. Fontana 1987; Ahmed 2006; Ramanathan Srinivasan 2021).

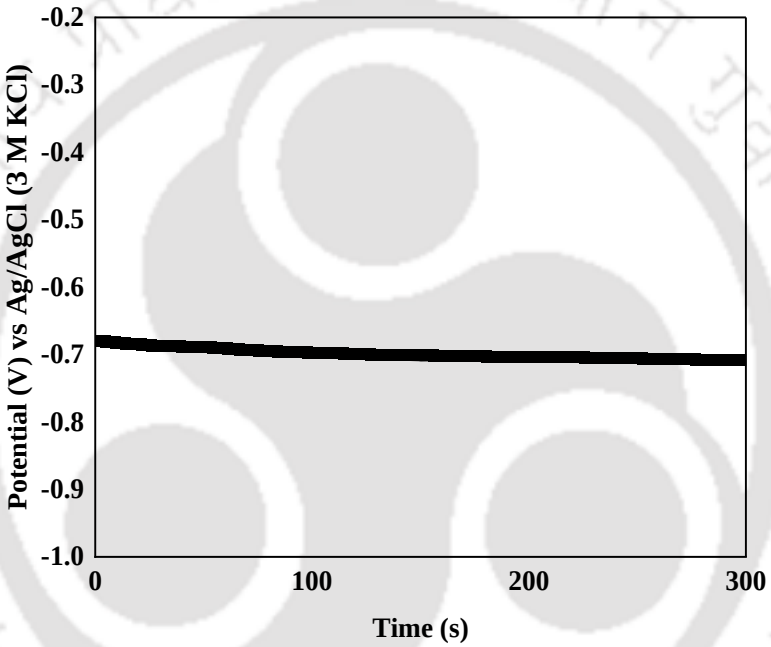

Figure 4.1 A typical potential vs. time plot representing the open circuit potential as a function of time

4.1.2 Potentiodynamic Polarization

Potentiodynamic polarization is an electrochemical method employing direct current in a large range of potential sweeping from negative to positive with reference to the OCP or corrosion potential so that the predominant electrochemical reaction will be either anodic or cathodic (Obot and Onyeachu 2018). The study of polarization is necessary to understand the corrosion behavior

and reactions associated with corrosion. When the electrochemical current density applied is measured against the potential of a corroding electrode at a condition where there is no oxidation-reduction reaction, the following mathematical relationship can be expressed by equation (4.1) (Kelly et al. 2002).

$$i = i_{corr}\left(\exp\left[\frac{2.3(E-E_{corr})}{\beta_a}\right] - \exp\left[\frac{-2.3(E-E_{corr})}{\beta_c}\right]\right) \quad 4.1$$

Where, β_a: Anodic tafel parameter

β_c: Cathodic tafel parameter

E_{corr}: Corrosion potential

I_{corr}: Corrosion current density

The equation 1.4 provides the basis for the electrochemical polarization technique when applied to the electrode at its corrosion potential. This relationship relies on the single charge transfer regulated anodic and cathodic reaction. Also, the rate of corrosion and susceptibility of specific materials towards corrosion is determined by this method. We have discussed I_{corr} and E_{corr} in the previous section (1.5.1). However, determining the I_{corr} at OCP is not possible as the net current is 0 ($I_{total} = I_{corr} = I_{oxidation} + I_{reduction}$). Meanwhile, at OCP, the polarity of both the anodic and cathodic current exists. Hence, the Icorr value can be evaluated by polarizing the system's potential away from its value marginally at OCP. This process includes sweeping the metal specimen from negative to positive potential w.r.t. OCP. The polarization curve or Evans diagram represents the potential vs. logarithmic absolute current plot at a steady state, as shown in Figure 4.2. In this figure, E_A signifies the anodic potential that is positive, and E_C represents the cathodic potential that will be negative. The polarization scan occurs from the cathodic to the anodic region since the cathodic reaction is non-destructive, whereas the anodic reaction is relatively destructive (Mars G.

Fontana 1987; Kelly et al. 2002; Ahmed 2006). The experimental polarization data is represented by plotting the current density against the applied potential, as shown in Figure 4.3.

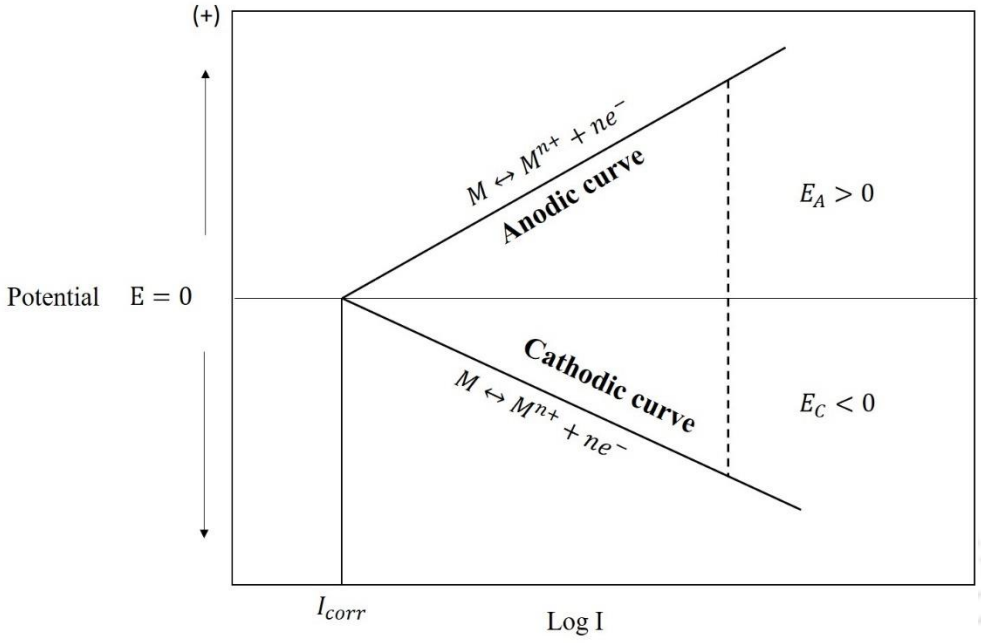

Figure 4.2 Evan's diagram of polarization

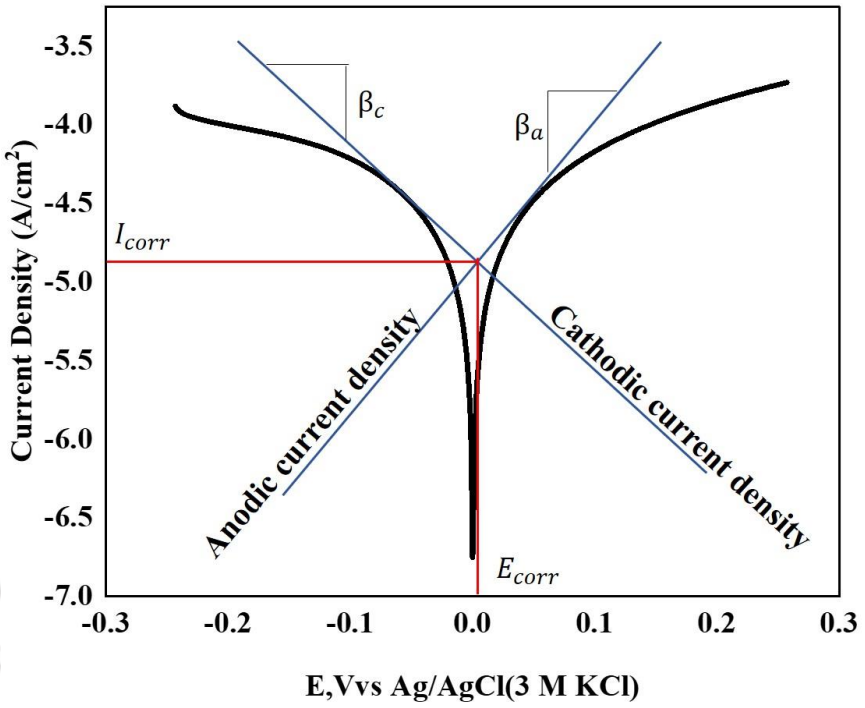

Figure 4.3 A Potentiodynamic polarization plot illustrating experimental data with anodic and cathodic components

The potentiodynamic polarization plot, as shown in Figure 4.3, represents the potential sweep from negative to positive potential. The slope of the tangent drawn to the cathodic curve is the cathodic current density, and to the anodic curve is the anodic current density. The corresponding current to the intersection of both tangents is the corrosion current, and the corresponding potential is the corrosion potential. Measuring the oxidation current and reduction current of a system is essential to interpret the corrosion kinetics of the system. Hence, with the assumption that the electron exchange reaction kinetics occurring at the metal surface is controlled by the cathodic and anodic processes. The following Butler-Volmer and Stern-Geary equations are derived to understand the kinetics of reactions occurring at the metal-solution interface (Ahmed 2006).

Butler-Volmer Equation

In the case of anodic polarization, we can consider a metal undergoing oxidation following the reaction

$$M \rightarrow M^{n+} + ne^{-} \qquad 4.2$$

When an electrode is connected to an external emf with a positive source, the superimposed potential or anodic overpotential η_A will be positive. This is referred to forward reaction. In such a condition, at $\eta_A>0$, the electrode is polarized toward the noble direction (Mars G. Fontana 1987; Ahmed 2006). For an activated ion to cross the energy barrier, the total activation energy will be expressed as

$$\Delta G_A^* = \Delta G - \beta nF\eta_A \qquad 4.3$$

However, the forward current is expressed as

$$i_f = nFf\alpha\left(\frac{N_s}{N_o}\right) exp\left[-\frac{\Delta G_A^*}{RT}\right]$$

Substituting ΔG_A^* from equation 1.6,

$$i_f = nFf\alpha\left(\frac{N_s}{N_o}\right) exp\left[-\frac{\Delta G - \beta nF\eta A}{RT}\right]$$

The exchange current density is expressed as,

$$i_o = nFf\alpha\left(\frac{N_s}{N_o}\right) exp\left[-\frac{\Delta G^*}{RT}\right]$$

Using the above equation, the forward current can be expressed as,

$$i_f = i_o exp\left[\frac{\beta nF\eta A}{RT}\right] \qquad 4.4$$

From the above it can be suggested that with the increase in anodic activation overpotential increases, the forward reaction rate is also increased.

In the reverse case, when the electrode is connected to the negative terminal, the reverse reaction rate is higher than the forward reaction rate. The activation energy associated with the forward

reaction will be higher than that of the reverse reaction. Hence, the cathodic reaction can be written as,

$$\Delta G_C^* = \Delta G^* + (1-\beta)nF\eta_C \qquad 4.5$$

The exchange current density associated with the cathodic reaction can be written as

$$i_o = nFf(C_S V_L)exp\left[-\frac{\Delta G_C^*}{RT}\right]$$

Substituting ΔG_C^* from equation 1.8 in the above equation, we will get the reverse current density as

$$i_r = nFf(C_S V_L)exp\left[-\frac{\Delta G^* + (1-\beta)nF\eta_C}{RT}\right]$$

This implies

$$i_r = -i_o exp\left[-\frac{(1-\beta)nF\eta_C}{RT}\right] \qquad 4.6$$

From the above equation, it can be concluded that, with the increase of cathodic overpotential, the cathodic reaction rate is also increased, eventually decreasing the forward reaction rate. Hence, experiencing the net current density i_{net}. Considering the two conditions,

At $i_f \gg i_r$ and $|i_r| \gg i_f$ is expressed as,

$$i_{net} = |i_a| - |i_c| = i_0\left\{exp\left[\frac{\beta z F\eta_A}{RT}\right] - exp\left[-\frac{(1-\beta)zF\eta_C}{RT}\right]\right\} \qquad 4.7$$

Equation 1.10 is termed as the Butler-Volmer equation and it is used to express the corrosion rate of a system (Ahmed 2006).

Where,

i_{net} is the total current density, A/cm^2

i_a is the anodic current density, A/cm^2

i_c is the cathodic current density, A/cm^2

i_0 is the exchange current density, A/cm^2

β is the constant, which is positive for the anode and negative for the cathode

z is the number of electrons exchanged

F is the Faraday's constant, Coulombs/mole

η_A is the anodic overpotential, V

η_C is the cathodic overpotential, V

R is the universal gas constant, 8.314 J/deg. mole

T is temperature, K

Further, two cases are discussed to get a better understanding of the over potential with respect to the current densities.

At higher over potential (η>0), anodic polarization is considered, and the cathodic current density i_c will be negligible. Such a condition can be explained as a reverse cathodic condition. Hence, the net current i_a^{net} will be equivalent to the anodic partial current density. Then, the Butler-Volmer equation will be reduced to

$$i_a^{net} = |i_a| = i_0 \left\{ exp \left[\frac{\beta z F \eta_A}{RT} \right] \right\} \quad 4.8$$

Hence, the Butler-Volmer equation relates the over-potential to the partial anodic current density when the anodic current density is high.

Similarly, when η<0, which is the case of large cathodic polarization. Here, the anodic partial current is negligible, and the net current is expressed as

$$i_c^{net} = -|i_c| = i_0 \left\{ exp \left[-\frac{(1-\beta) z F \eta_C}{RT} \right] \right\} \quad 4.9$$

From the above two conditions discussed, it can be concluded that the anodic or cathodic current densities contrast roughly with the exponential of over potential.

Stern-Geary Equation

The following assumptions are considered to simplify the Butler-Volmer equation.

- The potential is deviated close to the corrosion potential, Ecorr, in both positive and negative directions so that the output curve is almost straight line with unit resistance as the slope.
- The exponential term from Equation 1.11 is expanded following Taylor's series expansion, and the higher-order terms are neglected. After simplifying and further rearranging, the Stern-Geary equation is obtained and is expressed as follows,

$$I_{corr} = \frac{\beta_a \beta_c}{2.3\,(\beta_a+\beta_c)} . \frac{\Delta i}{\Delta E} \qquad 4.10$$

Where,

I_{corr} is the corrosion current, A

β_a is the anodic Tafel slope, mV/decade

β_c is the cathodic Tafel slope, mV/decade

Δi is the applied current, mA

ΔE is the potential difference, mV

For most electrolyte systems, β_a varies from 60 to 120 mV/decade. β_c is greater than 60 mV/decade. Hence, by assuming these values, corrosion rate estimates can be made within a factor of two. The polarization resistance R_p (kΩ) is given by,

$$R_p = \frac{\Delta i}{\Delta E} = \frac{\beta}{I_{corr}}$$

Where, $\beta = \frac{\beta_a \beta_c}{2.3\,(\beta_a+\beta_c)}$

4.1.3 Cyclic Voltammetry

Cyclic voltammetry is an established method to determine the oxidation and reduction behavior of any redox-active system. It provides substantial information on the thermodynamics and kinetics of heterogeneous oxidation-reduction reactions and adsorption processes. For the CV experiment, the working electrode is scanned with respect to the reference electrode from the starting potential to a switching potential and then returns to the final potential. During the scanning, an oxidation and reduction reaction will occur if the electroactive system undergoes any electron transfer within the respective potential range. The consequent current response, when plotted against the potential, a CV plot will be formed. The characteristic peaks formed in CV are due to the formation of a diffusion layer on the working electrode surface. The scan rate ascertains the time frame of the CV experiment. Linearly scanned potential as a function of time and the potential range that is traversed per unit of time is interpreted as the scan rate. The higher the scan rate, the lesser the experimental time frame. CV is recognized as a unique method for the kinetic analysis of electrochemical reactions due to its adjustable time frame across numerous orders of magnitude. The time-dependent potential plot is illustrated in Figure 4.4. The plot demonstrates the triangular waveform of the CV plot with the starting potential E_S, where the scanning starts and the forward scan runs till E_{SW}, the switching potential. From E_{SW}, reverse scanning takes place, and it stops at the final potential E_P. Figure 4.5 shows a typical CV plot showing cathodic and anodic peak currents I_{PC} and $I_{PA,}$ respectively. The curve corresponding to I_{PC} is a cathodic curve, and the one corresponding to I_{PA} is an anodic curve.

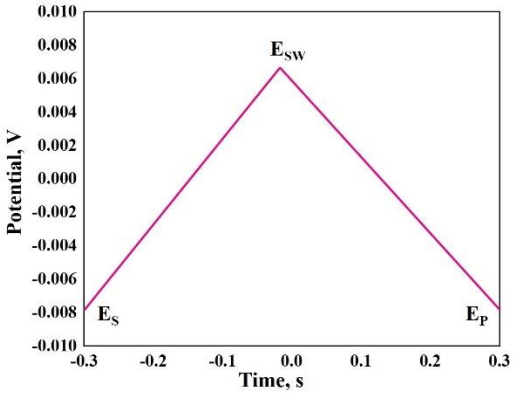

Figure 4.4 Potential vs. time plot for cyclic voltammetry experiment

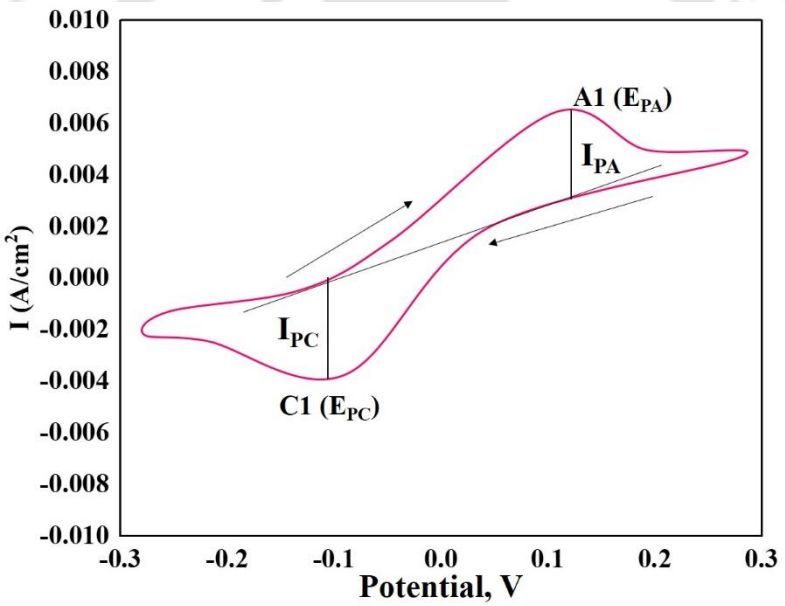

Figure 4.5 A typical cyclic voltammetry measurement plot showing anodic and cathodic current peak

4.1.4 Square Wave Voltammetry

Square wave voltammetry is defined as a differential technique with a large amplitude. In this method, a waveform is applied to the working electrode. The waveform comprises a symmetrical square wave that is superimposed on a base staircase potential. While a square wave cycle is run, the current is examined twice. First, sampling is performed at the end of the reverse pulse. Due to

the very large modulation amplitude in the square wave, the reverse scan causes a reversible reaction of the product that is formed during the forward scan. The square wave data is plotted, taking the difference between the two measurements with respect to the staircase potential. Having very little experiment time is the key advantage of square wave voltammetry. The effective scan rate is obtained by the product of the square wave frequency and the step height. So, if an experiment is performed at 50 Hz with a step size of 10 mV, then the effective scan rate will be 0.5 V/s. This will drastically reduce the analysis time, i.e., within a few seconds, the measurement will be over. This is helpful for many time-dependent processes, including the kinetic study of electrochemical reactions (Zachowski et al. 1985; Wang 2006). Figure 4.6 (A) shows the potential modulation plot of square wave voltammetry, and (B) shows a single potential cycle. The figure shows the forward and reverse sampling period, square wave amplitude (A_{sw}), scan increment (ΔA), duration of a potential step (ξ), and duration of two pulses (t_P). A typical square wave voltammetry plot with reversible current and voltage is illustrated in Figure 4.7 showing forward current (I_{fwd}), reverse current (I_{rev}), and differential current (I_{diff}).

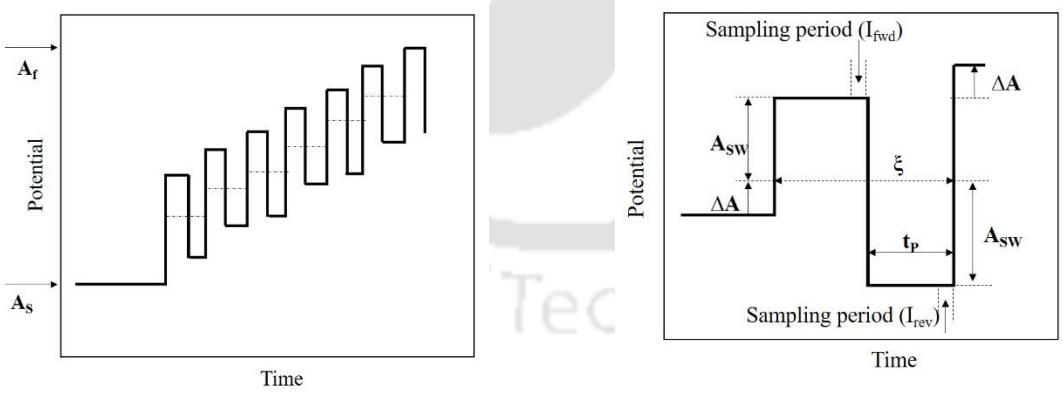

Figure 4.6 A.) Square wave voltammetry staircase potential modulation plot. B.) A single potential cycle

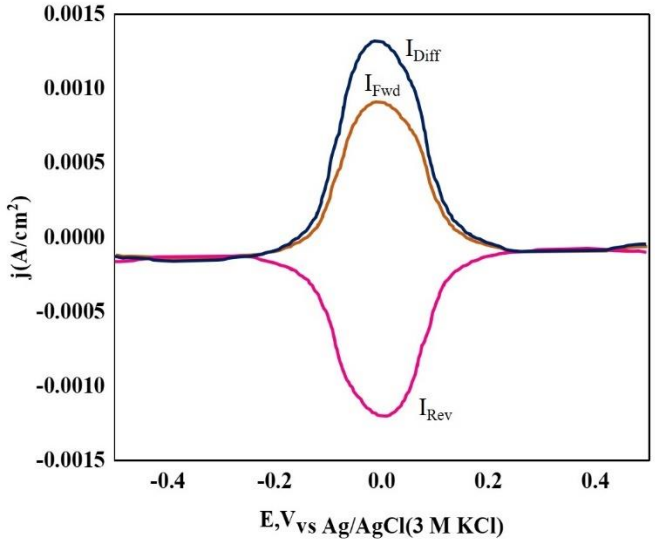

Figure 4.7 A typical Square wave voltammetry plot

4.1.5. Electrochemical Impedance Spectroscopy (EIS)

Electrochemical impedance spectroscopy has proved to be a very efficient method for investigating the corrosion mechanism of an electrochemical system. It is capable of mapping the behavior of the rate-determining step or measuring the corrosion resistance (charge transfer and polarization resistance). The precision offered by EIS measurement is the major advantage of using it for corrosion investigation. Resistance, as defined by Ohm's law ($V = IR$), is the capacity of an electrochemical system to resist the current flow in the system (circuit element). However, in real-life systems, more complex electrical circuits exist that are comprised of inductance, capacitance, etc. These cannot be explained through resistance. Hence, to explain the more complicated systems, impedance (Z) is used. Impedance is expressed as the function of frequency [$Z(f) = I/V$]. The relationship of impedance with various electrical components is listed in Table 4.1.

Table 4.1. Relationship of impedance with various electrical components

Component	Impedance	$I = f(V)$
Inductor	$Z = j\omega L$	$V = L\frac{dI}{dt}$
Capacitor	$Z = \frac{1}{j\omega C}$	$I = C\frac{dV}{dt}$
Resistor	$Z = R$	$V = IR$

In the above table, Z is impedance, j is an imaginary component ($\sqrt{-1}$), ω is the angular frequency, L is inductance, C is capacitance, I is current, V is potential, R is resistance and t is time.

The EIS method includes the measurement of the impedance of an electrochemical system by implementing a small sinusoidal AC perturbation to the system. Small AC perturbation is applied so that a pseudo-linear output is obtained.

The sinusoidal AC voltage input perturbation to an electrochemical system is mathematically expressed as,

$V(t) = V_0 \sin(\omega t)$

Where,

V(t) is the potential at time t (s),

V_0 is the amplitude of the applied signal

ω is the frequency in radians per second, and is expressed as 2πf

f is the frequency, Hz.

The frequency in EIS is measured from 100 kHz to numerous millihertz. EIS holds a special place in electrochemical techniques since, at a constant potential, it expresses the signal as a function of frequency (Losey and Kelly 2007).

The sinusoidal wave of output current is

$I(t) = A\sin(\omega t + \phi)$

Where, I(t) is the output AC current response, A is the maximum amplitude, ϕ is the phase shift.

Hence, the impedance of an electrochemical system is expressed as

$Z = \frac{V(t)}{I(t)}$

This implies,

$Z = \frac{V_0 \sin(\omega t)}{I_0 \sin(\omega t+\phi)}$

This can also be expressed as

$Z = Z_0 \frac{\sin(\omega t)}{\sin(\omega t+\phi)}$

Z_0 is the magnitude of impedance and is expressed as

$Z_0 = |Z| = [(Re(Z))^2 + (Im(Z))^2]^{0.5}$

and, $\phi = (argZ) = \tan^{-1}\left(\frac{Im(Z)}{Re(Z)}\right)$

Also, $Re(Z) = Z_0 \cos\phi$ and $Im(Z) = Z_0 \sin\phi$

The Euler's equation is $e^{j\phi} = cos\phi + jsin\phi$.

The impedance can also be expressed in complex form using the Euler's equation and is expressed as

$Z(\omega) = \frac{V(t)}{I(t)} = Z_0 e^{j\phi} = Z_0(cos\phi + jsin\phi)$

Here, the potential input is

$V(t) = V_0 e^{j(\omega t)}$

Output current is

$I(t) = I_0 e^{j(\omega t-\phi)}$

The impedance measured can then be used to propose an electrical equivalent circuit having similar spectrums as the system under test. The EIS data can be plotted as a Nyquist plot (Z_{real} vs. $Z_{imaginary}$), Bode plot (Modulus of impedance plotted versus frequency in logarithmic scale), and phase angle plot (phase angle versus frequency in logarithmic scale) (Mars G. Fontana 1987; Kelly et al. 2002; Ramanathan Srinivasan 2021). The Nyquist, Bode, and phase angle plots are illustrated in Figure 4.8.

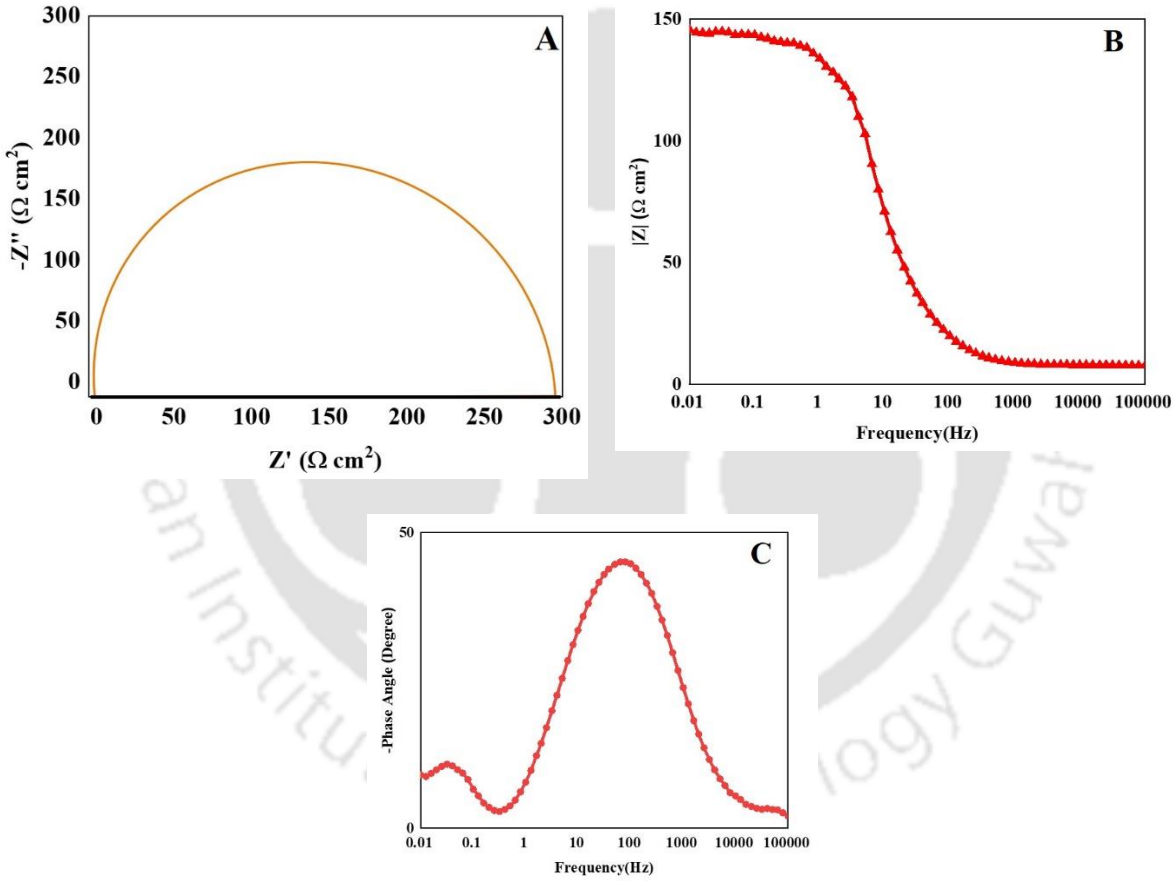

Figure 4.8 Typical EIS plot for A) Nyquist B) Bode and C) Phase angle

4.2. Other Methods

4.2.1. Weight Loss Measurements

One of the main approaches to investigate corrosion behavior is gravimetric analysis, also termed the immersion test or weight loss method. This is one of the most common methods for the quantification of corrosion rate due to its simple protocol and does not require the involvement of measurement of voltage or current. Both academic and industrial researchers use this approach widely for quantitative corrosion determination. Hence, a large number of standard procedures have already been reported.

The corrosion rate of a metal using an immersion test is quantified by measuring the mass loss of the specimen to be studied by obtaining the change in weight measured before and after exposing the specimen to the corrosive environment. Academia and industries broadly use the standard corrosion study guidelines, for instance, ASTM, G31 (Standard Guide for Laboratory Immersion Corrosion Testing of Metals) (2012), NACE TM0169/G31-12a (Zaludin et al. 2019). They provide the protocol for quantification of the corrosion rate using an immersion test.

The following mathematical equation is followed for the calculation of corrosion rate via weight loss studies (Elgaddafi et al. 2015),

$$CR = \frac{8.75\times10^{4}(W_o - W_f)}{A\times t}$$

Where,

CR: Corrosion rate (mm/year)

W_o: Original weight (g)

W_f: Final weight (g)

A: Exposed surface area (mm^2), t: Immersion time (h)

4.2.2. Polishing of Metals using CMP (Chemical Mechanical Planarization) Process

Chemical mechanical planarization (CMP) is the process of creating a highly planar surface in metals, semiconductors, dielectrics, polymers, and composites. CMP is a highly sophisticated and developed process that includes both chemical and physical action to remove materials and achieve an extremely smooth and planar surface. The process involves formulating a slurry that consists of oxidizers, complexing agents, surfactants for chemical action, and abrasives for physical action. The most important components of a CMP process are the specimen to be planarized along with the polishing pad and slurry. The planarized surface via the CMP process is obtained using a CMP machine. To get a more vivid idea of the whole process, we need to discuss the equipment first. The salient features of a CMP machine are a wafer carrier where the wafer (metal sample/specimen) is fixed; a polishing pad on which the wafer is polished; the slurry used for polishing is supplied continuously during the polish such that there is a flow of slurry through the wafer and the polishing pad; an appropriate downforce is applied upon the metal through a membrane-like object that is assembled in the wafer carrier. Also, the polishing pad is attached to the platen. The force applied on the wafer for polishing is mostly between 1 and 10 psi, and the table diameter ranges from 20 to 26 inches. The wafer is polished by chemical action due to oxidizers and other additives and physical action due to the abrasives and polishing pad. The schematic diagram of a typical CMP polisher is shown in Figure 4.9. From the above explanation, it is clear that the wafer moves in a relative motion with polishing pad, and the material is removed (Steigerwald et al. 1997; Alkalah 2004; Krishnan et al. 2010). In the CMP polisher used in the present study the platen moves in orbital direction with respect to the wafer. The rate of removal of material is regulated by the Preston's equation

$$Removal\ Rate\ = K_p \times P \times V$$

Where, K_p is a constant known as the Preston's coefficient, P is the pressure applied on the wafer surface, and V is the relative velocity between the wafer carrier and the polishing pad.

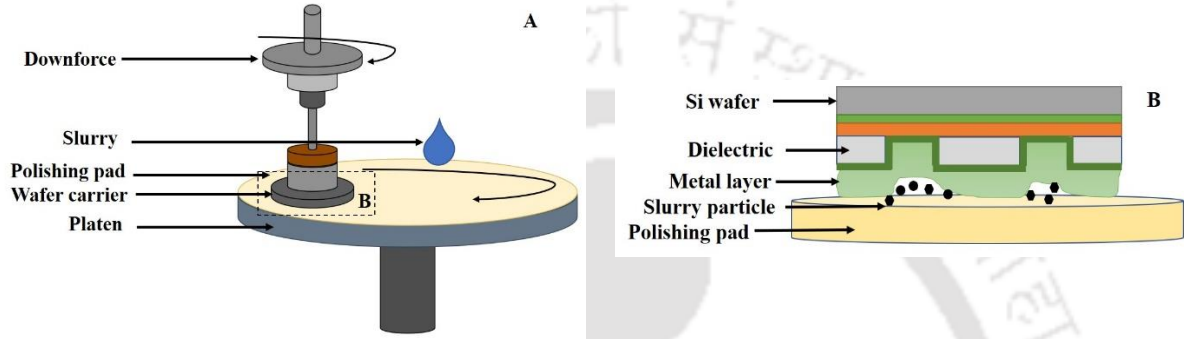

Figure 4.9 Schematic diagram of A) typical CMP machine function B) polishing process

4.3. Characterization Studies

4.3.1. Field Emission Scanning Electron Microscopy (FESEM)

Microscopic techniques analyze the surface and provide the morphological and compositional characteristics. Field emission scanning electron microscopy is an advanced instrument that is used to study the morphology of materials at a molecular level. Erwin Muller invented FESEM in 1936. Along with the surface morphology, it is also applicable for the analysis of surface topography, measurement of film thickness, and imaging of non-conductive as well as surface sensitive materials. This method can provide high-resolution images for very small structures, even in the nanometer range. FESEM uses a field emission gun as the electron source in a high vacuum system. Fine and focused electron beam produced from the field electron gun scans over the

surface area of the specimen at an accelerating voltage of 1-30 kV. A cleaner image with less electrostatic distortions is obtained using FESEM with a spatial resolution of less than 2 nm. With all the specifications, FESEM can achieve small probe diameters and high probe currents at low beam energies, which results in higher resolution. The low kinetic energy electron probes in FESEM provide a reduced penetration and, hence, give information closer to the immediate material surface. High-quality, low-voltage images are obtained with negligible electrical charging of samples.

4.3.2. X-Ray Photoelectron Spectroscopy Analysis (XPS)

X-ray photoelectron spectroscopy is also known as electron spectroscopy for chemical analysis (ESCA). It is a surface analysis technique that measures the chemical composition of a material. As the name suggests, electron spectroscopy utilizes the characteristic electrons that are emitted from any solid surface for elemental analysis. The characteristic photoelectrons demonstrate characteristic energy levels exposing the attribute of the chemical elements of the specimen examined. The XPS is a method that includes chemical analysis of the surface since the photoelectrons are capable of only escaping from the atomic layer of the solid surface up to a depth of only a few nanometers (< 10nm) due to their relatively low energy ($\leq 200\ eV$). The binding energy spectra of the X-ray photoelectrons help in identifying the chemical element. The binding energy possessed by atomic electrons has characteristic values that help to recognize the elements, when an incident X-ray photon with a corresponding kinetic energy knocks out the inner shell electron of any element. If the kinetic energy is known, then the binding energy of the photoelectron can be calculated as

$$e_\beta = h\nu - e_\kappa - \theta$$

Where,

e_β is the binding energy of the atom's photoelectron, e_κ is the kinetic energy, θ, the parameter that represents the energy that is required for an electron to jump from the specimen surface

h, Planck's constant and ν is the frequency. A typical XPS spectrum is plotted as binding energy vs. intensity.

4.3.3. Contact Angle Study

The contact angle is formed at the intersection of a solid-liquid interface or a gas-liquid interface. It is calculated by measuring the angle formed when a tangent is drawn from the point of contact along the droplet profile in the solid-liquid interface. The contact angle is represented in Figure 4.10 illustrating the contact angle of a liquid droplet over a solid surface. The figure shows that the surface wetting is more at a contact angle of less than 90° (Figure 4.10) (Behera et al. 2019; Singh et al. 2020). With an increase in contact angle, the surface wetting also decreases (Figure 4.10B, Figure 4.10C).

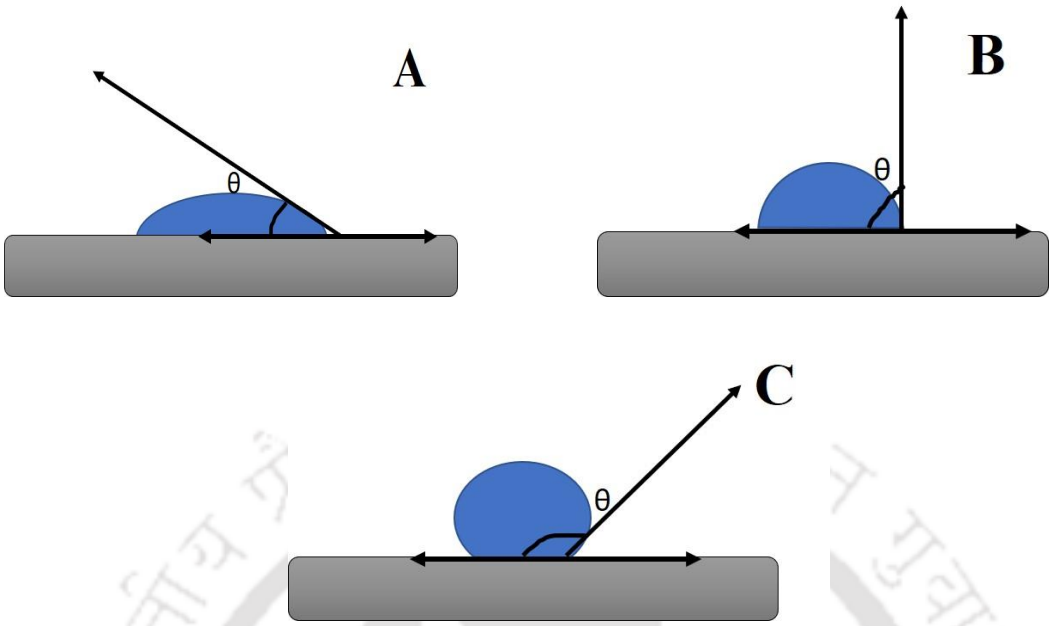

Figure 4.10 Schematic diagram of contact angle of a liquid on a solid surface A) contact angle < 90°, B) Contact angle = 90°, C) Contact angle > 90°

Till now, the thesis topic has been introduced, and the aim and objectives of the research work are discussed based on the comprehensive literature survey performed. After which, the materials used for experiments and the experimental procedures are explained. The theoretical background of the experimental procedures is also discussed in detail. Next, we will discuss the results obtained in the next results and discussions section. Among which, in Chapters 5 and 6, we will discuss the Mo dissolution behavior in the presence of H_2O_2 and $KMnO_4$, respectively. This will be followed by Chapter 7, which is about the mechanistic analysis of corrosion behavior of carbon steel in CO_2-H_2S-HAc media.

CHAPTER 5

Chapter V: Investigation on Anodic Dissolution of Mo in Alkaline Solutions Containing Oxidizer (H_2O_2) via Electrochemical Impedance Spectroscopy: A Mechanistic Analysis

5.1. Motivation

Molybdenum (Mo) finds its application in various industries, including metal oxide semiconductor field effect (MOSFET) transistors (Yang et al. 2018). Because of its passivation properties, Mo is emerging as an interconnect metal and barrier layer in semiconductor industries, replacing copper (Cu) and tungsten (W) (Adelmann et al. 2014; Ryu et al. 2021). The Mo is polished using the CMP process in semiconductor industries using H_2O_2 as an oxidizer. However, the electrochemical reactions between Mo and H_2O_2 have not been investigated yet. Thus, this study is devoted to understanding the dissolution behaviour of Mo in H_2O_2 solution using electrochemical techniques.

Results and Discussions

5.2.1. Etch Rate (ER) Measurements

The ER of Mo in various concentrations of H_2O_2 solution was measured at pH 10. The results obtained are shown in Figure 5.1. The formula for calculating the etch rate is provided in the supplementary file (Equation S1). As expected, the ER observed is very low when the solution does not contain H_2O_2. Besides, the ER increases with an increase in H_2O_2 concentration. Similarly, in CMP application, the increase in Mo polish rate with H_2O_2 concentrations is reported in the literature (Qu et al. 2017; Nam et al. 2024). Electrochemical experiments were further conducted to understand the underlying reaction mechanism and its kinetics.

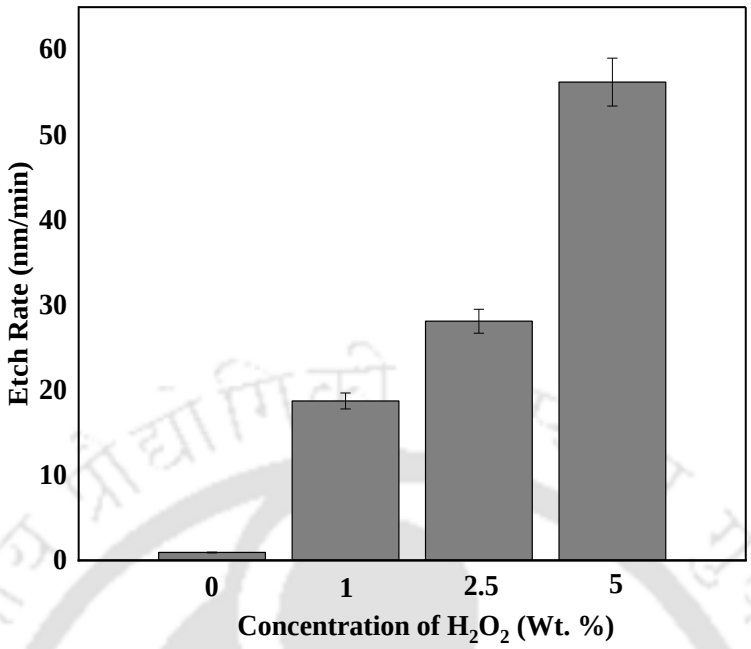

Figure 5.1 Etch Rate plot for Mo in various concentrations of H_2O_2 at pH 10

5.2.2. Open Circuit Potential Measurements

The open circuit potential (OCP) of Mo in H_2O_2 solutions (0-5 wt. %) was measured, and the results are presented in Figure 5.2. It is evident from the data obtained that the OCP value increases with increasing H_2O_2 concentration. The OCP value is -0.004 V in the absence of H_2O_2. Further, the OCP values are 0.14 V, 0.25 V, and 0.29 V for 1 wt. %, 2.5 wt. %, and 5 wt. % H_2O_2 solutions, respectively. The increase in OCP value with H_2O_2 concentration from 1 wt. % to 10 wt. % is also reported for Cu (Du et al. 2004). This is mainly due to the formation of oxide species on the metal surface. Further, in all the cases, the system attains the steady state OCP value in 600 s. Thus, the equilibration time of 600 s was provided for electrochemical experiments. Dependence of OCP value on oxidizer concentration is also reported by Yang et al. (Yang et al. 2018) at alkaline conditions for Mo dissolution in H_2O_2 solution in presence of glycine as inhibitor. In the absence of glycine, the OCP value increased with the increase in H_2O_2 concentration.

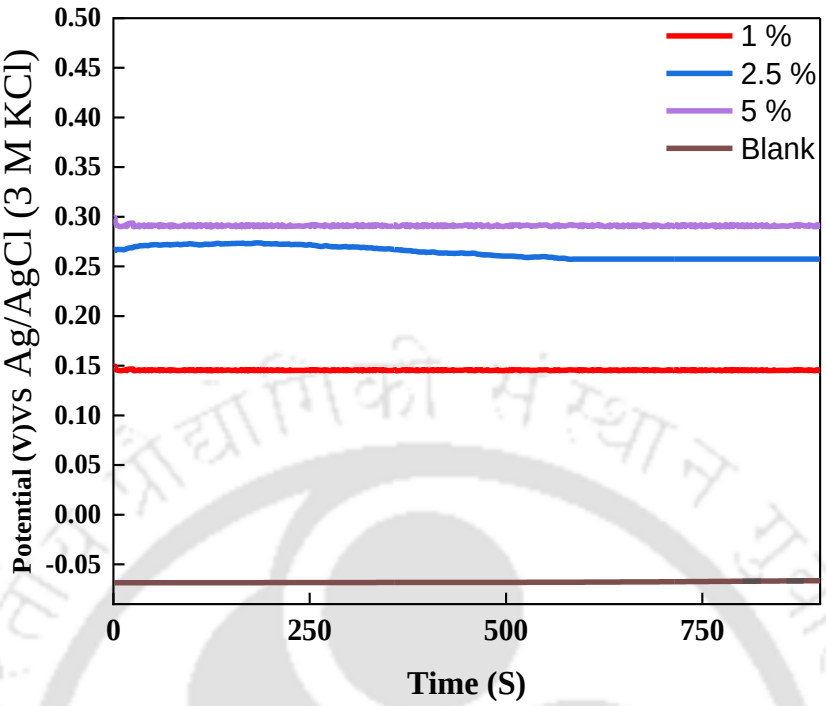

Figure 5.2 Open circuit potential plot for Mo in various concentrations of H_2O_2 solution at pH 10

5.2.3. Potentiodynamic Polarization Measurements

The anodic polarization measurement of Mo in solutions containing 0 wt. %, 1 wt. %, 2.5 wt. % and 5 wt. % H_2O_2 were performed at pH 10, and the results obtained are shown in Figure 5.3. In the absence of H_2O_2, the observed current density in the measured potential range is insignificant as compared to the values obtained for the solutions containing H_2O_2. In the presence of H_2O_2, the anodic polarization curves exhibit a similar pattern in all the cases, i.e., the current density increases with an increase in overpotential (from 0 to +0.5 V vs. OCP), indicating the active dissolution of Mo in H_2O_2 solutions. The passivation was not observed in the potential regime being investigated, as the constant current regime is not evident in these curves. Besides, the current density at any given overpotential increases with an increase in the H_2O_2 concentration.

This indicates that the dissolution rate increases with an increase in H_2O_2 concentrations, as observed in static etch rate experiments. Similar behavior of increased active dissolution at higher H_2O_2 concentration is reported for Mo at pH 10. The anodic current density as well as the corrosion current increased when the H_2O_2 concentration was increased from 1 wt. % to 10 wt. % (Qu et al. 2017).

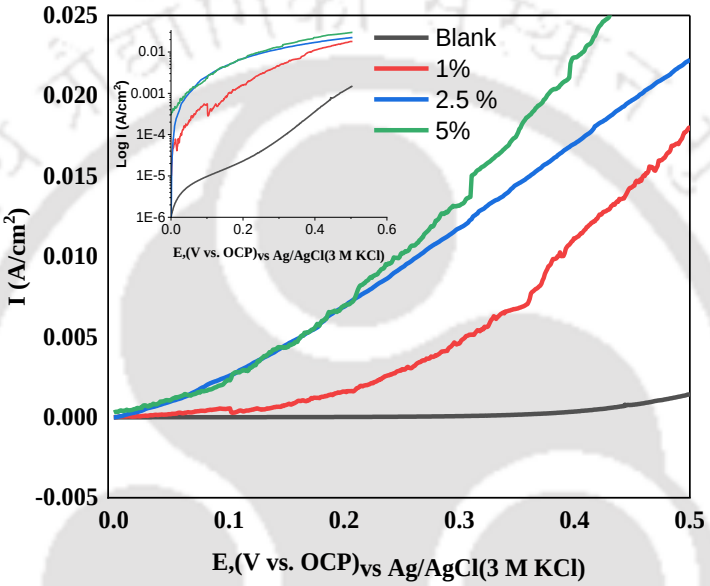

Figure 5.3 Anodic potentiodynamic polarization (*V* vs. OCP) plot for Mo in solutions containing various concentrations of H_2O_2 at pH 10

5.2.4. Pourbaix Plot

The stability of metal as a function of pH and potential range is expressed using the Eh-pH (Pourbaix) diagram. The Eh-pH plot constructed using Medusa® software is shown in Figure 5.4. It explains the electrochemical stability of Mo within the potential range of -2.5 V to +2.5 V and for the pH 0 to 14. From the Eh-pH plot, Mo is observed to dissolve in the form of $HMoO_4^-$ and MoO_4^{2-} ions or get passivated in the form of MoO_3 and MoO_4, depending upon the pH value and equilibrium potential. Ryu et al. (Ryu et al. 2021) also reported a Pourbaix diagram of the Mo-

H_2O system at 25 °C. They observed similar thermodynamic equilibrium states of Mo species within the entire pH range (Ryu et al. 2021). In the present study, the equilibrium potential exhibited by Mo in various concentrations of H_2O_2 solutions is in the range of 0.1 V to 0.3 V at pH 10. The equilibrium potentials are marked as blue, red, and green dots for 0.1V, 0.2 V and 0.3 V, respectively. Thus, Mo dissolves as MoO_4^{2-} (the oxidation state changes from 0 to +6) in the solutions containing H_2O_2. The polarization curves exhibit similar behavior, and equilibrium potential values fall in the same regime at pH 10. Besides, the CMP experiments suggested that the optimum concentration is 2.5 wt. % H_2O_2 (Qu et al. 2017; Ryu et al. 2021). Thus, the electrochemical experiments are restricted to 2.5 wt. % H_2O_2 to explicate the mechanism of Mo dissolution in H_2O_2 solutions.

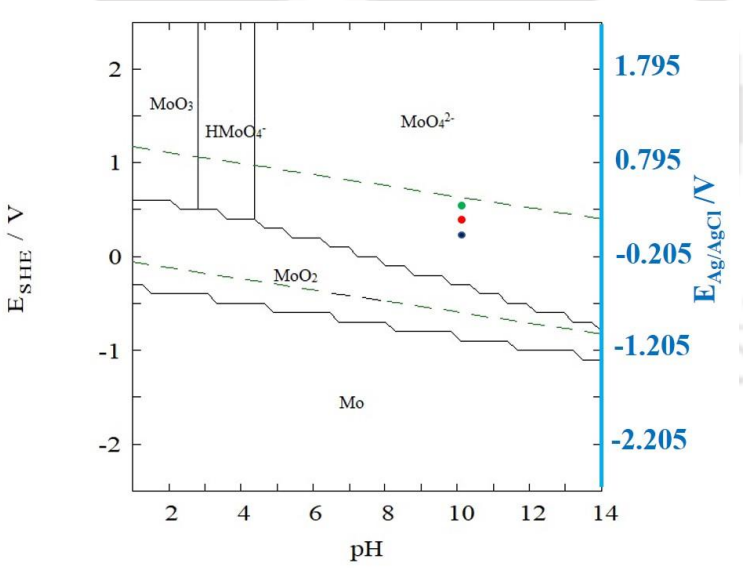

Figure 5.4 Pourbaix Plot for Mo-H_2O system at 25 °C with Mo ion concentration as 10^{-6} M

5.2.5 Cyclic Voltammetry Measurements

The cyclic voltammograms (CV) curves of Mo in 0 and 2.5 wt.% H_2O_2 solutions at 10 pH were measured as shown in Figure 5.5. Two oxidation peaks, O_1 and O_2, appeared in the forward scan at potentials of 0.05 V and 0.24 V, respectively. The first peak is likely due to the oxidation of Mo to Mo^{4+} (MoO_2), and the second peak corresponds to the further oxidation of Mo^{4+} to Mo^{6+} (MoO_4^{2-}). The corresponding reduction peaks R_1 and R_2 were observed at 0.21 V and -0.05 V, respectively. However, the reduction peak R_2 is not clearly evident in the CV and thus, a more sensitive technique, square wave voltammetry (SQV), was conducted to capture the reduction peaks, as shown in Figure 5.6. The cyclic voltammogram obtained for the blank solution (solution without H_2O_2), presented in Figure 5.5 for comparison, shows no peaks. This is likely due to the sluggish kinetics of Mo dissolution as evident from the polarization data.

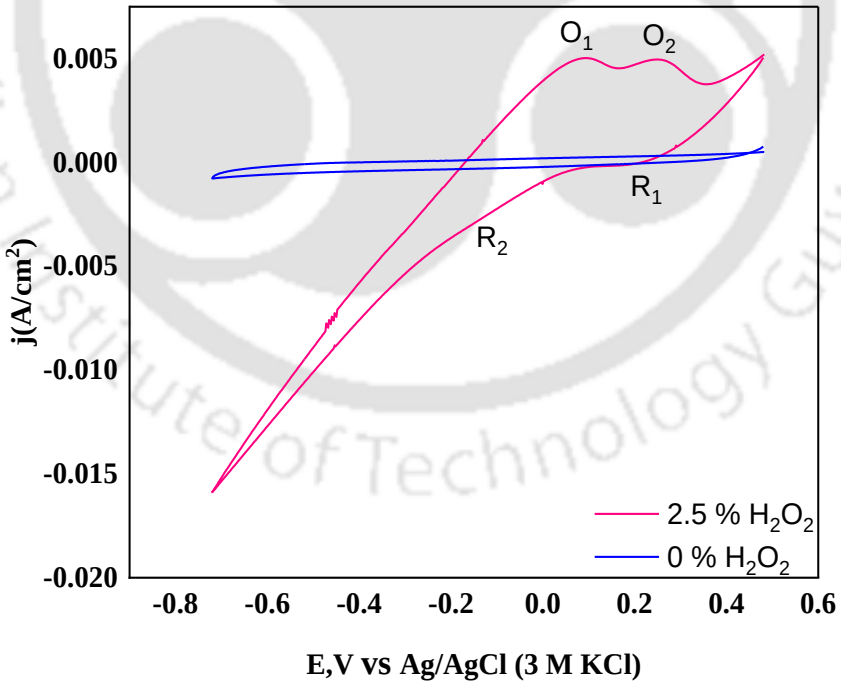

Figure 5.5 Cyclic voltammogram of Mo in 0 and 2.5 wt. % H_2O_2 solution at pH 10

5.2.6 Square Wave Voltammetry

To further analyze the reduction peaks, square-wave voltammetry was performed (Figure 5.6) (Mariola Brycht, Sławomira Skrzypek, Kinga Kaczmarska, Barbara Burnat 1, Andrzej Leniart 1 2015). To perform the experiment the system was scanned from -0.5 V to 0.5 V at a frequency of 25 Hz. The reduction peak potential R_1 is observed at 0.98 V and R_2 at -0.05 V. The reduction peaks correspond with the reduction peaks R_1 and R_2 observed in the CV measurement (Figure 5.5).

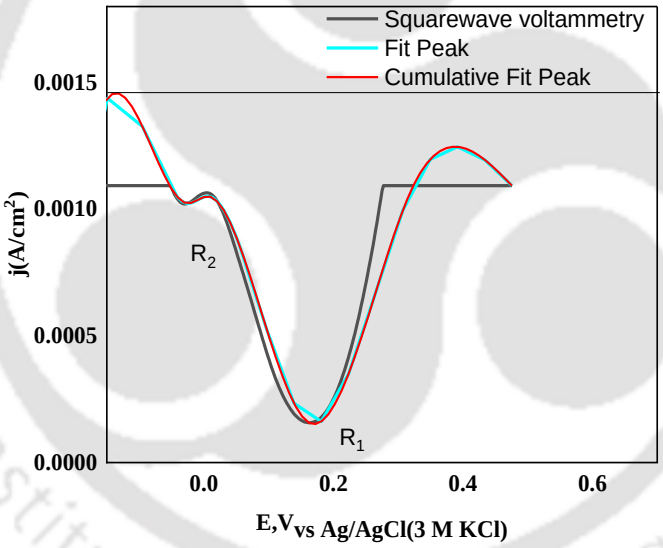

Figure 5.6 Square-wave voltammogram of Mo in 2.5 wt. % H_2O_2 solution at pH 10

5.2.7. Characterization Studies

5.2.7.1. FESEM Analysis

The FESEM images of the Mo surfaces were captured to understand the type of corrosion, as shown in Figure 5.7. Before exposure to the H_2O_2 solution, the blank metal surface shows (Figure 5.7A) a plain surface without any cracks or corrosion marks. The Mo surface exposed to 2.5 wt.

% H_2O_2 solution showed uniform corrosion with some cracks (Figure 5.7 B) (Gao et al. 2024). The morphology of the Mo surface exposed to the blank solution does not show any significant corrosion marks. The FESEM images of the corrosion product obtained are shown in Figure 5.8. The products were composed of flake-like and clusters of smaller particle-like structures (Figure 5.8A and B). The cluster, when magnified, showed a flowery structure. A similar structure is reported in the literature, confirming MoO_3 (Maheswari and Muralidharan 2017; Reddy et al. 2019; Song et al. 2019; Varol Özkavak 2024). XPS analysis was performed to further confirm the formation of molybdenum oxides.

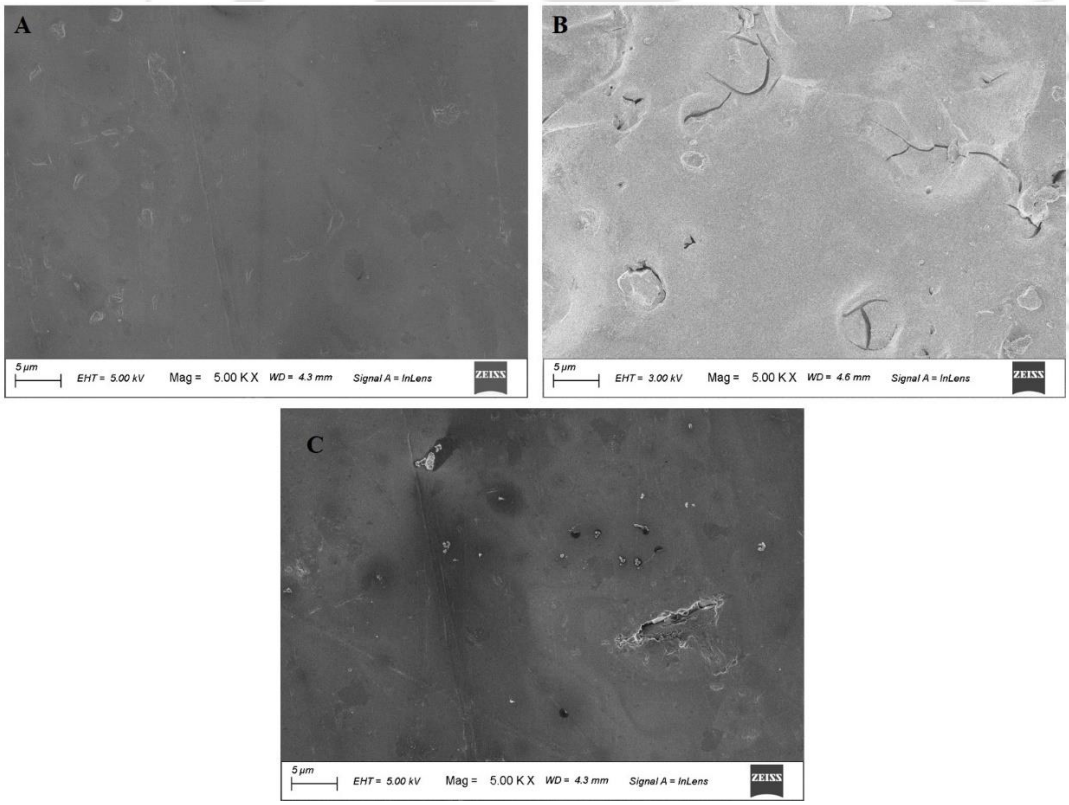

Figure 5.7 FESEM images of Mo A) Before exposing B) After exposure to 2.5 wt. % H_2O_2 C) exposing in blank solution for 2 h at pH 10

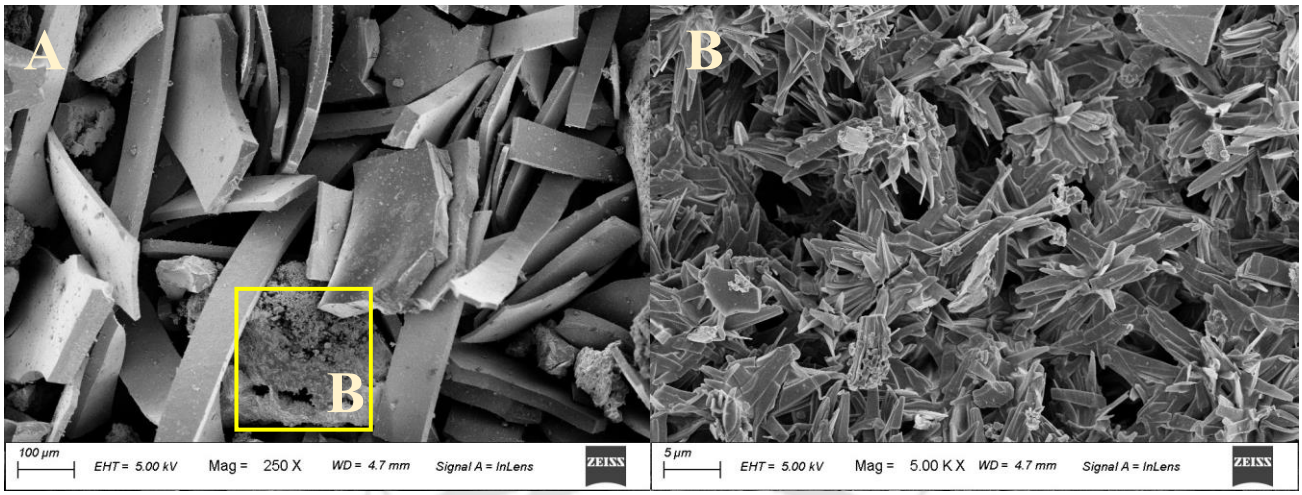

Figure 5.8 FESEM images of the corrosion product obtained by exposure of Mo in 2.5 wt. % H_2O_2 for 2 h at pH 10

5.2.7.2. XPS Analysis

To get further clarification on the oxidation state of Mo when exposed to 2.5 wt. % H_2O_2, XPS analysis was performed. Figure 5.9 shows the deconvoluted species of Mo 3d [Figure 5.9 (A)] and O1S [Figure 5.9 (B)]. The XPS survey plot is shown in Figure 5.10. The peak fitting was performed using the Gaussian model. The XPS high-resolution spectrum of the Mo 3d peak was deconvoluted into $Mo3d_{3/2}$. The deconvoluted Mo3d spectra showed $Mo^{4+}3d_{3/2}$ at 233 eV, $Mo^{6+}3d_{5/2}$ at 234 eV, and $Mo^{6+}3d_{3/2}$ at 237 eV (Xie et al. 2013; Song et al. 2019; Lin et al. 2023). The peak at 233 eV corresponds to MoO_2 (M. Ürgen,U Stolz, R Kirchheim 1990) while the peaks at 234 eV and 237 eV correspond to MoO_3 (Schroeder et al. 2004; Baltrusaitis et al. 2015). The formation of MoO_2 in the presence of H_2O_2 is due to the following reaction (Ryu et al. 2021)

$$Mo + H_2O_2 \rightarrow MoO_2 + H_2 \qquad 5.1$$

The MoO_2 is further oxidized into MoO_3 ($MoO_2 + H_2O_2 \rightarrow MoO_3 + H_2O$) and reacts with hydroxyl ion to form soluble MoO_4^{2-} ions in alkaline solution due to the following reaction (Ryu et al. 2021).

$$MoO_3 + 2OH^- \rightarrow MoO_4^{2-} + H_2O \quad 5.2$$

The O1S spectrum shows a main peak at 531.5 eV (Morgan 2021; Dey et al. 2024). After de-convolution, two peaks at 531.5 eV and 531.9 eV and a smaller peak at 533.4 eV were observed (Yu et al. 2023; Wang et al. 2024). The main peaks at 531.5 eV and 531.9 eV correspond to the lattice oxygen of Mo oxide (Choi et al. 2011; Liu et al. 2024). The peak obtained at 533.4 eV corresponds to OH^-. This is likely due to the adsorbed ions on the metal surface. A similar observation was also reported by other researchers (Yu et al. 2023) . There were no other oxides of Mo found, since the $HMoO_4^{2-}$ is soluble and could not be collected as a product. To be precise, XPS analysis reveals that the surface is occupied mainly by MoO_2 and MoO_3.

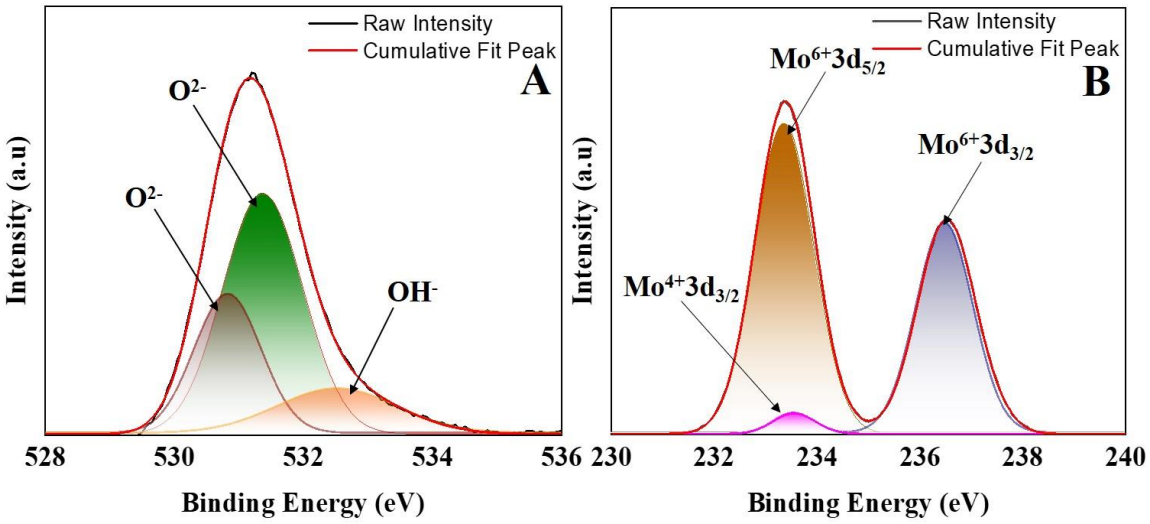

Figure 5.9 Detailed spectra of A) O1S and B) Mo3d for XPS of the corrosion product obtained by exposure of Mo in 2.5 wt. % H_2O_2 at pH 10

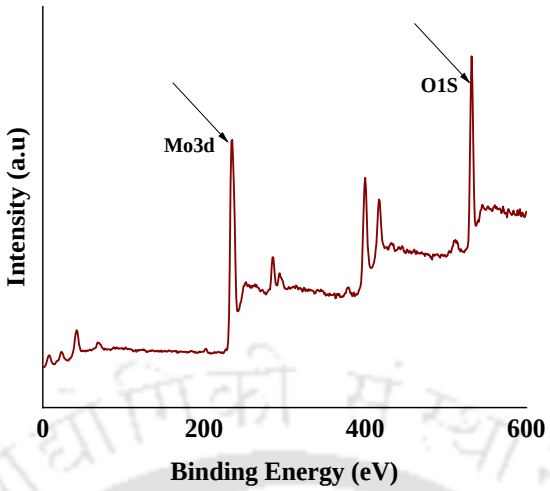

Figure 5.10 XPS survey plot of the corrosion product obtained by exposure of Mo in 2.5 wt. % H_2O_2 at pH 10

5.2.8. Electrochemical Impedance Spectroscopy (EIS) Measurements

To understand the reaction pathway and to retrieve the kinetic information of Mo dissolution in H_2O_2 solution at pH 10, EIS measurements were performed at various overpotentials (0.1 V, 0.2 V, and 0.3 V) with respect to OCP (Figure 5.12), and the results are shown in Figure 5.11. Prior to analysis, the EIS data was validated using the Kramers Kronig Technique (KKT) using Gamry software to ensure that the acquired EIS data is linear, stable, and causal (Kaisare et al. 2011; Adhikari et al. 2024). The simulated data is presented in the supplementary file (Figure 5.13-5.15). The Nyquist loop obtained showed a capacitance loop at a higher frequency range, followed by another pseudo-capacitive loop towards a lower frequency. Here, the total impedance was observed to decrease with an increase in the overpotential value (0.1 V, 0.2 V, and 0.3 V), indicating an increase in the dissolution rate of Mo as observed in polarization measurements. Further, EIS experiments at varying concentrations of H_2O_2 were also performed to ensure that the loop appearing in the low-frequency regime was not caused by the system being unstable. It shows that the impedance of the second loop changes with respect to concentration (not presented here).

To ensure that the current is stable even at lower frequencies (due to exposure of the metal in a corrosive solution for a longer time), a current vs time experiment was performed for 40 min in 2.5 wt. % H_2O_2 solution at 0.3 V (Figure 5.16), and the current was observed to be stable throughout the time.

The EIS data was further analyzed (Revilla et al. 2020; Dhongde et al. 2024) by the electrical equivalent circuit (EEC) fitting using ZSimpwin® software. The EEC circuit used for simulating impedance data is shown in Figure 5.17. It consists of solution resistance (R_s) to account for the solution resistance, the constant phase elements (Q_{CPE}), and R_{ct} to model the capacitance associated with the electrical double layer and the charge transfer resistance (the resistance at $\lim_{\omega\to\infty} Z_f$) associated with electrochemical system respectively (Kumar and Das 2024; Pan et al. 2024). If the reactions occur via multi-steps, additional loops will appear in the Nyquist plot. Thus, an additional pair of C_1 and R_1 is included in the circuit to model the faradaic reactions occurring via multi-steps, i.e., here, the dissolution reaction takes place via the formation of adsorbed intermediates. The simulated data obtained from EEC fitting is represented as a solid black line in Figure 5.11. The proposed circuit is selected among the ones with the least error (< 5%). Since a depressed semicircle is observed in the EIS, the Q_{CPE} is calculated for the real system using the following formula (Bai et al. 2015; Dhongde et al. 2023)

$$Q_{CPE} = \frac{(jw)^{-n}}{Y_0} \qquad 5.3$$

Here, Y_0 and n are the parameters of CPE, and *w* is the angular frequency. At n=1, CPE designates an ideal capacitor. In our case, the value ranges between 0.8 and 0.9, which is attributed to the roughness of the metal surface (Bai et al. 2015; Baranwal and Prasanna Venkatesh 2017; Kumar and Das 2023). It is well evident from Table 5.1. that both R_{ct} and R are decreasing with

overpotential, indicating the active dissolution of Mo within the discussed potential range. It is also consistent with polarization results. Similarly, the Y_0 and C_1 values increase with overpotential (Baranwal and Rajaraman 2019; Talukdar et al. 2023; Devi et al. 2024).

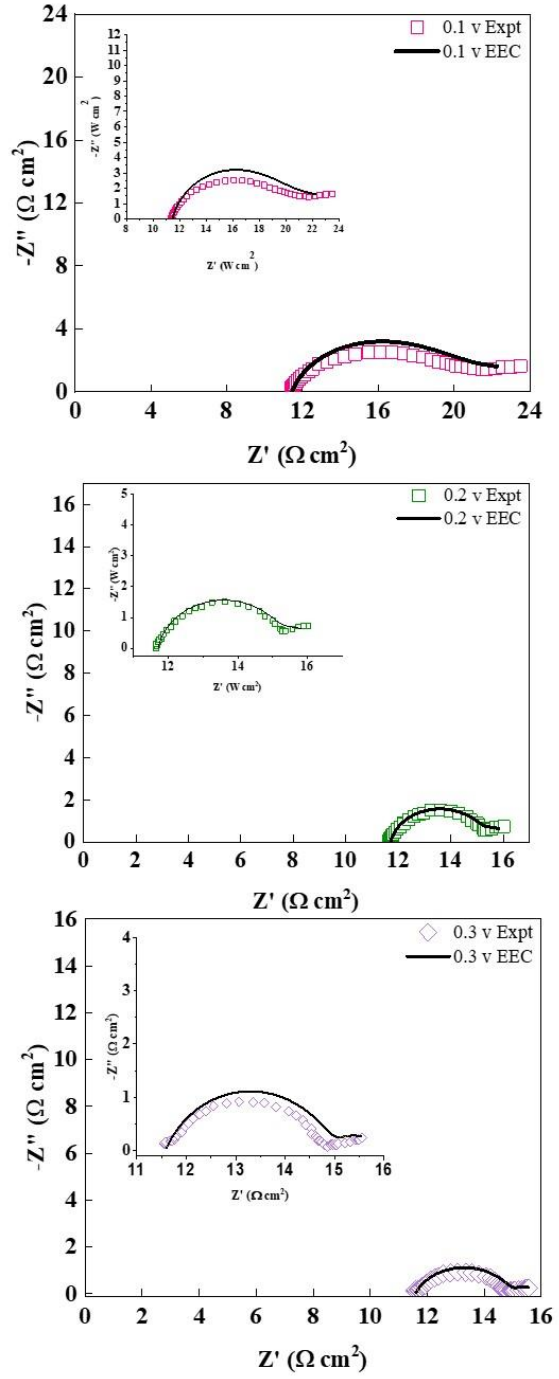

Figure 5.11 Experimental and EEC fitting electrochemical impedance spectroscopy data of Mo in 2.5 wt. % H_2O_2 solution at pH 10 at 0.1, 0.2 and 0.3 V overpotentials. The experimental data is shown as dotted lines and fitted data is illustrated as solid line

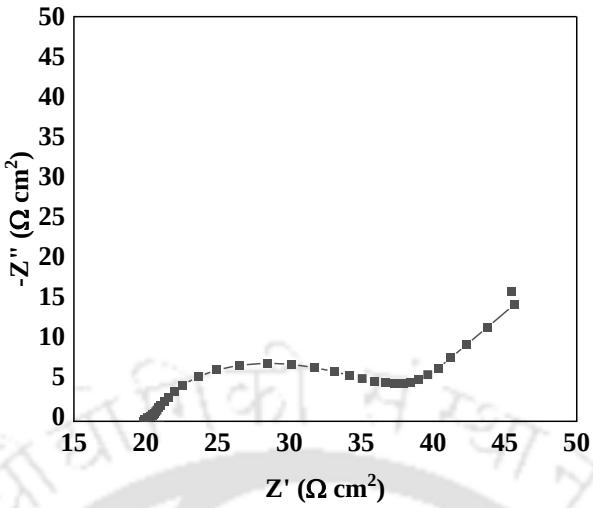

Figure 5.12 Electrochemical impedance spectroscopy of Mo in 2.5 wt. % H_2O_2 at OCP

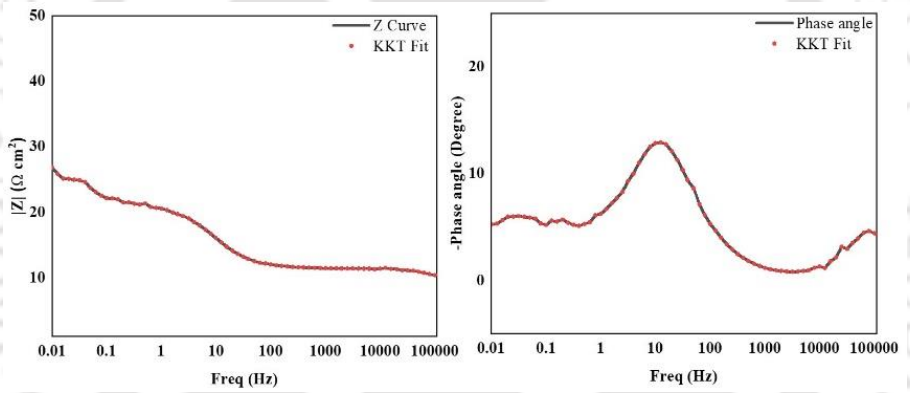

Figure 5.13 Experimental and KKT fitting data of Mo in 2.5 wt. % H_2O_2 solution at pH 10 at 0.1 V w.r.t. OCP. The experimental data is shown solid lines and fitted data is illustrated as dotted line

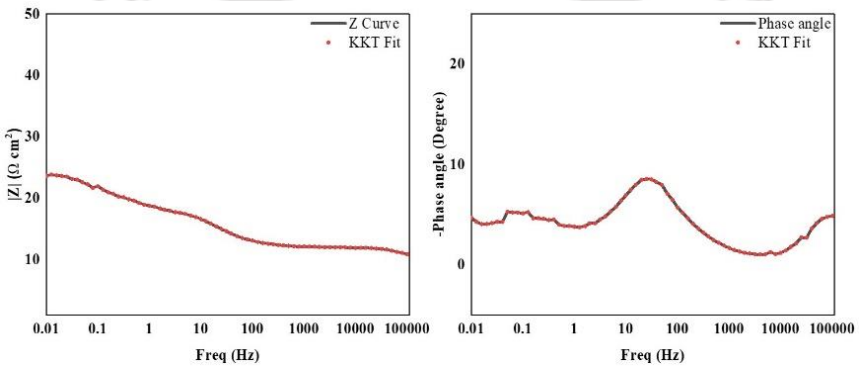

Figure 5.14 Experimental and KKT fitting data of Mo in 2.5 wt. % H_2O_2 solution at pH 10 at 0.2 V w.r.t. OCP. The experimental data is shown solid lines and fitted data is illustrated as dotted line

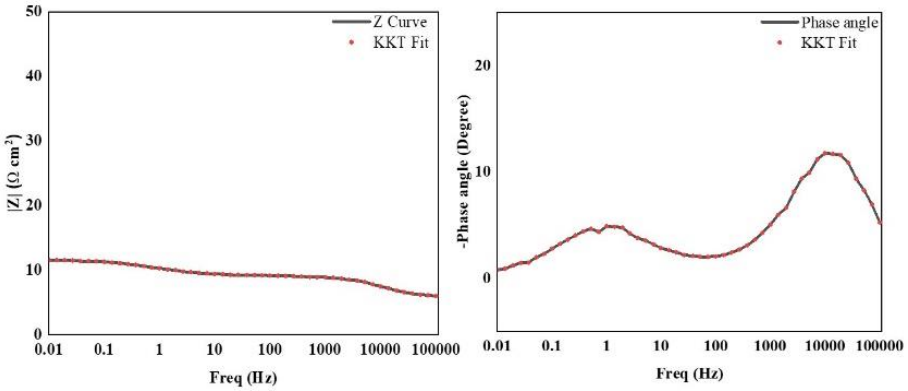

Figure 5.15 Experimental and KKT fitting data of Mo in 2.5 wt. % H_2O_2 solution at pH 10 at 0.3 V w.r.t. OCP. The experimental data is shown solid lines and fitted data is illustrated as dotted line

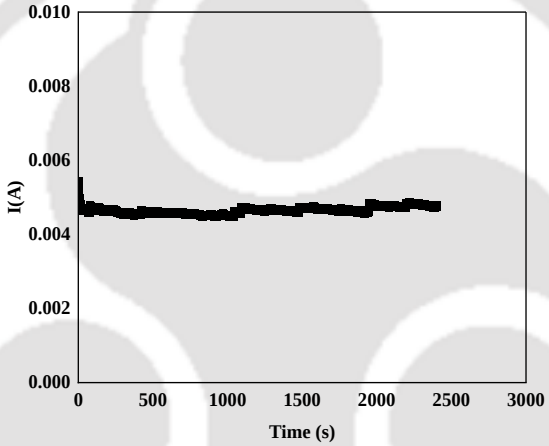

Figure 5.16 Current vs time plot to monitor current stability with time in 2.5 wt. % H_2O_2 solution at 0.3 V

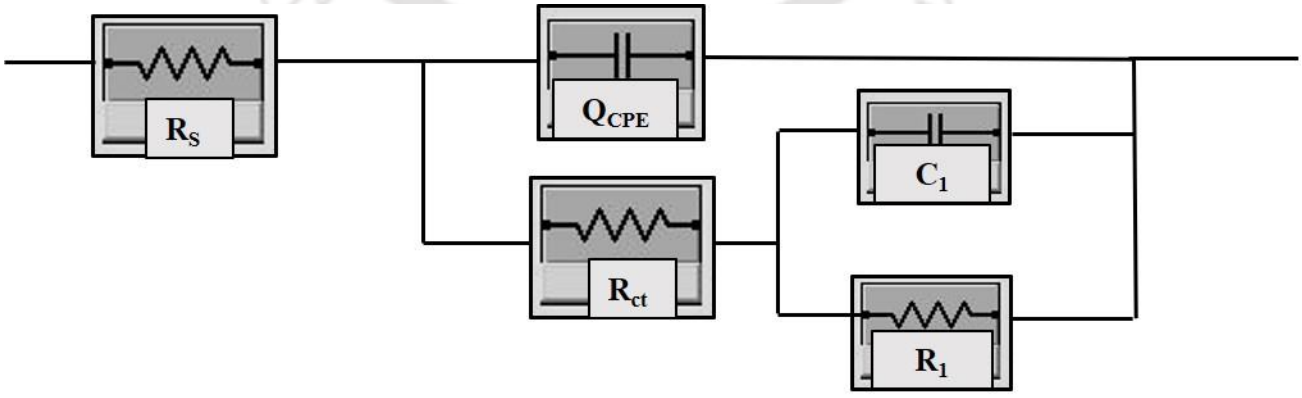

Figure 5.17 Electrochemical equivalent circuit obtained from EIS data for Mo in 2.5 wt. % H_2O_2 solution at pH 10

Table 5.1. EEC Fitting parameters of EIS data of Mo in 2.5 wt. % H_2O_2 solution at pH 10

Overpotential (V)	R_s (Ωcm^2)	Q_{CPE}		R_{ct} (Ωcm^2)	C_1	R_1 (Ωcm^2)
		$Y_o \times 10^{-4}$ ($\Omega^{-1} cm^{-2} S^n$)	**n**		**$Y_o \times 10^{-1}$ ($\Omega^{-1} cm^{-2} S^n$)**	
0.1	11.78±0.11	0.9±0.01	0.9	9±0.18	0.06±0.00	1.5±0.00
0.2	11.59±0.14	1.0±0.01	0.8	3.7±0.07	2.7±0.02	1.0±0.01
0.3	11.44±0.12	1.8±0.03	0.8	3.4±0.07	2.9±0.01	0.9±0.00

5.2.9. Reaction Mechanism Analysis

EEC fitting has limitations in providing a detailed analysis of the EIS data (Amrutha et al. 2018). Thus, RMA was performed to provide more insight into the reaction mechanism of Mo in alkaline solution containing an oxidizer. The RMA was performed by considering the following assumptions (Jeevan Maddala, Krishnaraj Sambath, Vinod Kumar):

i. The Langmuir isotherm model was considered for the charged adsorbed species. This restricts the surface coverage to unity.

ii. The system perturbation was considered linear, neglecting the higher-order terms.

iii. The kinetic parameters of the reaction depend exponentially on voltage ($k_i = k_{i0} e^{b_i V}$, where, $b_i = \pm \frac{\alpha n F}{RT}$).

iv. The forward reaction was considered to have a positive component and vis-à-vis.

The pre-exponential terms k_{i0} and b_i are independent of the DC potential applied. α is the transfer coefficient, and its value ranges between 0 to 1. F is the Faraday constant (96500 C mol^{-1}), n corresponds to the number of electrons transferred, and R is the universal gas constant and temperature, T (Baranwal and Prasanna Venkatesh 2017; Hazarika et al. 2023a).

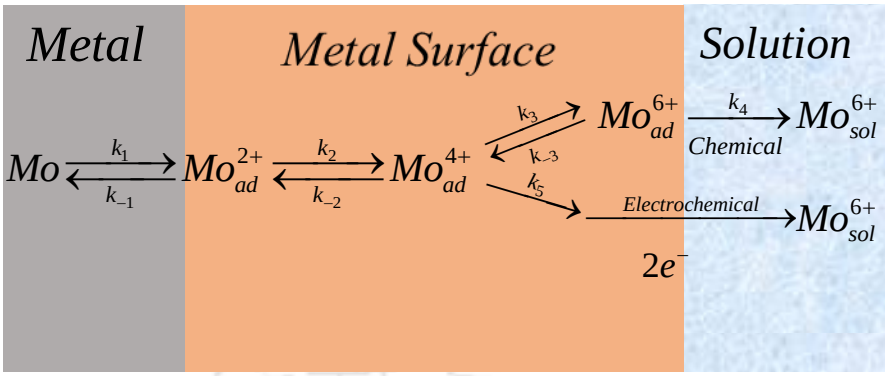

Figure 5.18 Proposed dissolution mechanism of Mo in H_2O_2

Pourbaix diagram reveals that the possible oxidation state of the dissolved species is + 6, and CV shows two oxidative peaks (Mo – Mo^{4+} - Mo^{6+}). As 4 electrons are not more likely to transfer in a single step, it is assumed that the conversion of Mo to Mo4+ occurs via two consecutive steps, i.e., Mo to Mo^{2+} and Mo^{2+} to Mo^{4+}. Based on this, the mechanism shown in Figure 5.18 is suggested. Three intermediate absorbed species are considered in the above mechanism, such as Mo^{2+}, Mo^{4+}, and Mo^{6+}, with +2, +4, and +6 oxidation states, respectively. Further, the reaction mechanism also considers that the dissolution of Mo in the H_2O_2 solution occurs via both chemical (*k4*) and electrochemical (*k5*) steps. It is to be noted that the presence of adsorbed species on the metal surface will not always generate an inductance loop in the Nyquist plot, as observed in the results and also reported in the literature (Jeevan Maddala, Krishnaraj Sambath, Vinod Kumar; Paul and Srinivasan 2020). A similar approach was employed in previous studies reported (Amrutha et al. 2018; Baranwal and Rajaraman 2019; Paul and Srinivasan 2020; Talukdar et al. 2022). Notably the value of *k4* (kinetic rate constant associated with chemical step) is independent of overpotential.

The development of the impedance equation for the suggested mechanism started with applying unsteady state mass balance over the adsorbed species, which leads to:

$$\tau \frac{d\theta_1}{dt} = k_1(1-\theta_1-\theta_2-\theta_3) - k_{-1}\theta_1 - k_2\theta_1 + k_{-2}\theta_2 \quad 5.4$$

$$\tau \frac{d\theta_2}{dt} = k_2\theta_1 - k_3\theta_2 - k_{-2}\theta_2 + k_{-3}\theta_3 - k_5\theta_2 \quad 5.5$$

$$\tau \frac{d\theta_3}{dt} = k_3\theta_2 - k_{-3}\theta_3 - k_4\theta_3 \quad 5.6$$

Where τ is the total number of available active sites per unit area, θ_1, θ_2, θ_3 are the surface coverage of the adsorbed species Mo_{ad}^{2+}, Mo_{ad}^{4+}, and Mo_{ad}^{6+}, respectively.

Under steady-state conditions, the left-hand side of the equations will be set to 0. After solving the equations, the expressions for θ_{1ss}, θ_{2ss}, and θ_{3ss} will be obtained (Paul and Srinivasan 2020).

The unsteady steady-state current density equation is,

$$J = 2F\left[k_1\left(1-\theta_1-\theta_2-\theta_3\right) - k_{-1}\theta_1 + k_2\theta_1 - k_{-2}\theta_2 + k_3\theta_2 - k_{-3}\theta_3 + k_5\theta_2\right] \quad 5.7$$

Under steady-state conditions, the above equation is expressed as

$$J_{ss} = F\left[6\left(k_4\theta_{3ss} + k_5\theta_{2ss}\right)\right] \quad 5.8$$

Differentiating J over a voltage (V) gives the faradaic impedance,

$$\frac{dJ}{dV} = \left(Z_{F,m/s}\right)^{-1} = 2F\left[\begin{array}{l} \frac{dk_1}{dV}(1-\theta_{1ss}-\theta_{2ss}-\theta_{3ss}) + k_1\left(-\frac{d\theta_1}{dV}-\frac{d\theta_2}{dV}-\frac{d\theta_3}{dV}\right) - \frac{dk_{-1}}{dV}\theta_{1ss} - k_{-1}\frac{d\theta_1}{dV} + \frac{dk_2}{dV}\theta_{1ss} \\ +k_2\frac{d\theta_1}{dV} - \frac{dk_{-2}}{dV}\theta_{2ss} - k_{-2}\frac{d\theta_2}{dV} + \frac{dk_3}{dV}\theta_{2ss} + k_3\frac{d\theta_2}{dV} - \frac{dk_{-3}}{dV}\theta_{3ss} - k_{-3}\frac{d\theta_3}{dV} + \frac{dk_5}{dV}\theta_{2ss} + k_5\frac{d\theta_2}{dV} \end{array}\right] \quad 5.9$$

Rearranging the above equation,

$$(Z_{F,m/s})^{-1} = R_t^{-1} - 2F\left[\frac{d\theta_1}{dV}\left(k_1 + k_{-1} - k_2\right) + \frac{d\theta_2}{dV}\left(k_1 + k_{-2} - k_3 - k_5\right) + \frac{d\theta_3}{dV}\left(k_1 + k_{-3}\right)\right] \quad 5.10$$

Where R_t denotes the charge transfer resistance and is expressed as,

$$R_t^{-1} = 2F\left[k_1 b_1\left(1 - \theta_{1ss} - \theta_{2ss} - \theta_{3ss}\right) - k_{-1} b_{-1} \theta_{1ss} + k_2 b_2 \theta_{1ss} - k_{-2} b_{-2} \theta_{2ss} + k_3 b_3 \theta_{2ss} - k_{-3} b_{-3} \theta_{3ss} + k_5 b_5 \theta_{2ss}\right] \quad 5.11$$

Applying Taylor series approximation on the surface coverage under unsteady state conditions and neglecting the higher order terms, we get

$$\frac{d\theta_1}{dV} = \frac{AK\left(F_1 J_1 - GK\right) + BIF_1 J_1 - BIGK + BJ_1\left(KH - F_1 I\right)}{D_1 K\left(KH - F_1 I\right) + KE\left(AK + BI\right)} \quad 5.12$$

$$\frac{d\theta_2}{dV} = \frac{KE\left(\frac{d\theta_1}{dV}\right) - F_1 J_1 + GK}{KH - F_1 I} \quad 5.13$$

$$\frac{d\theta_3}{dV} = \frac{IKE\left(\frac{d\theta_1}{dV}\right) - IF_1 J_1 + IGK - J_1\left(KH - F_1 I\right)}{K\left(KH - F_1 I\right)} \quad 5.14$$

where,

$$A = k_1 - k_{-2} \quad 5.15$$

$$B = k_1 \quad 5.16$$

$$C = k_1 b_1 - \left(k_1 b_1 + k_2 b_2 + k_{-1} b_{-1}\right)\theta_{1ss} - \left(k_1 b_1 - k_{-2} b_{-2}\right)\theta_{2ss} - k_1 b_1 \theta_{3ss} \quad 5.17$$

$$D_1 = k_1 + k_2 + k_{-1} + j\omega\tau \quad 5.18$$

$$E = k_2 \quad 5.19$$

$$F_1 = k_{-3} \quad 5.20$$

$$G = k_2 b_2 \theta_{1ss} - \left(k_3 b_3 + k_5 b_5 + k_{-2} b_{-2}\right)\theta_{2ss} + k_{-3} b_{-3} \theta_{3ss} \quad 5.21$$

$$H = k_3 + k_5 + k_{-2} + j\omega\tau \quad 5.22$$

$$I = k_3 \quad 5.23$$

$$J_1 = \left(k_4 b_4 + k_{-3} b_{-3}\right)\theta_{3ss} - k_3 b_3 \theta_{2ss} \quad 5.24$$

$$K = k_4 + k_{-3} + j\omega\tau \quad 5.25$$

The values of $\frac{d\theta i}{dV}$ (equations 22-23) in equation 17 are obtained by applying the Taylor series approximation, with the omission of higher order terms.

The overall impedance is expressed as

$$Z_{total} = R_{sol} + \frac{1}{\left(Z_{F,m/s}\right)^{-1} + (j\omega)^{n_1} Y_0} \quad 5.26$$

Where R_{sol} is the solution resistance, the values for constant phase parameters, $Y_{0,}$ and n_i, are obtained from EEC analysis.

Finally, the best fit to experimental impedance data is obtained at the optimized RMA parameter set shown in Table 5.2. The optimization was performed by sequential quadratic programming (SQP) by using a code written in MATLAB to minimize the residue of the following equation

$$Residue = \sum [(Z_{\mathrm{Re}T})^2 + (Z_{\mathrm{Im}T})^2] \quad 5.27$$

Where,

$$Z_{\mathrm{Re}T} = Z_{\mathrm{Re}_{experimental}} - Z_{\mathrm{Re}_{simulated}} \quad 5.28$$

$$Z_{\mathrm{Im}T} = Z_{\mathrm{Im}_{experimental}} - Z_{\mathrm{Im}_{simulated}} \quad 5.29$$

The impedance data calculated from the simulation is shown in Figure 5.19 in a dotted line along with the experimental data in a solid line. Further, the steady-state current values simulated from equation 13 are compared with the anodic polarization plot for Mo dissolution in 2.5 wt. % H_2O_2 solution, as shown in Figure 5.20. The steady state current values for Mo dissolution in 1 and 5 wt. % H_2O_2 solution was also simulated using the same mechanism. It captured experimental trends qualitatively well in the concentration range being investigated (Refer to Figure 5.21). Further, it is observed that only the k_{50} value is sensitive to the H_2O_2 concentration for the entire concentration range (1-5 wt. %) while the k_{20} value is sensitive only in the concentration range of 1-2.5 wt. % (Refer Table 5.3). The values of other RMA parameters remain the same for the entire concentration range. However, there is a quantitative difference between the experimental and simulated data. The suggested mechanism captures the number and pattern of loops observed in the impedance measurement of all the experimental trends observed in both polarization and

impedance measurements. The difference is relatively high for impedance data acquired at an overpotential of 0.1 V. This is likely due to the interference of cathodic reactions as the potential is closer to the OCP value. From the RMA parameters obtained, the surface coverage of Mo^{2+}, *Mo4+, and Mo6+* is estimated for various overpotentials, which is presented in Figure 5.22 (A). The surface coverage of both adsorbed species ($Mo^{2+}$and Mo^{4+}) is very negligible (~0.01) at all the overpotential values being investigated, while the surface coverage of Mo^{6+} is increasing with overpotential (0.60 at 0.1 V to 0.97 at 0.3 V). Thus, the surface is occupied mainly by Mo^{6+} at any overpotential level. It reveals that the conversion of Mo^{4+} to Mo^{6+} is very rapid compared to that of Mo to Mo^{4+} via Mo^{2+}. Further, the surface coverage is higher (close to 1) at a higher overpotential. This is mainly ascribed to the low k_4 value, i.e., the dissolution of Mo^{6+} via chemical step is insignificant, while the k_3 value (conversion of Mo^{4+} to Mo^{6+}) is higher. To be precise, the surface coverage obtained from the RMA simulation confirms maximum coverage by the adsorbed species Mo_{ad}^{6+}, corresponding to MoO_3, as confirmed from XPS data. The total current estimated is resolved into two components: (i) due to the chemical step (k_4) and (ii) due to the electrochemical step (k_5) using equations 10 and 11; the same is plotted in Figure 5.23 (B). It is evident that the contribution to the total dissolution by chemical step (k_4) is significantly lower and is almost constant concerning the overpotential values. On the other hand, the contribution by the electrochemical step (k_5) is significantly higher and is also increasing with overpotential. The schematic of the dissolution mechanism is shown in Figures 5.24 and 5.25. Thus, the overall dissolution in the form of MoO_4^{2-} occurs mainly via the electrochemical step, whereas the low rate of the chemical step (k_4) is responsible for the oxides (MoO_3) on the metal surface. These findings are also consistent with the Pourbaix diagram and XPS results.

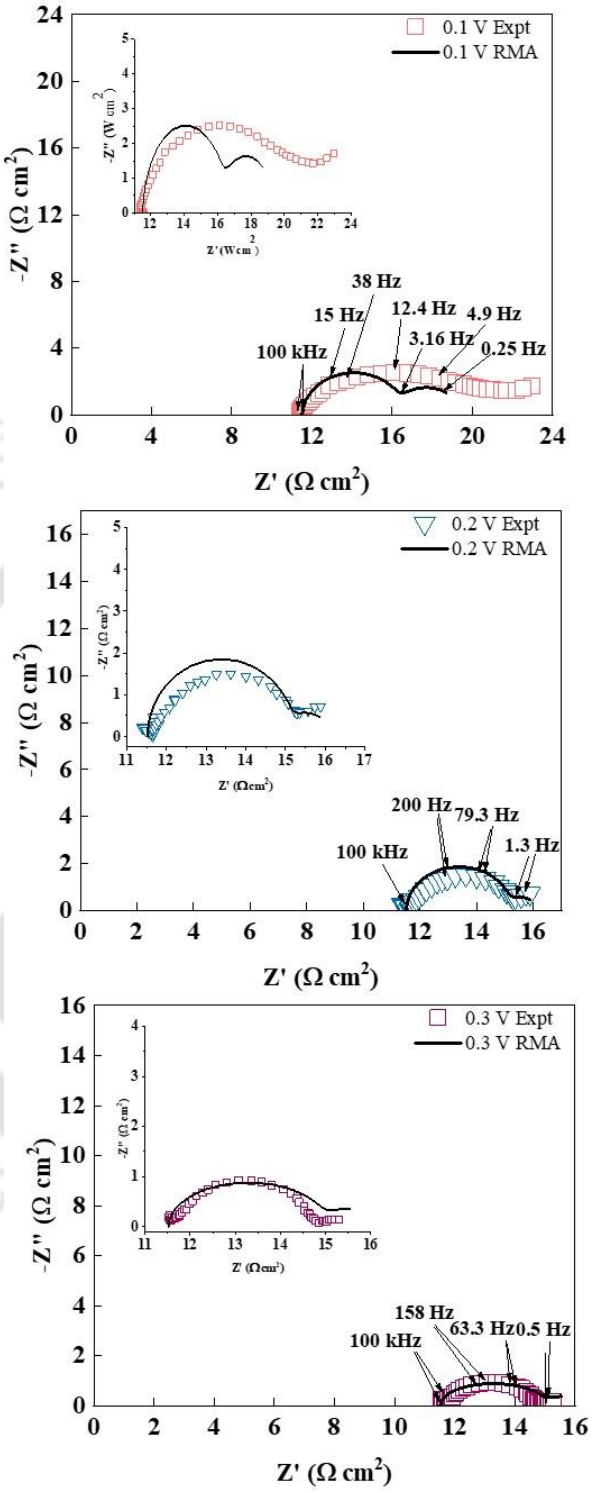

Figure 5.19 Experimental and RMA fitting complex plane plots of Mo in 2.5 wt. % H_2O_2 solution at pH 10 at 0.1, 0.2 and 0.3 V overpotential. The experimental data is shown as dotted lines and fitted data is illustrated as solid line

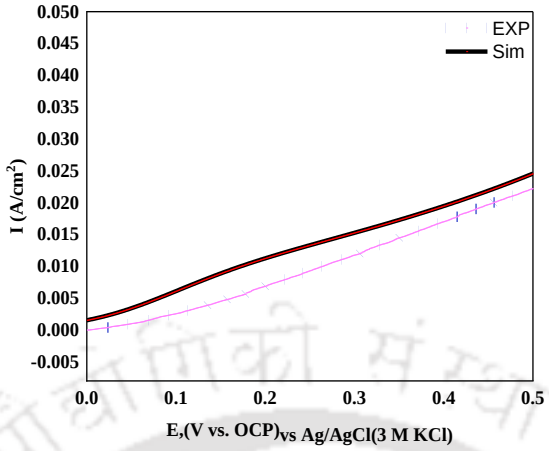

Figure 5.20 Experimental and RMA fitting anodic polarization plots of Mo in 2.5 wt. % H_2O_2 solution. The experimental data is shown as dotted lines and fitted data is illustrated as solid line

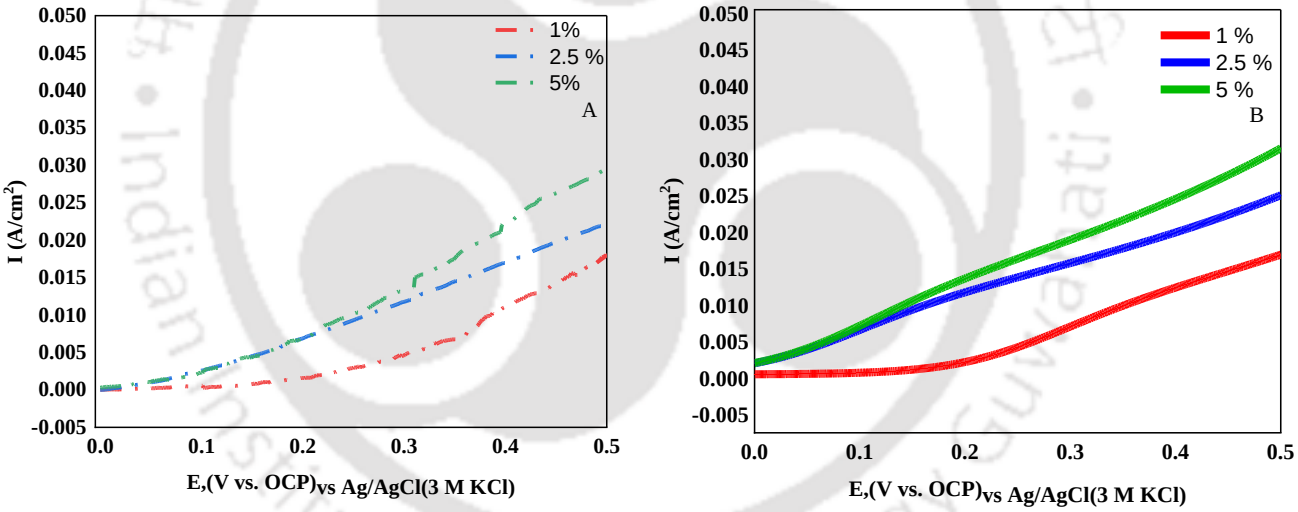

Figure 5.21 Experimental and RMA fitting anodic polarization plots of Mo in 1-5 wt. % H_2O_2 solutions. A.) Experimental data is shown as dotted lines, and B.) fitted data is illustrated as solid lines

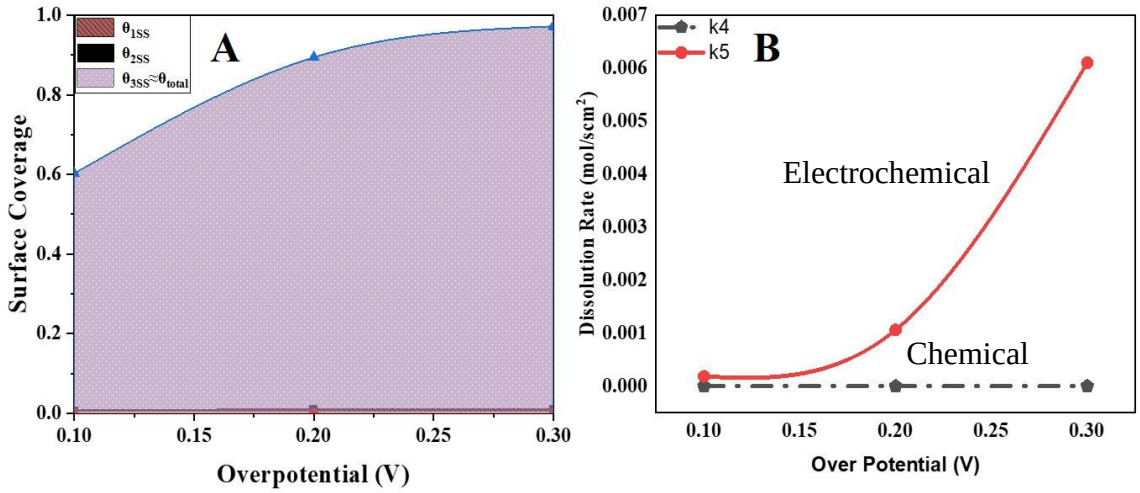

Figure 5.22(A) Steady-state surface coverage distribution of the adsorbed metal species along with the metal with respect to overpotential obtained from the proposed mechanism, (B) Dissolution rates of Mo with respect to overpotential obtained from the proposed mechanism

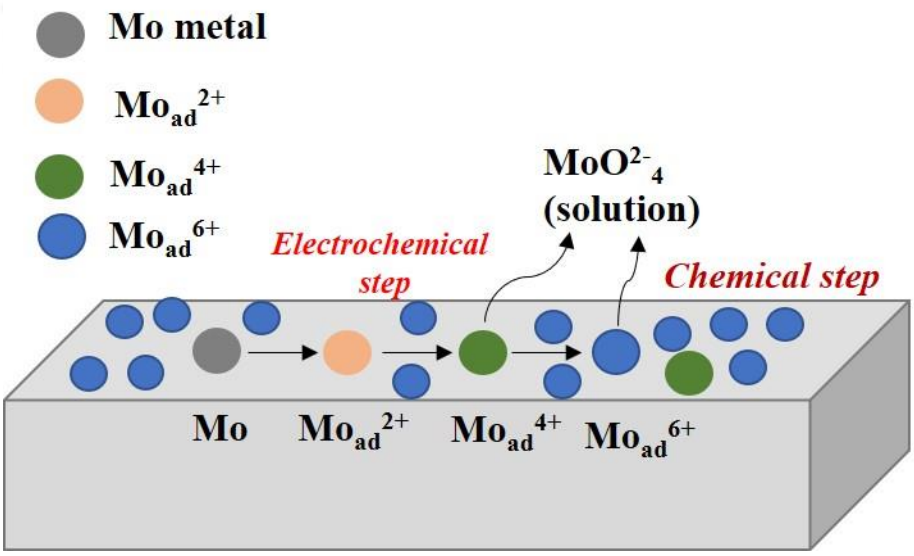

Figure 5.23 Dissolution mechanism of Mo in 2.5 wt. % H_2O_2 at 10 pH at lower overpotential

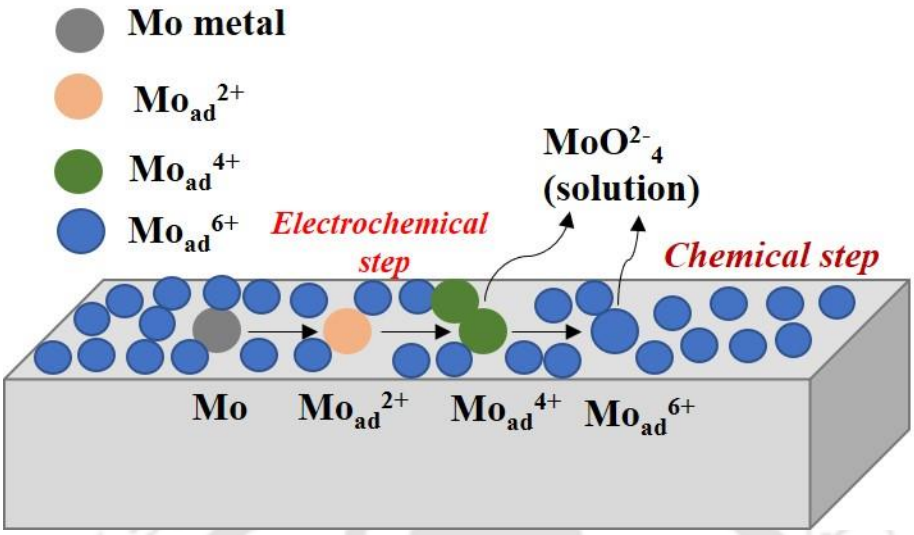

Figure 5.24 Dissolution mechanism of Mo in 2.5 wt. % H_2O_2 at 10 pH at higher overpotential

Table 5.2. Best fit parameters obtained from RMA for EIS data of Mo in 2.5 wt. % H_2O_2 solution at pH 10

Parameters	R_{sol} **(Ω cm^2)**	k10 **(mol s^{-1} cm^{-2})**	b1 **(V^{-1})**	k-10 **(mol s^{-1} cm^{-2})**	b-1 **(V^{-1})**	k20 **(mol s^{-1} cm^{-2})**	b2 **(V^{-1})**	k-20 **(mol s^{-1} cm^{-2})**	b-2 **(V^{-1})**	k30 **(mol s^{-1} cm^{-2})**	b3 **(V^{-1})**	k-30 **(mol s^{-1} cm^{-2})**	b-3 **(V^{-1})**	k40 **(mol s^{-1} cm^{-2})**	k50 **(mol s^{-1} cm^{-2})**	b5 **(mol s^{-1} cm^{-2})**	**τ (mol cm^{-2})**
2.5 % H_2O_2	11.5	9.00E-09	17.5	3.00E-06	-1.5	5.00E-07	3	1.00E-06	0	5.60E-05	14.5	9.00E-09	0	1.00E-12	3.20E-05	17	9.00E-07

Table 5.3 Best fit parameters obtained from RMA for Anodic dissolution data of Mo in 1-5 wt. % H_2O_2 solutions at pH 10

Parameters	k20 **(mol s^{-1} cm^{-2})**	k50 **(mol s^{-1} cm^{-2})**
1 % H_2O_2	1.00E-08	2.60E-05
2.5 % H_2O_2	5.00E-07	3.20E-05
5 % H_2O_2	5.00E-07	3.70E-05

The correlation between k_{20} and k_{50} values with H_2O_2 is given below

$k_{20} = 1E^{-08}[H_2O_2]^{4.2694}$ for 1-2.5 wt. % H_2O_2

$k_{20} = 5E^{-07}$ (constant) for 2.5-5 wt.% H_2O_2

$k_{50} = 2E^{-05}[H_2O_2]^{0.2713}$

CHAPTER 6

Chapter VI: Anodic Dissolution of Molybdenum in Potassium Permanganate Solution by Electrochemical Impedance Spectroscopy: Reaction kinetics

6.1. Motivation

Several works are reported on the effect of various oxidizers on Mo CMP. The oxidizers reported for Mo CMP include H_2O_2 (Qu et al. 2017; Ryu et al. 2021), ammonium sulfate, and glycine (Feng et al. 2014; Yang et al. 2018). However, the results from our research group [Vinay Kumar M.Tech. thesis, Chemical Engineering Department, IIT, Guwahati] show that among the various oxidizers being studied, $KMnO_4$ gives a high polish rate, although the etch rate is low. Especially, the polish rate is significantly higher compared to the H_2O_2-based slurry, which is commonly employed. Thus, understanding the anodic dissolution of Mo in $KMnO_4$ and comparing it with the dissolution behavior of Mo in H_2O_2 solution is the main focus of this chapter.

6.2. Results and Discussions

6.2.1. Etch Rate and Polish Rate Study

The etch rate and polish rate study of Mo was performed in 2.5 wt. % $KMnO_4$ solution at pH 10, is illustrated in Figure 6.1. The polish rate of Mo in 2.5 wt. % $KMnO_4$ was obtained as 125.5 nm/min. The polish rate is significantly higher than the etch rate (15.61 nm/min) of Mo in the same solution. However, from the results shown in Chapter 5, the etch rate of Mo in 2.5 wt. % H_2O_2 solution is 28.1 nm/min (Figure 5.1), which is high from the etch rate of Mo but significantly lower than the polish rate of Mo in 2.5 wt. % $KMnO_4$ solution.

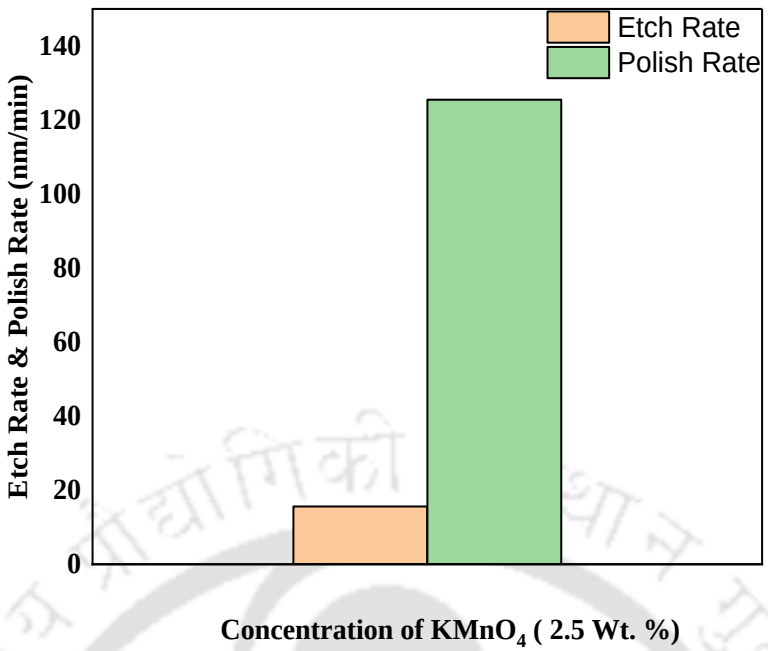

Figure. 6.1 Etch rate and polish rate plot for Mo in blank and 2.5 wt. % $KMnO_4$ at pH 10

6.2.2. Morphology Analysis by FESEM Study

The characteristics of the corrosion product of Mo were analyzed by obtaining FESEM images after being exposed to a 2.5% $KMnO_4$ solution, as shown in Figure 6.2 (A) and (B). As observed from the FESEM images, cluster-like particles were observed at a lower resolution. At a higher resolution, both spike-like structures and clusters were observed. The structures obtained resembled MoO_2 [Mo(IV)] and MoO_3 [Mo(VI)], as reported in the literature (Camacho 2005; Caique D.A. Lima a,**, Jo˜ao Victor Barbosa Moura b, Alexandre de Castro Maciel c, Cleˆanio Luz-Lima c, Lanna I.M. Sinimbu a, Jo˜ao F. Chaves a, Jonatas D.S. Oliveira c, Adnan R. Syed d, Rubem L. Sommer d, Anupama Ghosh e, Carlos L.R. Fragoso f, Marco Cre 2023). The product composition was further confirmed by XPS analysis. In the Mo-H_2O_2 system, also Mo (IV) and Mo (VI) were found in the corrosion product as written in Section 5.2.6.1 (Chapter 5).

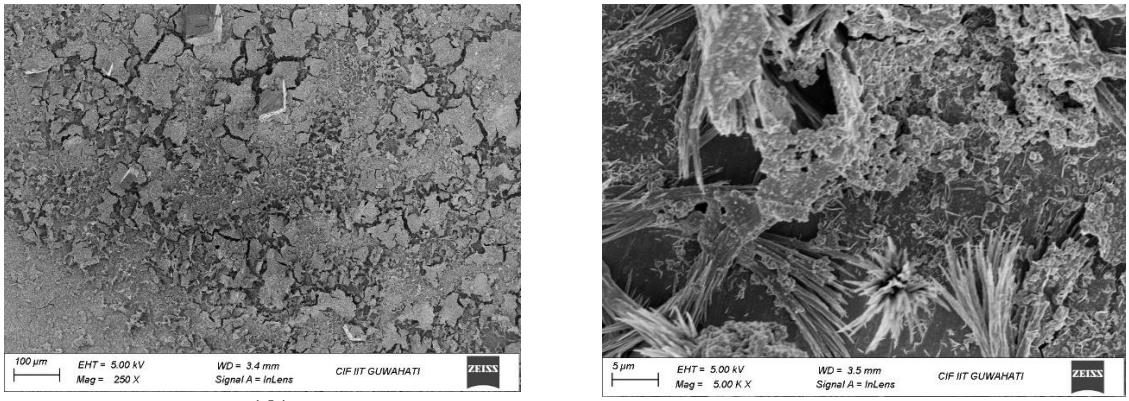

(A) **(B)**

Figure 6.2 FESEM images of corrosion product obtained after exposure of Mo in 2.5 wt. % $KMnO_4$ solution at pH 10

6.2.3. XPS Analysis

The FESEM analysis provided an idea of the morphology of the type of corrosion product. To get an indistinct idea of the composition of the corrosion product obtained by exposing Mo in 2.5 wt. % $KMnO_4$ solution, XPS analysis was performed. Figure 6.3 (A) and (B) show the deconvoluted peaks of Mo 3d and O1S, respectively. The peak fitting was executed following the Gaussian model. The deconvolution of high-resolution Mo 3d spectra obtained the Mo $3d_{3/2}$ peaks. The deconvoluted peaks at 228.8 and 228.7 eV correspond to MoO_2 [Mo (IV)], and the peaks corresponding to 231.6 eV and 231.5 eV are MoO_3 with a +6-oxidation state. Similar observations are reported in the literature (Schroeder et al. 2004; Khademi et al. 2009; Qu et al. 2017; Yang et al. 2017; Ryu et al. 2021). A main peak was observed at 531 eV for O1S spectra, which, upon deconvolution, gives peaks at 529.9, 531.24, 532.01, and 533.52 eV. The peak at 529.9 eV corresponds to the oxygen bound to Mo (VI) (Ishfaq et al. 2014). The peak corresponding to 531.24 and 532.01 eV is lattice oxygen. Similar observations have been reported in the literature (Choi et al. 2011; Liu et al. 2024). The peak equivalent to 533.52 eV is due to OH^- ions adsorbed on the metal surface. Other forms of Mo oxides were not observed.

Since $HMoO_4^{2-}$ is soluble in nature hence, the collection of the corrosion product was not possible.

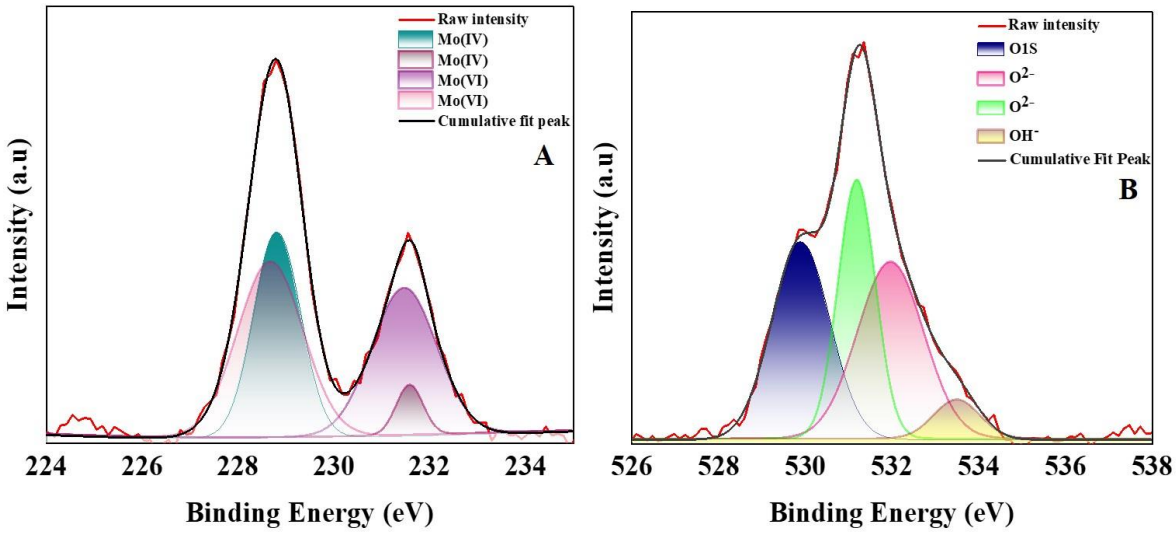

Figure 6.3 Detailed spectra of (A) Mo 3d and (B) O1S for XPS of the corrosion product obtained by exposure of Mo in 2.5 wt. % $KMnO_4$ at pH 10

6.2.4. Potentiodynamic Polarization

The OCP plot indicated that the system became stable after 2000 s (Figure 6.4). The open circuit potential value for Mo is 2.5 wt. % $KMnO_4$ concentration at pH 10 is 0.06 V. The potentiodynamic polarization curve of Mo immersed in 2.5 wt. % $KMnO_4$ solution at pH 10 is shown in Figure 6.5. The anodic polarization curve was observed to show an increase in the current density with the increase in potential. The rate of increase of current density with respect to potential was less till 0.2 V. After 0.2 V, a steady increase in current density was observed, indicating the active dissolution of Mo up to 0.5 V potential (at higher overpotential). Compared to the anodic polarization of Mo in 2.5 wt. % H_2O_2 solution as reported in Chapter 5, Figure 5.3, the rate of change of current density is observed to be higher in the case of Mo-$KMnO_4$ system.

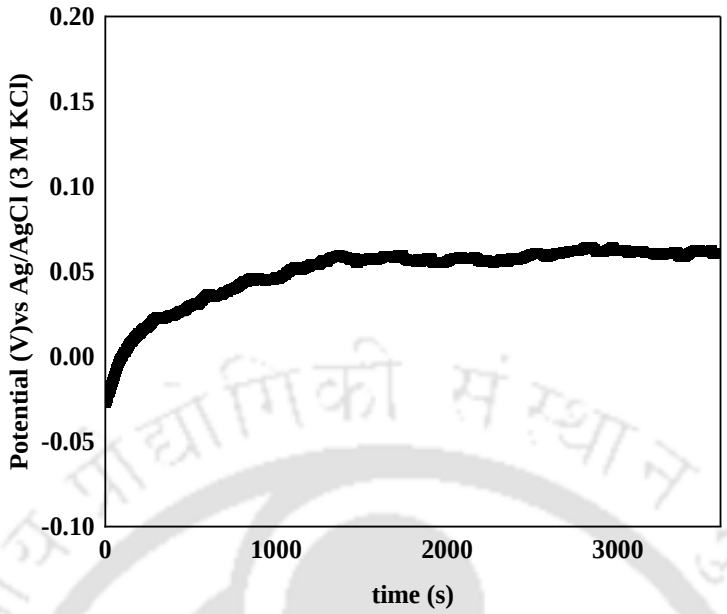

Figure 6.4 Open circuit potential plot for Mo in 2.5 wt. % $KMnO_4$ solution at pH 10

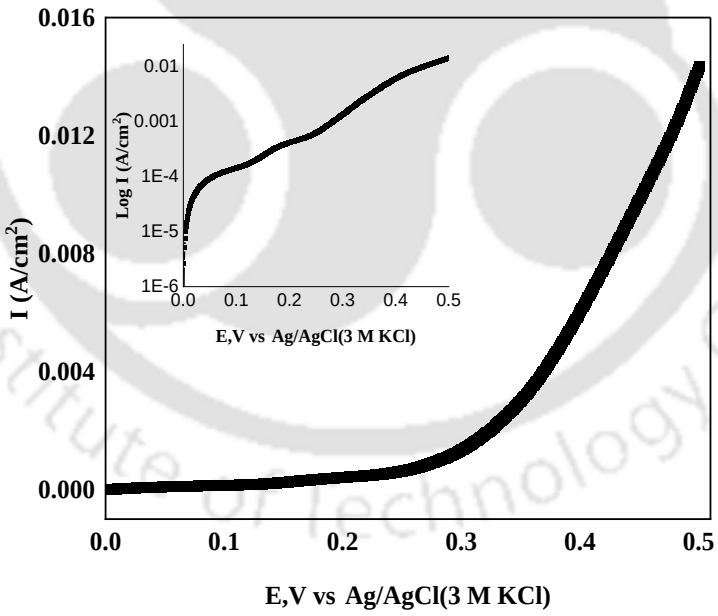

Figure 6.5 Anodic polarization plot (vs. OCP) for Mo in 2.5 wt. % $KMnO_4$ solution at pH 10

6.2.5. Electrochemical Impedance Spectroscopy Measurement

EIS measurements were carried out for Mo in 2.5 wt. % $KMnO_4$ solution (pH 10) at various overpotentials, 0.1 V, 0.2 V and 0.3 V w.r.t. OCP. The results obtained from the EIS

experiments are shown in Figures 6.6-6.9. Before further analyzing the EIS data, the Kramers Kronig Technique was performed to validate the data for stability, linearity, and casualty. The KKT fitting data is presented in Figures 6.6-6.9 (dotted lines for experimental data and solid lines for simulated data). The impedance data represented in the Nyquist plot exhibited a capacitive loop at a higher frequency and Warburg impedance at a lower frequency. The capacitive loop is significant for charge transfer resistance, and Warburg impedance signifies diffusive behavior at a lower frequency range. A decrease in the overall impedance was observed at the respective DC potential since it increased from 0.1 to 0.3 V. From the decreasing impedance behavior, it is evident that the dissolution rate increases with increasing overpotential, as observed in the polarization measurement experiments. Figures 6.6-6.9 B and C illustrate the Bode plot and phase angle plot, respectively. The impedance modulus in the Bode plot and the angle in the phase angle plot decreased with increased overpotential. The trend in all three overpotentials is similar, as observed in the Nyquist plot. The Electrical equivalent circuit (EEC) fitting was performed using ZSimpwin® Software to analyze the EIS data quantitatively. The EEC circuit used for the impedance data simulation is illustrated in Figure 6.10. The EEC circuit consists of the following elements. Solution resistance (R_s), which is responsible for the resistance supplied by the solution. Constant phase element (Q_{CPE}) and charge transfer resistance R_{ct} were used for the capacitive loop that associates with the electrical double layer and the charge transfer resistance. The straight line followed after the capacitive semicircle is modelled using a Warburg impedance and resistance (W-R). The Warburg impedance is observed when the predominating reaction is diffusion-controlled. This is observed at lower frequencies when the reactants diffuse further and increase the impedance value. The best-fit parameters with the proposed circuit are represented in Table 6.1 (error <5%). The resistance and Warburg impedance values are found to decrease with increasing

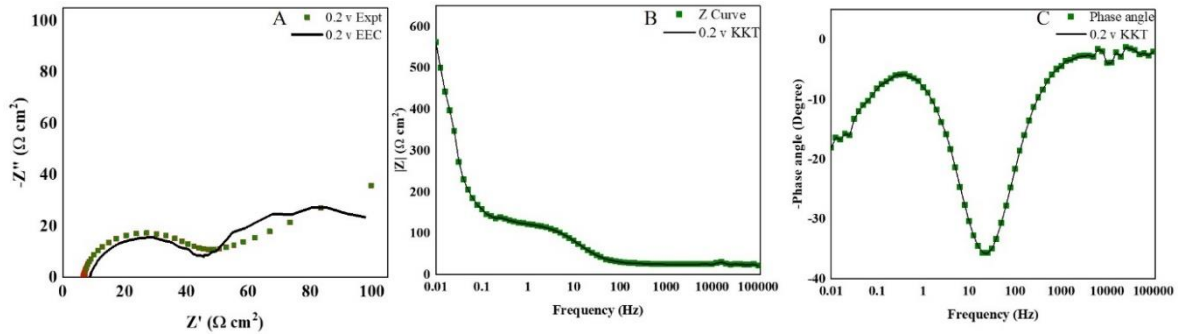

Figure 6.6 EIS plots for Mo in 2.5 wt. % $KMnO_4$ solution at pH 10 at 0.2 V overpotential A) Nyquist plot with EEC fitting B) Bode plot with KKT fitting C) Phase angle plot with KKT fitting. Dotted line represents experimental data and solid line represents fitted data

overpotential. The constant phase element was observed to increase with increasing

overpotential.

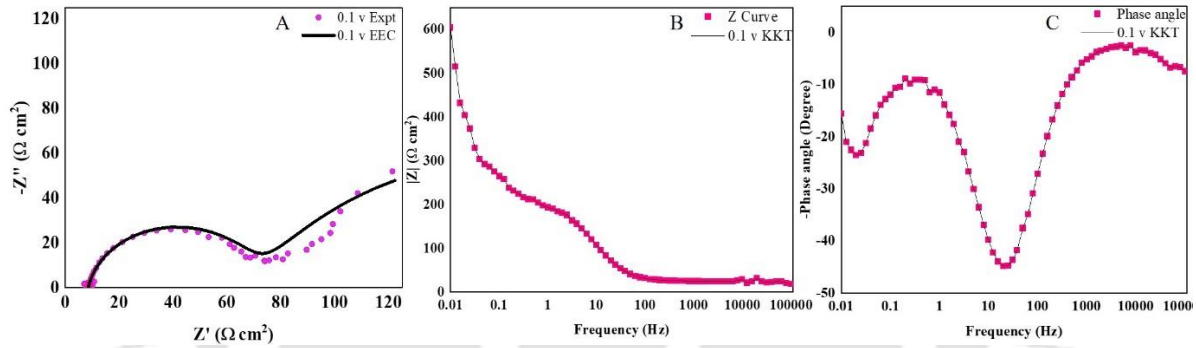

Figure 6.7 EIS plots for Mo in 2.5 wt. % $KMnO_4$ solution at pH 10 at 0.1 V overpotential A) Nyquist plot with EEC fitting B) Bode plot with KKT fitting C) Phase angle plot with KKT fitting. Dotted line represents experimental data and solid line represents fitted data

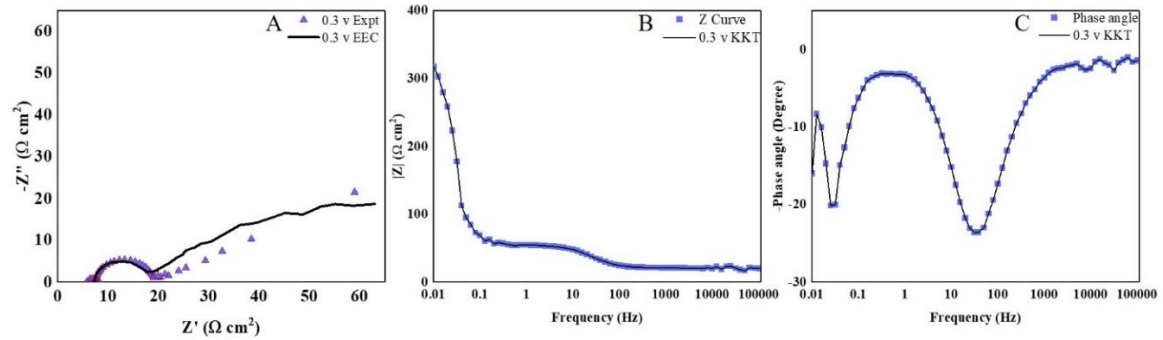

Figure 6.8 EIS plots for Mo in 2.5 wt. % $KMnO_4$ solution at pH 10 at 0.3 V overpotential A) Nyquist plot with EEC fitting B) Bode plot with KKT fitting C) Phase angle plot with KKT fitting. Dotted line represents experimental data and solid line represents fitted data

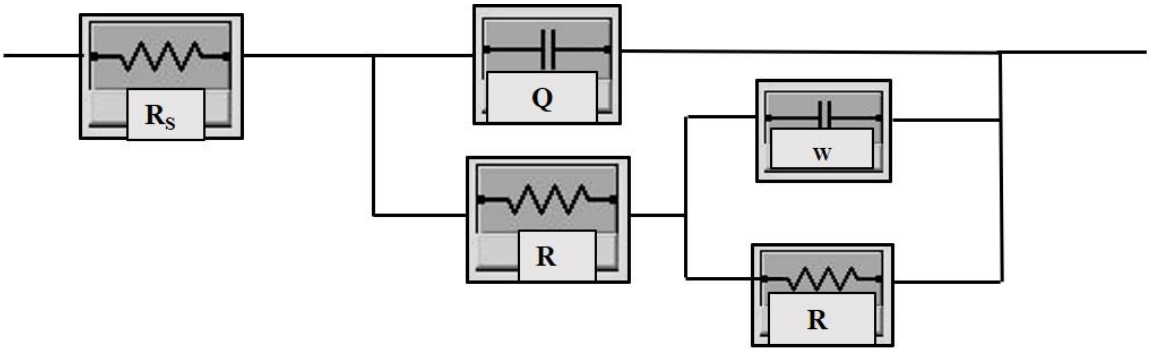

Figure 6.9 Electrochemical equivalent circuit obtained from EIS data for Mo in 2.5 wt. % $KMnO_4$ solution at pH 10

Table 6.1. EEC Fitting parameters of EIS data of Mo in 2.5 wt. % $KMnO_4$ solution at pH 10

Overpotential (V)	R_s (Ωcm^2)	Q_{CPE}		R_{ct} (Ωcm^2)	W (Ωcm^2)	R (Ωcm^2)
		$Y_o \times 10^{-5}$ ($\Omega^{-1} cm^{-2} S^n$)	n			
0.1	9.294±0.11	1.7±0.01	0.9	56.14±0.18	0.057±0.00	185±0.00
0.2	8.835±0.14	4.3±0.01	0.9	31.32±0.07	0.047±0.02	174±0.01
0.3	7.3±0.12	5.7±0.03	0.9	9.76±0.07	0.042±0.01	89±0.00

6.2.6. Reaction Mechanism Analysis (RMA)

We have discussed EEC fitting and provided a quantitative analysis in the previous Section 6.2.5. However, it has limitations in providing a detailed analysis of the EIS data (Amrutha et al. 2018; Baranwal and Rajaraman 2019). Thus, to understand the dissolution mechanism of Mo in alkaline solutions containing oxidizers, the reaction mechanism analysis was performed. The RMA was performed by considering the proposed reaction reported in Chapter 5. The comparison of RMA parameters with Mo-H_2O_2 and Mo-$KMnO_4$ is performed in the following context.

The impedance data calculated from the simulation is shown in Figure. 6.10 in a dotted line and experimental data in a solid line. Further, the steady-state current values simulated from equation 5.6 (Chapter 5) are also compared with the anodic polarization plot, as shown in Figure 6.11. Although a quantitative difference exists between experimental and simulated

data, still the number and pattern of loops observed in the impedance measurement and all the experimental trends observed in both polarization and impedance measurements are observed by the suggested mechanism. The best fit RMA parameters are presented in Table 6.2. From the RMA parameters obtained, the surface coverage of Mo^{2+}, Mo^{4+}, and Mo^{6+} is estimated for various overpotentials, which is presented in Figure. 6.12 (A). The surface coverage of both adsorbed species ($Mo^{2+}$and Mo^{4+}) is very negligible (~0.01) at all the overpotentials being investigated, while the surface coverage of Mo^{6+} is decreasing with overpotential (0.97 at 0.1 V to 0.99 at 0.3 V). Thus, the surface is occupied mainly by Mo^{6+} at any overpotential level. It reveals that the conversion of Mo^{4+} to Mo^{6+} is very rapid compared to that of Mo to Mo^{4+} via Mo^{2+}. Further, the surface coverage is lower at a higher overpotential. This is mainly ascribed to the low k_4 value, i.e., the dissolution of Mo^{6+} via chemical step is insignificant, while the k_5 value (conversion of Mo^{4+} to Mo^{6+}) is higher. To be precise, the surface coverage obtained from the RMA simulation confirms maximum coverage by the adsorbed species Mo_{ad}^{6+}, corresponding to MoO_2, as confirmed from FESEM images. The total current estimated is resolved into two components: (1) one due to the chemical step (k_4) and the other one due to the electrochemical step (k_5); the same is plotted in Figure. 6.12 (B). It is evident that the contribution to the total dissolution by chemical step (k_4) is significantly lower and is almost constant concerning the overpotentials. On the other hand, the contribution by the electrochemical step (k_5) is significantly higher and is also increasing with overpotential. Thus, the overall dissolution in the form of MoO_4^{2-} occurs mainly via the electrochemical step, whereas the chemical step (k_4) generates oxides (MoO_2) on the metal surface. These findings are also consistent with the Pourbaix diagram, FESEM, and XPS findings.

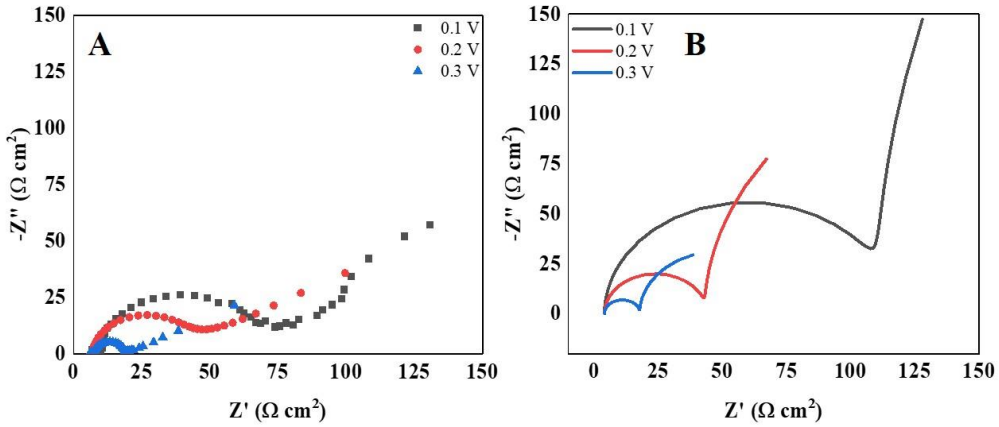

Figure. 6.10 A.) Experimental and B.) RMA fitting complex plane plots of Mo in 2.5 wt. % $KMnO_4$ solution at pH 10 at 0.1, 0.2 and 0.3 V overpotential. The experimental data is shown as dotted lines, and fitted data is illustrated as a solid line

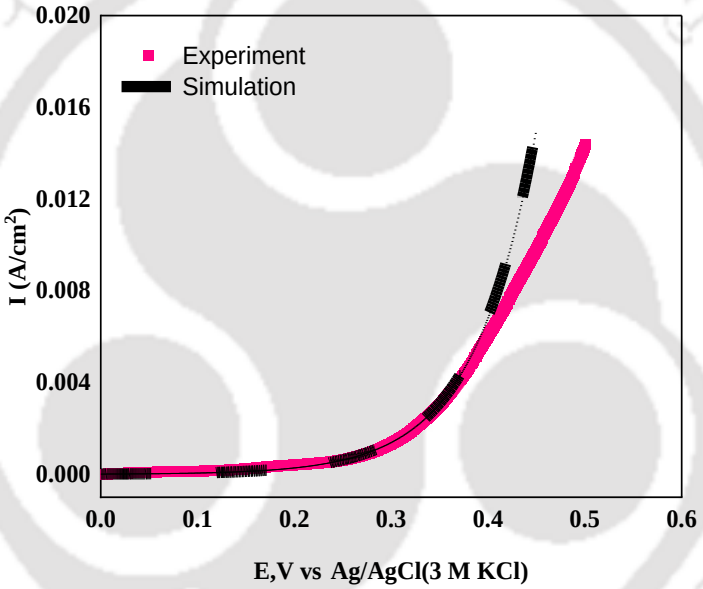

Figure. 6.11 Experimental and RMA fitting anodic polarization plots of Mo in 2.5 wt. % $KMnO_4$

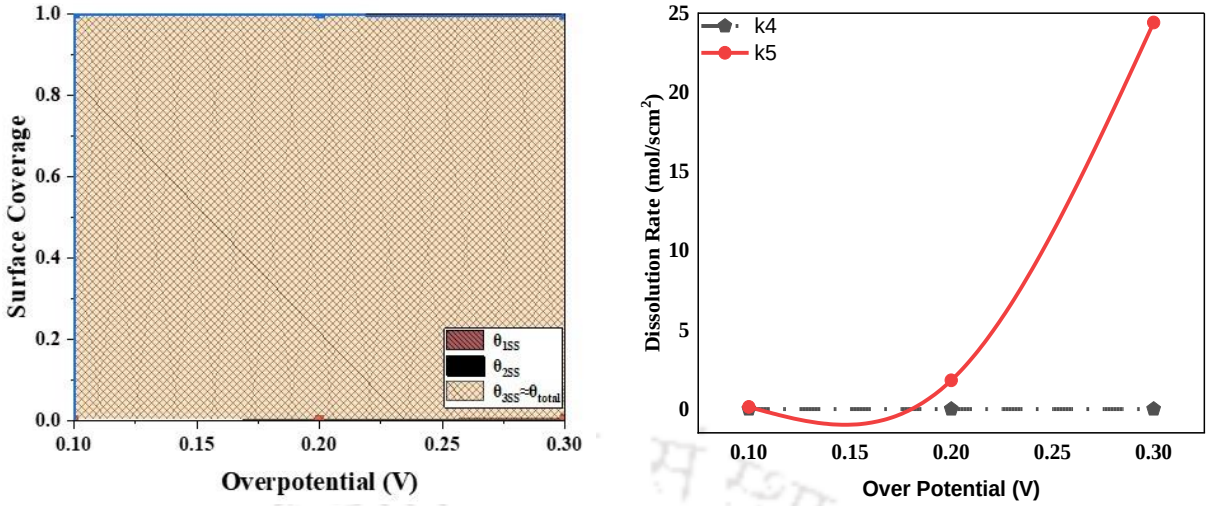

Figure. 6.12 Steady-state surface coverage distribution of the adsorbed metal species along with the metal with respect to overpotential obtained from the proposed mechanism (B) Dissolution rates of Mo with respect to overpotential obtained from the proposed mechanism

Table 6.2. Best fit parameters obtained from RMA for EIS data of Mo in 2.5 wt. % $KMnO_4$ solution at pH 10

Parameters	**R_{sol}** (Ω cm^2)	**k10** (mol s^{-1} cm^{-2})	**b1** (V^{-1})	**k-10** (mol s^{-1} cm^{-2})	**b-1** (V^{-1})	**k20** (mol s^{-1} cm^{-2})	**b2** (V^{-1})	**k-20** (mol s^{-1} cm^{-2})	**b-2** (V^{-1})	**k30** (mol s^{-1} cm^{-2})	**b3** (V^{-1})	**k-30** (mol s^{-1} cm^{-2})	**b-3** (V^{-1})	**k40** (mol s^{-1} cm^{-2})	**k50** (mol s^{-1} cm^{-2})	**b5** (mol s^{-1} cm^{-2})	τ (mol cm^{-2})
2.5 % $KMnO_4$	4	1.0E-06	9	9.00E-06	0	1.00E-07	6	0	0	1.00E-03	10	1.00E-12	0	1.00E-12	1.00E-02	26	5.00E-06

6.3.7. Comparison of Dissolution Behavior of Mo-$KMnO_4$ and Mo-H_2O_2 System

The dissolution behavior of Mo in the presence of oxidizers was investigated (H_2O_2 and $KMnO_4$) as reported in Chapter 5 and in the present chapter. There is a contrast in the dissolution behavior of Mo in the presence of $KMnO_4$ in terms of etch rate and polish rate. The etch rate of Mo observed in the presence of $KMnO_4$ is less than that in H_2O_2; however, the polish rate of Mo in $KMnO_4$ is significantly high. The surface coverage of Mo oxides in the H_2O_2 system follows an increasing trend from 60 % to 97 % as the overpotential increases. In the $KMnO_4$ system, the surface coverage decreases from higher to lower overpotential (99.7 % to 99.3 %), though the change is insignificant. The dissolution rate at 0.3 V overpotential is 0.006 and 25 mol/Scm^2 for H_2O_2 and $KMnO_4$, respectively. Also, the anodic polarization behavior of Mo in $KMnO_4$ solution shows a higher current density rate with increasing overpotential. EIS measurement confirmed the diffusion behavior of Mo at lower frequencies. From all the experimental as well as RMA observations, it can be concluded that the oxide formation for Mo is rapid (significantly high dissolution rate) in the presence of $KMnO_4$, and the oxide layer covers the metal surface, which hinders the contact of metal with the oxidizer. However, when the oxide layer is removed due to external force (higher overpotential or physical action), the dissolution of Mo is very rapid, resulting in a high polish rate value. A schematic of the proposed dissolution is shown in Figure 6.13. The schematic diagram of comparison of the dissolution mechanism of Mo in H_2O_2 and $KMnO_4$ system is shown in Figure 6.14.

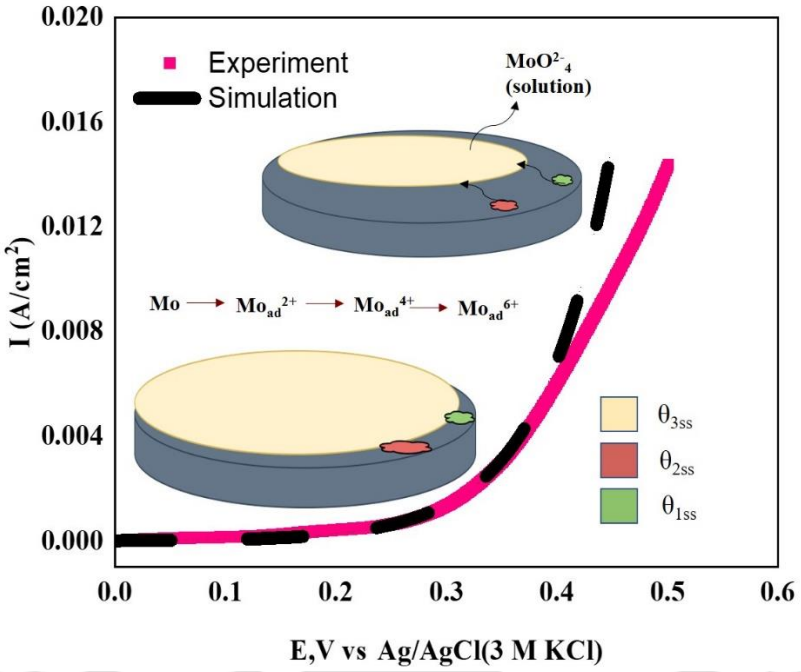

Figure. 6.13 Proposed mechanism of Mo dissolution in the presence of $KMnO_4$ solution

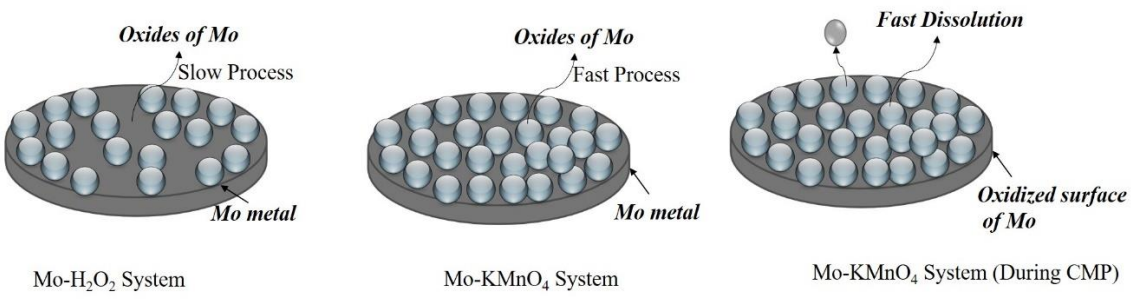

Figure 6.14 Comparison of dissolution mechanism of Mo in H_2O_2 and $KMnO_4$ system

From Chapters 5 and 6 we got a vivid idea about the mechanistic analysis of Mo in H_2O_2 and $KMnO_4$ media through reaction mechanism analysis. In the next chapter we will discuss the mechanistic analysis of carbon steel corrosion using the reaction mechanism analysis.

CHAPTER 7

Chapter VII: Investigation of Carbon Steels (API 5L X52 and API 5L X60) dissolution in CO_2-H_2S Solutions in the presence of acetic acid: Mechanistic Reaction Pathway and Kinetics

7.1. Motivation

Oil and gas industries experience significant failures of carbon steel due to corrosion (Ochoa et al. 2015). It is reported that more than 50 % of pipeline failures occur due to corrosion due to CO_2 and H_2S [1-3]. Oil recovery can be enhanced by injecting produced water into wells. Besides salts of chlorides and bicarbonates, volatile fatty acids (VFA's) are also found in produced water. Acetic acid is found in higher amount than other VFA's such as propionic acid, formic acid, etc. (Kahyarian et al. 2016). There are several works reported on effect of acetic acid on corrosion rate of CS in CO_2-H_2S solutions (Singh and Gupta 2000; Santos and Lo 2014; Yaro et al. 2015; Al-janabi 2020; Talukdar and Rajaraman 2020). However, the comparison of carbon steel of various grades has not been investigated in detail. Hence, the same has been focused on in this study.

7.2. Results and Discussions

7.2.1. Weight Loss Measurements

The immersion tests were performed for X52 and X60 for varying acetic acid concentrations (0, 500, 1000 ppm) at constant CO_2 (3 bar) and H_2S (0.001 bar) partial pressures in 3.5 wt. % NaCl solution. The results are shown in Figure 7.1. As the results show, the CR increases with acetic acid concentration for both steels. An increasing trend of CR with ascending acetic acid concentration was observed. The corrosion rate of carbon steel X60 was observed to be higher than X52 at 40 ^oC at all acetic acid concentrations (Rihan 2013). Thus, it is clearly evident from

these results that the CR is significantly influenced by CS grade. Electrochemical experiments were performed to understand the corrosion behavior further, as discussed below.

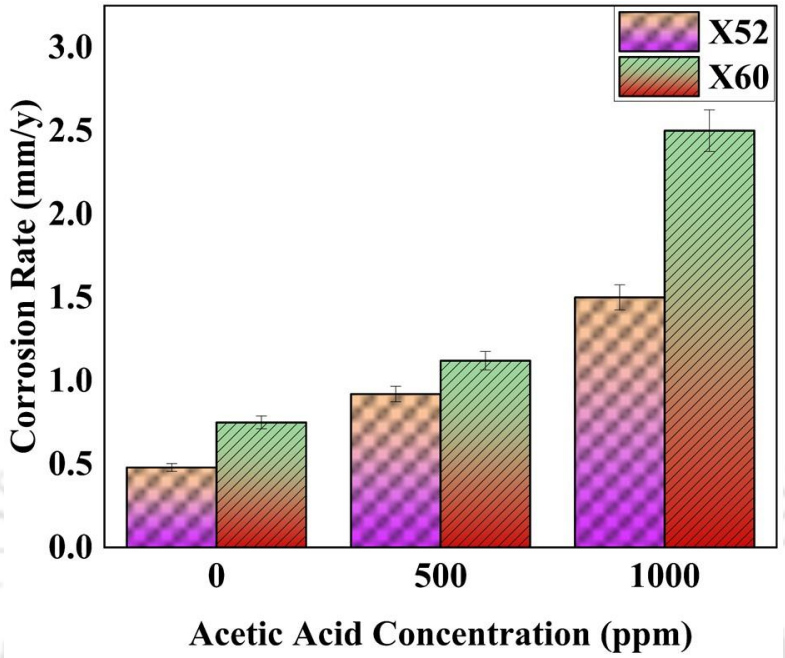

Figure 7.1 Corrosion rate of carbon steels (X52 and X60) in CO_2-H_2S system and acetic acid in the presence of 3.5 wt. % NaCl at 40 ^oC

7.2.2 Potentiodynamic Polarization Measurements

The potentiodynamic polarization measurements were performed for both the steels at the same conditions as followed in the immersion test. The acquired results are shown in Figure 7.2 and Figure 7.3. The major observation found from these plots is that the increase in acetic acid concentration leads to an increase in cathodic current density without a significant change in anodic current density. Thus, the increase in CR with respect to acetic acid concentration is mainly due to the increase in cathodic reaction rate. Similar observations were also reported in the literature stating that acetic acid is responsible for producing hydrogen ions, which are accountable for increasing the CR (Tran et al. 2014). The equations below show the cathodic reactions taking place where acetic acid (CH_3COOH) gets dissociated to acetate ion (CH_3COO^-) and hydrogen ion (H^+). The hydrogen ion further reduces to form H_2.

$$CH_3COOH \rightarrow CH_3COO^- + H^+ \quad 7.1$$

$$H^+ + e^- + H_{ad} \rightarrow H_2 \quad 7.2$$

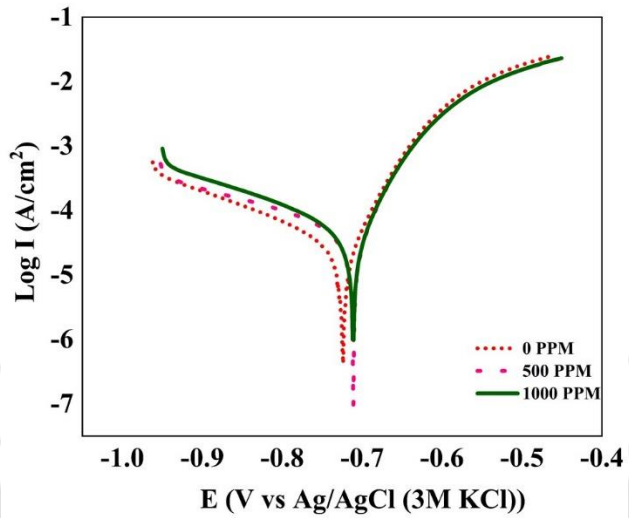

Figure 7.2 Polarization curves of carbon steel X52 acquired in 3.5 wt. % NaCl solution containing CO_2-H_2S and varying acetic acid concentrations (0, 500, 1000 PPM) at 40 ºC

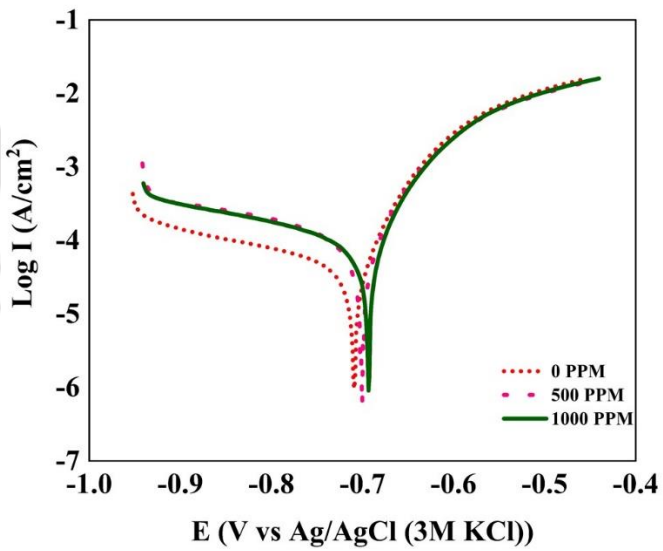

Figure 7.3 Polarization curves of carbon steel X60 acquired in 3.5 wt. % NaCl solution containing CO_2-H_2S and varying acetic acid concentrations (0, 500, 1000 PPM) at 40 ºC

The tafel fit kinetic parameters, corrosion current density (I_{corr}) and corrosion potential (E_{corr}) obtained from the potentiodynamic polarization data using Gamry software are listed in Table 7.1. From the fitted kinetic parameters, the corrosion current density of X60 was found to be higher than the corrosion current density of X52 at all concentrations of acetic acid. The increase in corrosion current density with increase in acetic acid concentration was also noted for both the carbon steels. The corrosion potential was also observed to increase with increasing acetic acid concentration. The trends obtained in potentiodynamic polarization study corroborate with the trends obtained in immersion test. An increase in both E_{corr} and I_{corr} values clearly suggest that acetic acid strongly influences the cathodic reaction rates for both the steels as per mixed potential theory (Basics of Electrochemical Impedance Spectroscopy; Lei Zhang, Wen Zhong, Jianwei Yang; Perez).

Table 7.1 Corrosion parameters for carbon steel X52 and X60 at various acetic acid concentrations at 40 ^{o}C

Carbon Steel	Acetic Acid Concentration (ppm)	I_{corr} (mA)	E_{corr} (mV) vs Ag/AgCl
X52	0	17.5	-724
	500	31.5	-711
	1000	33.7	-710
X60	0	39.3	-709
	500	58.5	-701
	1000	71.3	-693

7.2.3. Electrochemical Impedance Spectroscopy

Figure 7.4 (a-b) show the Nyquist plots acquired from EIS measurements for carbon steel samples X52 and X60, respectively at 40 °C exposed at various concentrations of acetic acid (0, 500 and 1000 ppm). Two loops (capacitance followed by an inductance) were clearly observed for X52 in high-mid frequency regime with a third pseudo capacitive loop in the lower frequency regime. Whereas, for X60 three loops were clearly observed in high-low

frequency regime. For lower concentrations (0-500 ppm), a capacitive loop at higher frequency followed by an inductive loop at mid frequency and another capacitive loop at lower frequency were observed. At 1000 ppm acetic acid concentration, three capacitance loops were observed. Further, the capacitance loop observed at higher frequency is depressed in nature for both the steel samples. The overall impedance was observed to decrease with increasing acetic acid concentration for both the steels that explains the increase of corrosion rate with increase in acetic acid concentration as observed in immersion and polarization measurements.

The capacitive loop at higher frequency indicates double-layer capacitance with charge transfer resistance associated with faradaic reactions. The depressed semi-circle is suggested to be due to heterogeneous surface roughness and a non-uniform current density distribution over the surface (Amrutha et al. 2018). The inductive loop suggests that the dissolution of Fe may take multiple steps, and an adsorbed intermediate can also be involved. The EIS data was further analyzed quantitatively by an electrical equivalent circuit, shown in Figure 7.5, and the EEC simulated data is presented in Figure 7.4 (a-b). Here, Rs represents solution resistance, and Q1 and R1 correspond to the constant phase element (CPE) associated with the electrical double layer and charge transfer resistance. Three Maxwell pairs, Q_2 - R_2, L – R_L, and Q_3 – R_3, were used to model the impedance data in the mid-low frequency range. These Maxwell pairs are associated with both faradaic and non-faradaic reactions, such as the relaxation of adsorbed intermediates. It is to be noted that CPE was used instead of an ideal capacitor to model the depressed semi-circle. Although two Maxwell pairs were initially tested, the fitting was better with the suggested circuit.

The best-fit parameters found from the EEC analysis are presented in Table 7.2. It is clear from the parameters that Q_1, Q_2, and L are increasing, and R1 and R2 are decreasing with an increase in acetic acid concentration. It is attributed to the decrease in total impedance associated with faradaic and non-faradaic reactions. The charge transfer resistance (R_{ct}) is estimated based on

effective resistance from R_1 and R_2 and is presented in Table 7.2 (Basics of Electrochemical Impedance Spectroscopy). R_{ct} value decreases with an increase in acetic acid concentration and is lower for carbon steel X60. This explains the increase in corrosion rate with increasing acetic acid concentration, and a higher corrosion rate was observed for X60. The Bode plot of the EIS data is illustrated in the appendix (Figure A1 and A2).

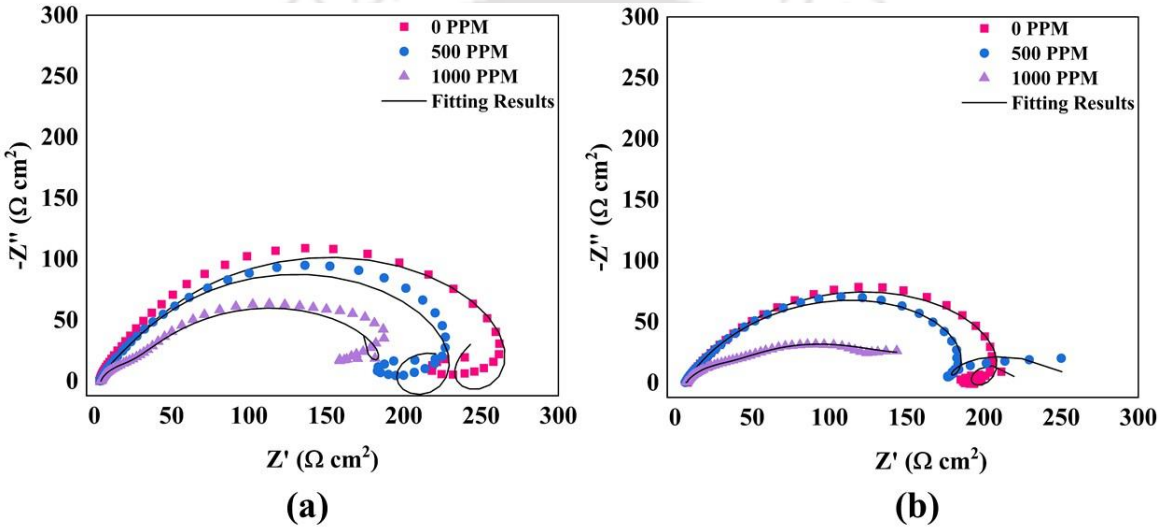

Figure 7.4 Nyquist plots obtained from EIS and EEC fitting for carbon steels (a) X52 and (b) X60 obtained in 3.5 wt. % CO_2-H_2S system at varying acetic acid concentrations (0,500,1000 ppm) at 40 °C

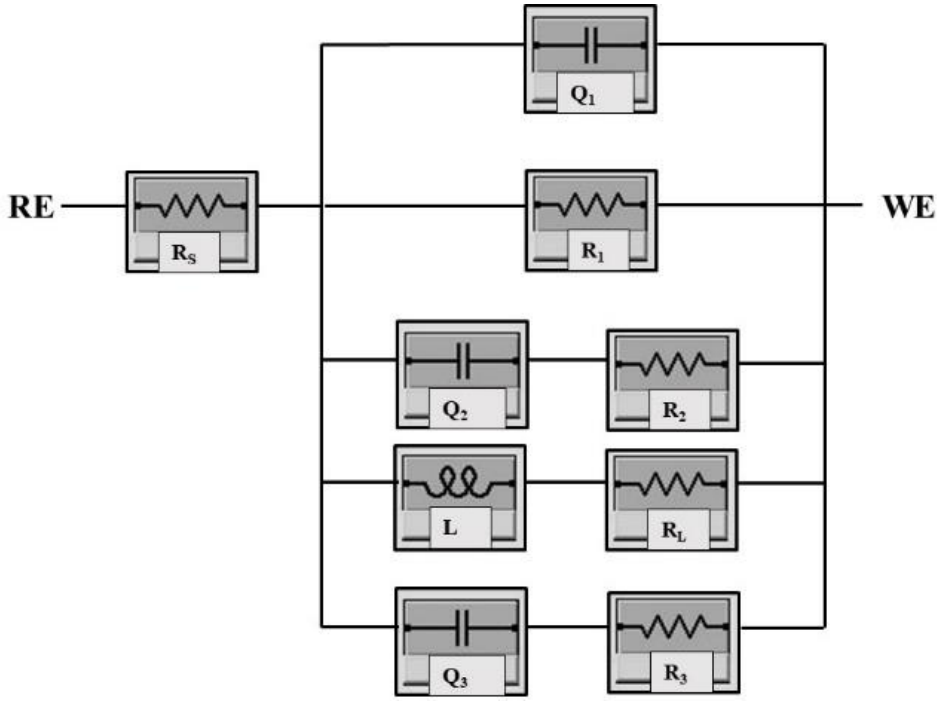

Figure 7.5 Electrical equivalent circuit used for fitting EIS data for carbon steels acquired in 3.5 wt. % CO_2-H_2S system at varying acetic acid concentrations at 40 ºC

Table 7.2: Fitting parameters of carbon steel X52 and X60 exposed to 3.5 wt. % NaCl with CO_2-H_2S at varying concentrations of acetic acid (0-1000 ppm) at 40 ºC

CS	Acetic Acid Conc. (ppm)	R_S, Ωcm^2	CPE $Yo \times 10^{-3}$ Ωcm^{-2}	n	R_1, $\Omega\ cm^2$	Q_1 $Yo \times 10^{-2}$ $\Omega\ cm^{-2}$	n	R_2, Ωcm^2	$L \times 10^2$, H cm^2	R_3, Ω cm^2	Q_2 $Yo \times 10^{-5}$ $\Omega\ cm^{-2}$	n	$R_4 \times 10^3$, $\Omega\ cm^2$	R_{ct}, Ω cm^2
X52	0	4.3	0.2	0.8	500	2.7	0.8	675.5	9.6	884	1.6	0.8	1.1	287.3
	500	4.4	34.8	0.8	409.2	75.1	0.9	624.1	14.1	674.2	38.8	0.8	1.0	247.1
	1000	4.3	108	0.7	302.1	261	0.8	600.4	49.2	400	108	1	0.8	200.9
X60	0	9.8	4.9	0.7	280.4	6.0	0.6	654.1	66	473.2	3.2	1	3.8	196.2
	500	8.2	6.0	0.7	243.4	7.1	1	575.5	53.9	448.6	22.5	0.8	3	171
	1000	6.2	33.9	0.6	196.8	8.7	0.8	465.9	78.2	350	48	0.6	4.7	138.3

7.2.4. Morphology Analysis

The microstructure analyses for carbon steels X52 and X60 are shown in Figure 7.6. Banded ferrite and pearlite were observed in X52 (Akeer et al. 2013) while finely grained ferrite with coarse acicular pearlite nature was observed in X60 (Calan-Canche et al. 2019). It is clearly evident that X52 has relatively higher ferrite content as compared to X60. It is also reported in the literature that carbon steel with more ferrite content offers better corrosion resistance (Rihan 2013). The surface morphology of the carbon steels after being exposed to a corrosive environment for 24 h was analysed. Figure 7.7 shows the FESEM images of X52 and X60 at various acetic acid concentrations at 40 ^{o}C. Uniform corrosion was observed for both X52 and X60 at 0 ppm acetic acid concentration, while the X60 surface was comparatively more corroded with surface cracks (Karimi Abadeh and Javidi 2019). In the presence of acetic acid (500 ppm and 1000 ppm) as shown in Figure 7.7, X60 was more severely corroded than X52. Although surface cracks were observed for both the steels, X60 possesses more surface cracks than X52 (López et al. 2003). It is clearly evident from these images that X60 is more corroded compared to that of X52 as observed in weight loss and electrochemical studies at all acetic acid concentrations.

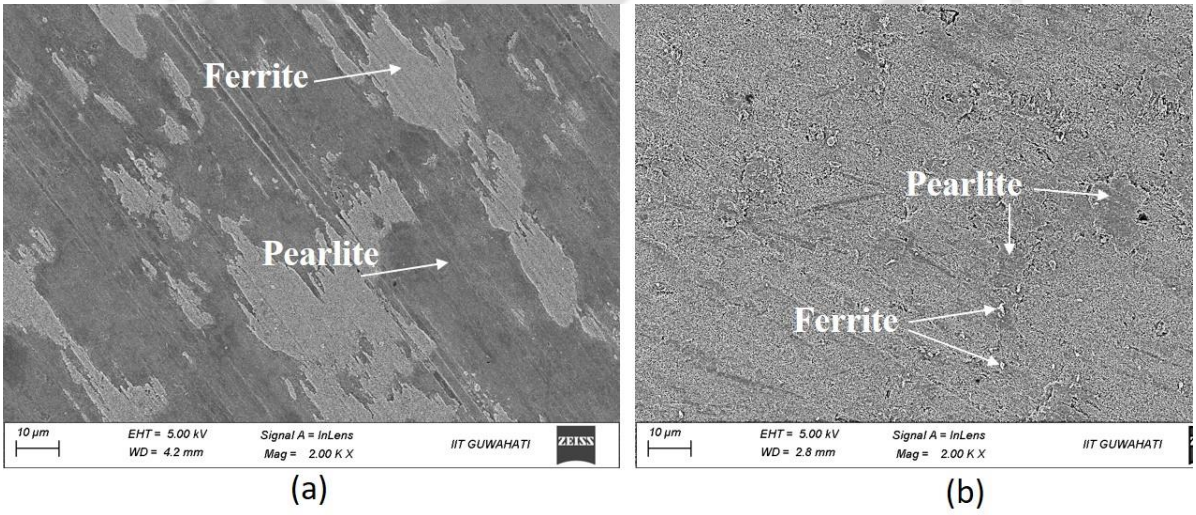

Figure 7.6 Surface morphology of carbon steel specimens. (a) X52 (b) X60

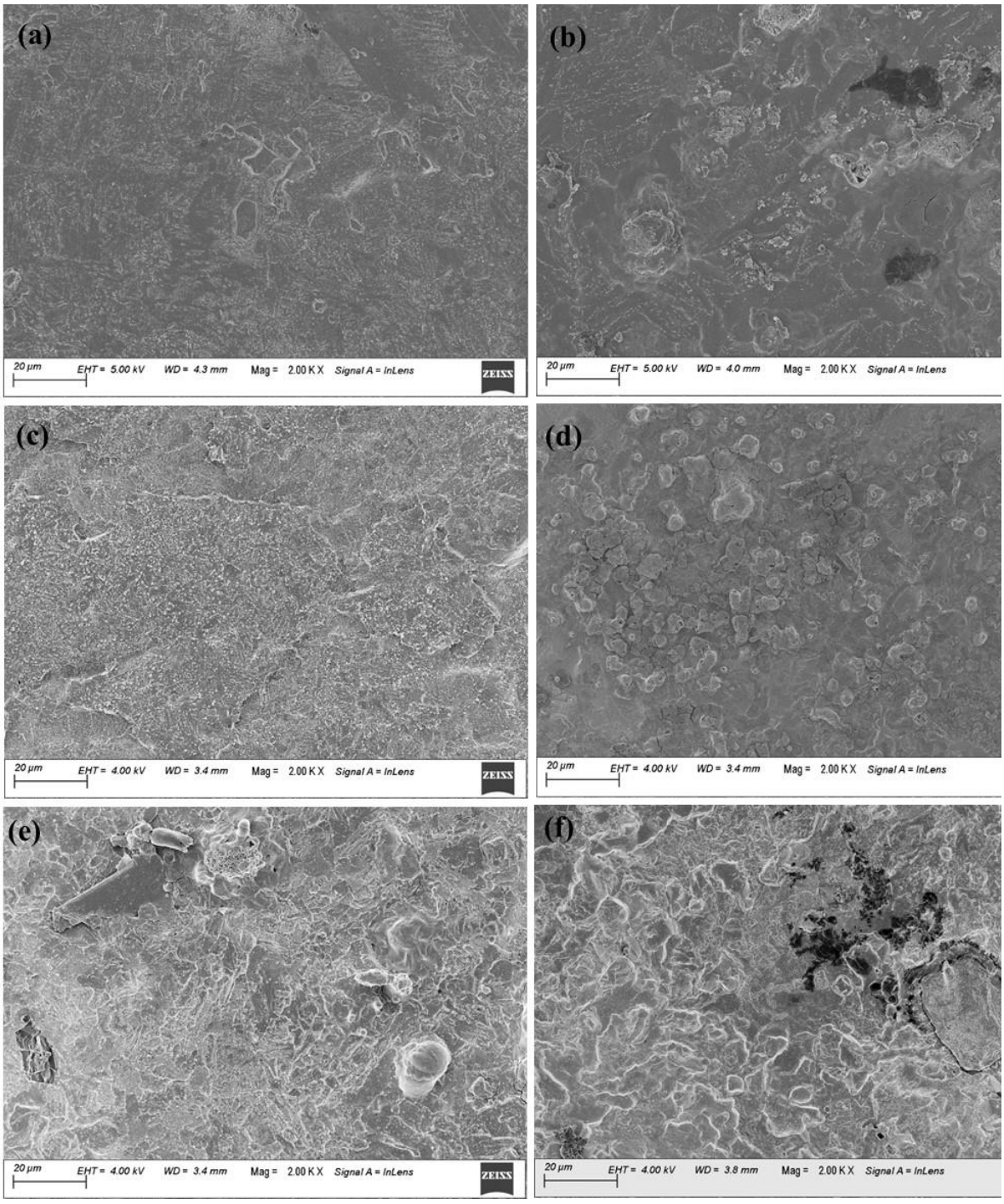

Figure 7.7 FESEM analysis of carbon steel after exposure to various acetic acid concentration and H_2S-CO_2 in the presence of 3.5 wt. % NaCl (a), (c), (e) X52 at 0 ppm, 500 ppm, and 1000 ppm, respectively at 40 ^oC; (b), (d), (f) X60 at 0 ppm, 500 ppm, and 1000 ppm respectively at 40 ^oC

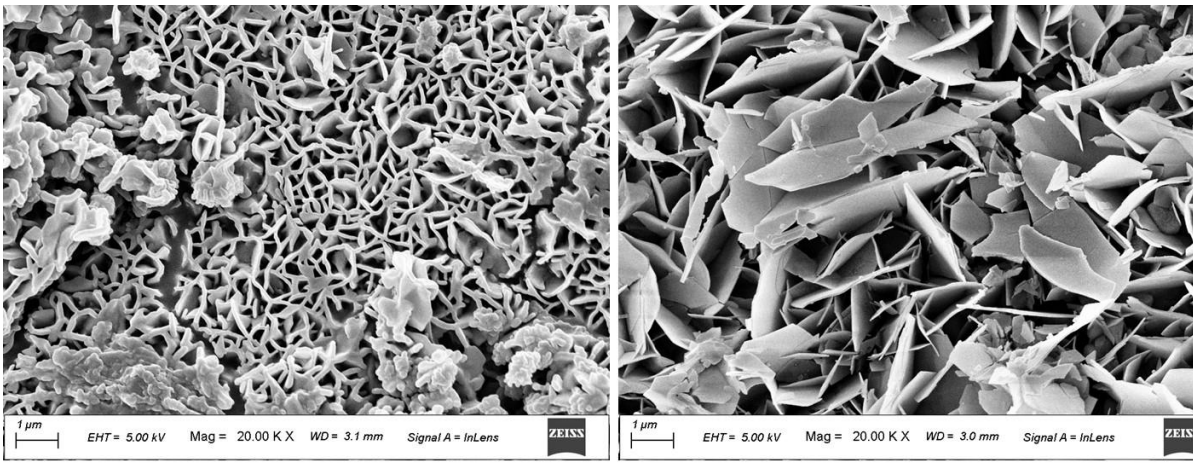

Figure 7.8 Morphology study of corrosion product in presence of 3.5 wt. % NaCl with CO_2-H_2S at 1000 ppm (a) X52 (b) X60 at 40 ^oC

Figure 7.8 (a-b) shows the corrosion product observed on the surfaces of both the steels when it is immersed in solution containing CO_2, H_2S and 1000 ppm acetic acid in 3.5 wt. % NaCl. The needle like fibrous structure observed in X52 featured chukanovite (iron carbonate) predominantly along with iron sulphide (Alam et al. 2016). However, in case of X60, flake like structure was observed expected to be mackinawite (FeS). For X60, iron sulphide was formed majorly along with iron carbonate [9,38]. Since mackinawite is a less stable form of FeS, hence, the corrosion product formed at the surface of X60 was not stable remarking higher corrosion rate observed in X60. Further it was observed that the corrosion product observed on the X52 surface is fine in nature whereas coarse in nature for X60 steel. These results clearly suggest that kinetics of carbon steel dissolution is significantly different for X52 and X60.

7.2.5. XPS Analysis

To understand the corrosion products formed, X-ray photo electron spectroscopy (XPS) analysis was performed for the corrosion products obtained from both the carbon steels (X52

and X60) exposed at 1000 ppm acetic acid concentration at 40 ^{o}C. The spectrum observed for X52 is shown in Figure 7.9and X60 is shown in Figure 7.11. The Gaussian model was implemented for peak fitting. The deconvoluted peaks for C show 2 major peaks at binding energy (BE) 285 eV (I) and 287 eV (II) (Figure 7.10 (a), 7.12 (a)). The peak I is for adventitious carbonaceous species (Wang et al. 2023b), whereas the peak II is attributed to iron carbonate (López et al. 2003). Figure 7.10 (b) and Figure 7.12 (b) show deconvoluted peaks for Fe 2p3/2. The peaks observed at 711 eV (I) and 712 eV (II) indicate $FeCO_3$ and Fe_2O_3, respectively. The peaks at 726 eV (III) and 732eV (IV) are attributed to the presence of FeS and Fe^{3+}, respectively. The O1S XPS spectra for carbon steel X52 are shown in Figure 7.10 (c) and Figure 7.12 (c). The deconvoluted peak at binding energy 530 eV (I), is the one that corresponds to the hydroxyl group resulting from chemisorption of water or oxygen. Hence this explains the presence of Fe_2O_3 and the one at 532.5 (II) indicates SO_4^{2-}. The deconvolution of S2p1/2, as shown in Figure 7.10 (d) and Figure 7.12 (d), gives 3 major peaks at 167 eV (I), 168 eV (II) and 170 eV (III) associated with S^{2-}, R-SH and SO_4^{2-} respectively. The presence of a sulfate group in the corrosion product is due to the usage of sodium thiosulphate in the electrolyte solution. A similar observation is also reported in the literature (Zhang et al. 2022). The atomic percentage as shown in Table 7.3, confirms more amount of C and Fe in X52 corrosion product compared to that of X60 while the sulphur content was found to be more in X60 corrosion product. The carbonate to sulphide ratio (C1S / S2P) is more for X52 compared to that of X60 and this confirms that more FeS was formed on CS surface.

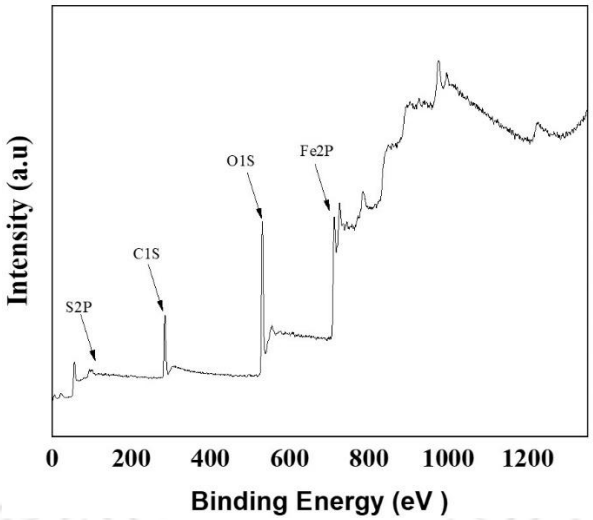

Figure 7.9 XPS analysis of carbon steel X52 at 40 °C and in solution containing CO_2, H_2S and 1000 ppm acetic acid concentration in the presence of 3.5 wt. % NaCl (a) C (b) Fe (c) O and (d) S

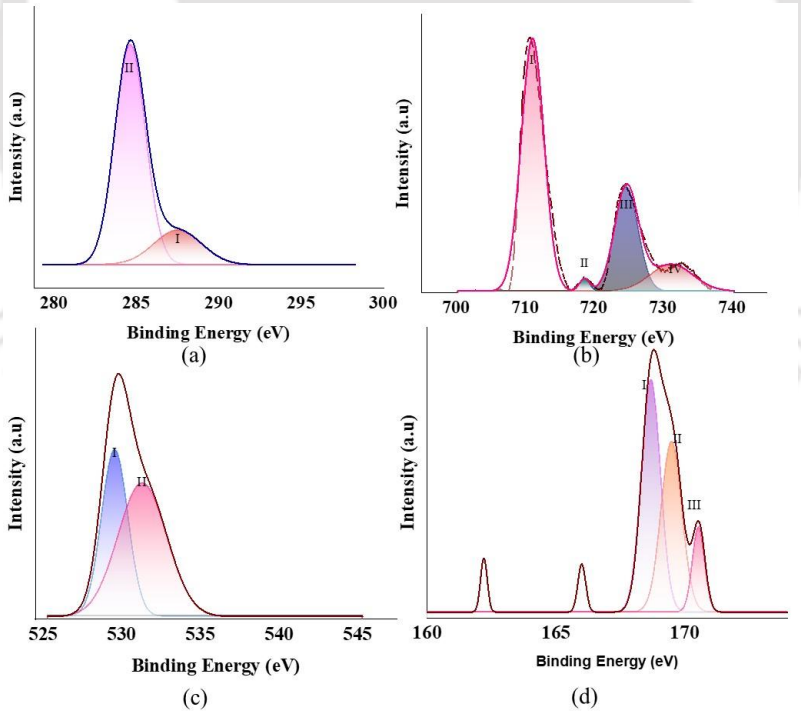

Figure 7.10 XPS analysis of carbon steel X52 at 40°C and in solution containing CO_2, H_2S and 1000 ppm acetic acid concentration in the presence of 3.5 wt. % NaCl (a) C (b) Fe (c) O and (d) S

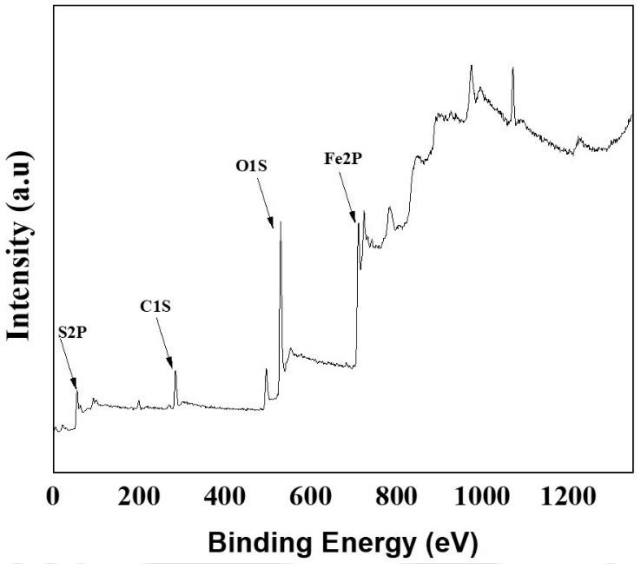

Figure 7.11 XPS analysis of carbon steel X60 at 40 ^{o}C and in solution containing CO_2, H_2S and 1000 ppm acetic acid concentration in the presence of 3.5 wt. % NaCl (a) C (b) Fe (c) O and (d) S

Table7.3 Atomic percentage of O, Fe, C, S obtained from XPS analysis

Carbon Steel	O1S	Fe2P	C1S	S2P
X52	41.29	14.41	43.48	0.25
X60	45.21	17.28	27.09	0.29

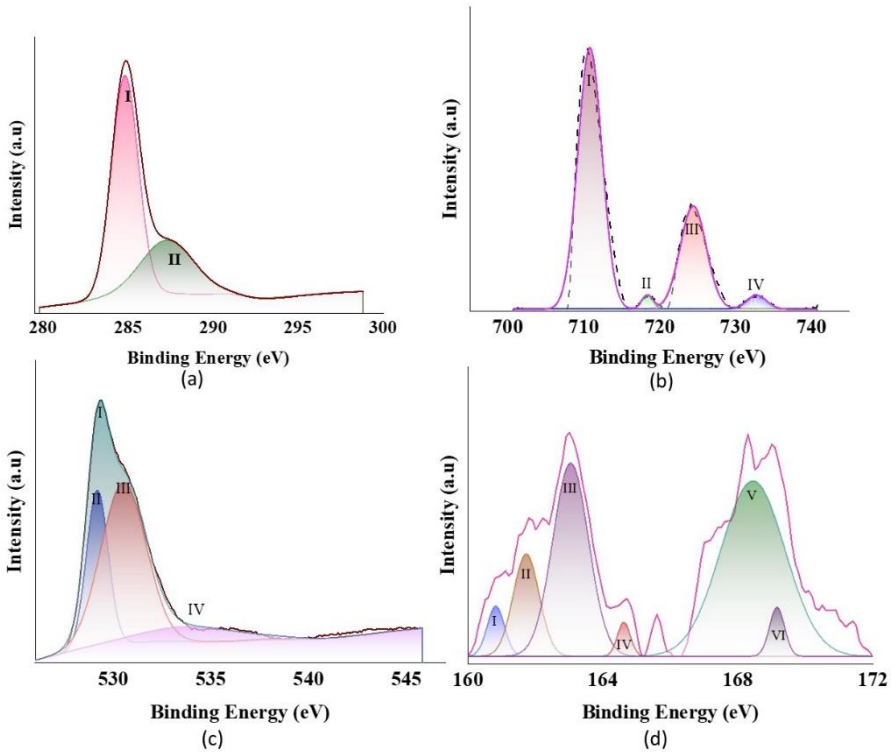

Figure 7.12 XPS analysis of carbon steel X60 at 40 ºC and in solution containing CO_2, H_2S and 1000 ppm acetic acid concentration in the presence of 3.5 wt. % NaCl (a) C (b) Fe (c) O
and (d) S

7.2.6. Contact Angle Study

The surface wettability of the carbon steels (X52 and X60) with the corrosive liquid was determined by measuring the contact angle as shown in Figure 7.13. The contact angle was measured at varying acetic acid concentrations (0, 500, and 1000 ppm) in the CO_2- H_2S at 3.5 wt. % NaCl solution.

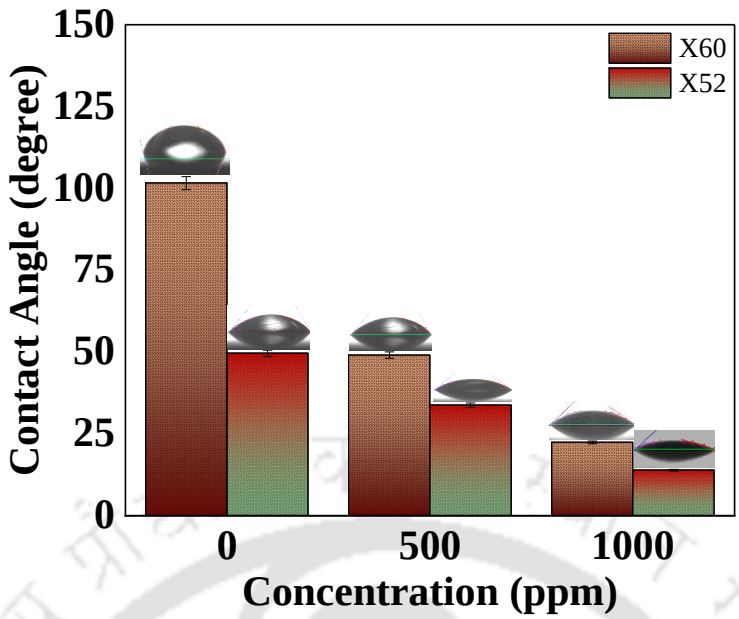

Figure 7.13 Contact angle measurements for X52 and X60 in 0 ppm and 1000 ppm acetic acid in the presence of CO_2-H_2S and 3.5 wt. % NaCl solution

In the absence of acetic acid, the contact angle of X60 was high (109.1°) owing to hydrophobicity (Singh et al. 2020). The decreasing trend of contact angle was witnessed with the increase in acetic acid concentration for X52 and X60. Still, the surface of X52 was observed to be more hydrophilic in nature, possessing higher surface energy (Behera et al. 2019) at all the investigated concentrations.

7.2.7. Reaction Mechanism Analysis

In order to investigate and compare the dissolution kinetics of carbon steels (X52 and X60), the EIS experiments were performed at various overpotentials (0.05 V, 0.15 V and 0.25 V) for both the steels in CO_2- H_2S solutions in the absence (0 ppm) and presence of (1000 ppm) acetic acid. The results obtained are shown in Figures 7.14 – 7.17. The obtained complex plane plots, as illustrated in the figures, show 3-time constants depicting a capacitance-inductance loop followed by a pseudo-capacitance loop. The RMA is used to retrieve the kinetic information from the impedance data. As observed from the Nyquist plots, the total impedance decreases with an increase in overpotential. Also, the overall impedance at corresponding overpotentials

is high for 0 ppm compared to 1000 ppm. Hence, the corrosion rate is explained to increase with the ascending overpotential and with an increase in acetic acid concentration.

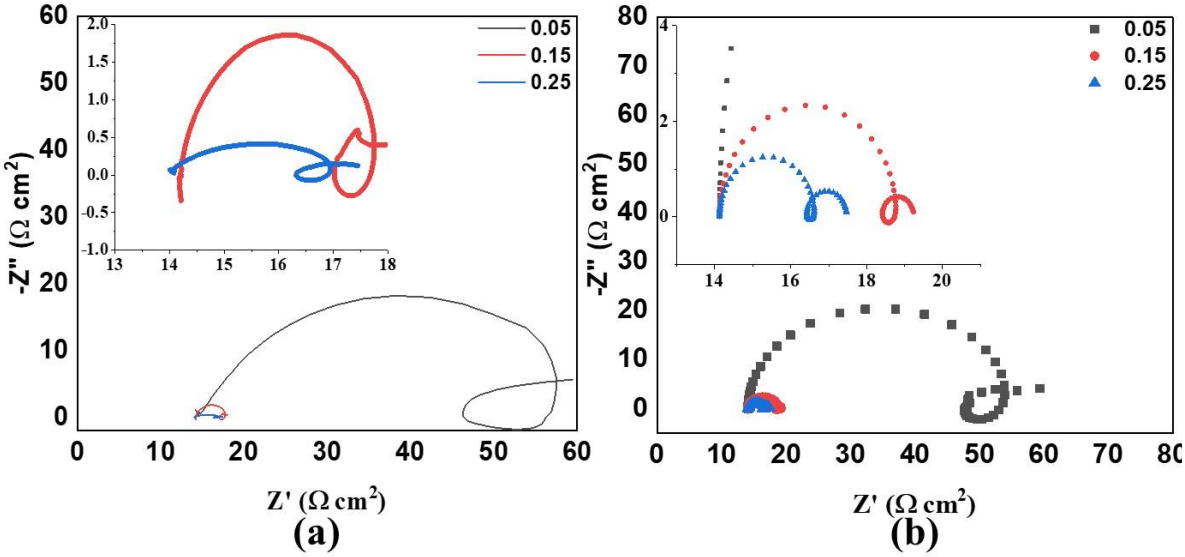

Figure 7.14 EIS measurement at overpotentials (0.05 V, 0.15 V, and 0.25 V) in presence of 3.5 wt. % NaCl with CO_2-H_2S and 0 PPM acetic acid for X52 at 40 °C (a) experimental (b) simulated

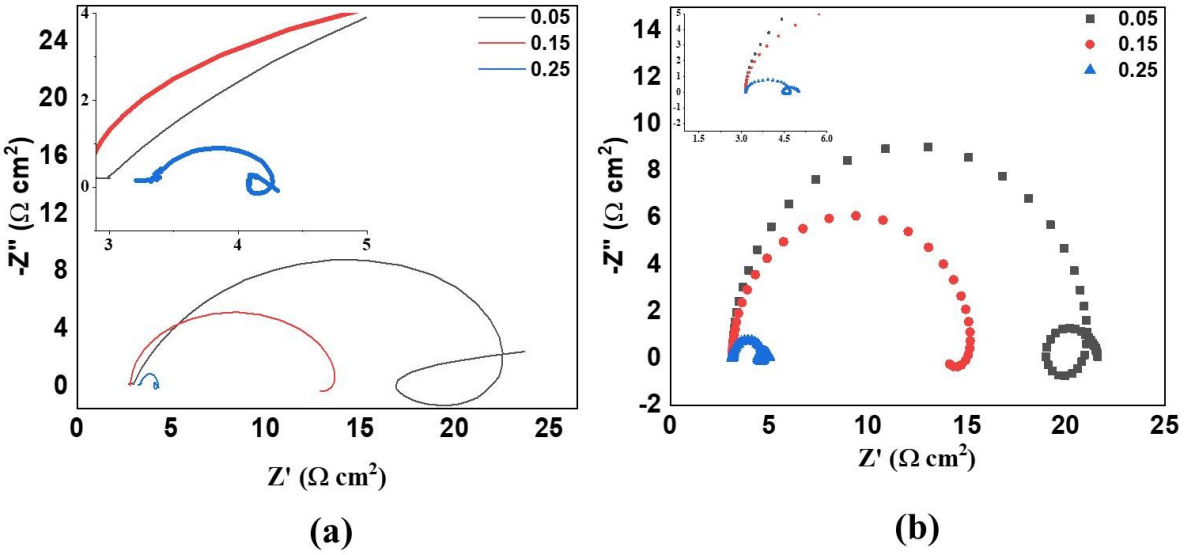

Figure 7.15 EIS measurement at overpotentials (0.05 V, 0.15 V, and 0.25 V) in presence of 3.5 wt. % NaCl with CO_2-H_2S and 0 PPM acetic acid for X60 at 40°C (a) experimental (b) simulated

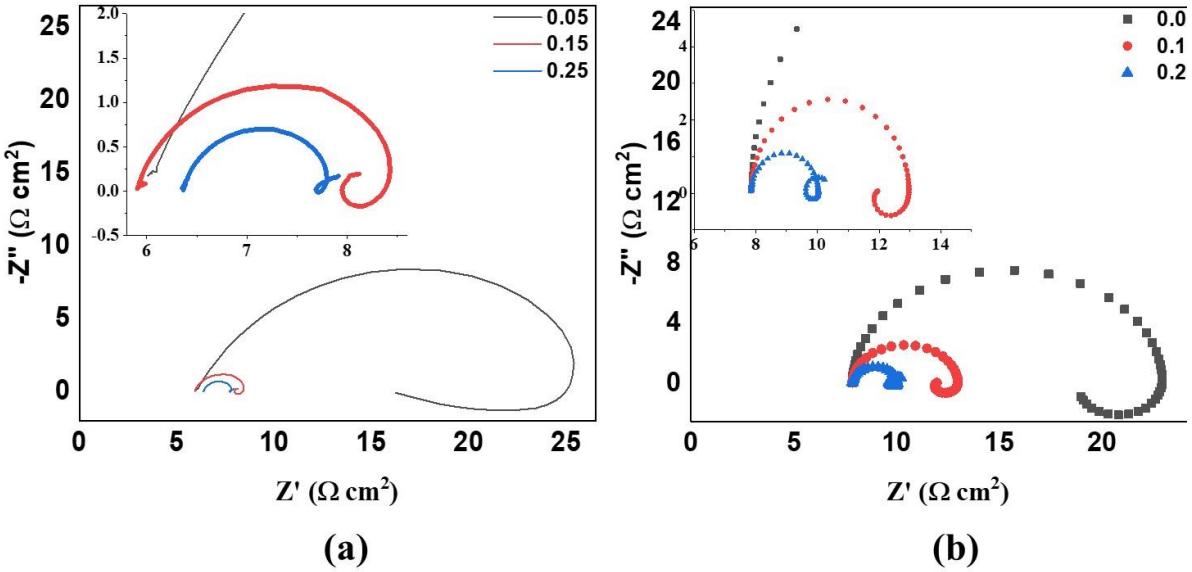

Figure 7.16 EIS Measurement at overpotentials (0.05 V, 0.15 V, and 0.25 V) in the presence of 3.5 wt. % NaCl with CO_2-H_2S and 1000 PPM acetic acid for X52 at 40 °C (a) Experimental (b) Simulated

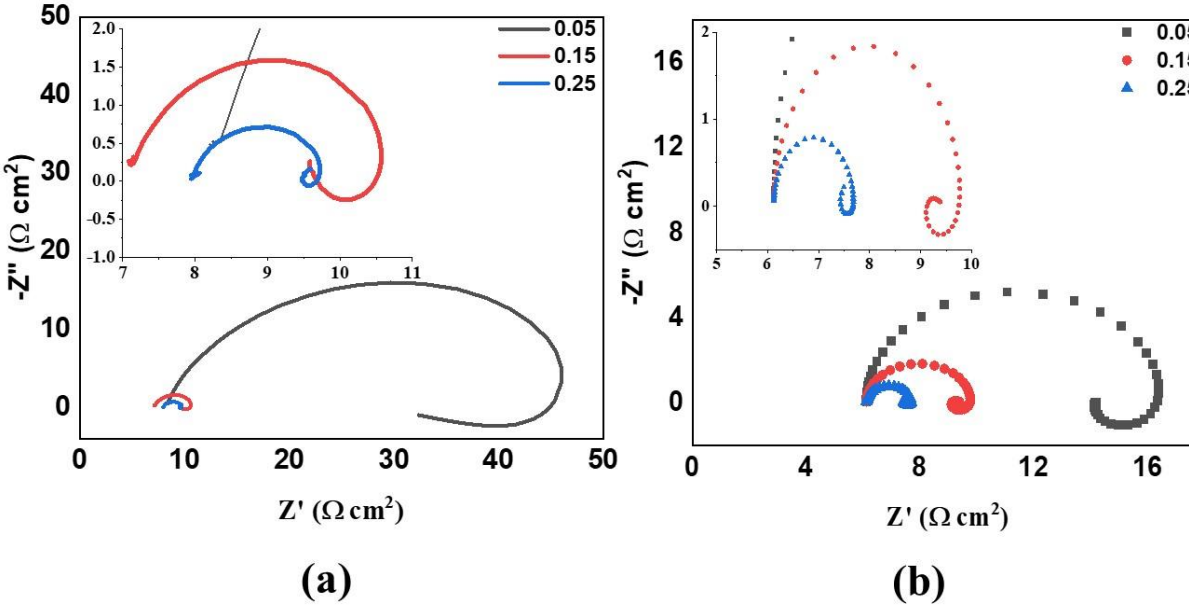

Figure 7.17 EIS Measurement at overpotentials (0.05 V, 0.15 V, and 0.25 V) in the presence of 3.5 wt. % NaCl with CO_2-H_2S and 1000 PPM acetic acid for X60 at 40 °C (a) Experimental (b) Simulated

Since three-time constants were observed in the impedance spectra, a mechanism with at least two intermediate adsorbed species needs to be considered to simulate the impedance data.

However, in the present case, as the system has both CO_2 and H_2S, the following mechanism having six steps with four intermediate adsorbed species are considered as it explains the observed trend better. It is to be noted that the suggested mechanism has two chemical dissolution paths k_5 and k_6. Further, as the concentration of other metals such as Ni, Cr etc is very minimal in both X52 and X60, its impact on the corrosion reaction mechanism and rate is insignificant (Baranwal and Prasanna Venkatesh 2017). Hence, we considered only Fe in the reaction mechanism analysis.

$$Fe \xrightarrow{k_1} Fe^{+}_{ad_1} + e \xrightarrow{k_3} Fe^{2+}_{ad_3} \xrightarrow{k_5} Fe^{2+}_{sol} \quad \text{(Dissolution Step 1)} \qquad 7.3$$

$$Fe \xrightarrow{k_2} Fe^{+}_{ad_2} + e \xrightarrow{k_4} Fe^{2+}_{ad_4} \xrightarrow{k_6} Fe^{2+}_{sol} \quad \text{(Dissolution Step 2)} \qquad 7.4$$

Here, Fe^{+}_{ad1}, Fe^{+}_{ad2}, Fe^{2+}_{ad3} and Fe^{2+}_{ad4} are the absorbed metal species considered. Where, Fe^{+}_{ad1} and Fe^{2+}_{ad3} corresponds to iron sulfides. while Fe^{+}_{ad2} and Fe^{2+}_{ad4} corresponds to iron carbonates and oxides. A similar mechanism is also proposed in the literature (Talukdar and Rajaraman 2020). Among other corrosion products of Fe, the solubility of ferrous acetate is higher. Hence, the acetate layer of Fe was not considered on the carbon surface. FESEM and XPS analysis also confirmed the absence of ferrous acetate in the corrosion product. Fe^{2+}_{sol} represents the metal ion dissolved in the solution. Taking account of the reversible reactions, it did not improve our simulation results significantly; hence, only the forward reactions are considered. The following assumptions were made to develop the impedance equations (a) a small amplitude of 10 mv (rms) linear perturbation was applied using ac voltage signal; (b) Langmuir adsorption isotherm model was employed and hence the surface coverage of adsorption of the charged species was assumed to be unity; (c) the kinetic parameters were proportional exponentially to the voltage. The current density for the proposed reaction mechanism at an unsteady state is expressed as a Butler-Volmer type reaction where the individual reaction rate

at an elementary electrochemical step, i, is termed as $k_i = k_{i0}e^{b_i v}$. The k_{i0} is the reaction rate at open circuit potential. Both the dissolution paths (k_5, and k_6) are chemical in nature and hence their values are independent of potential.

The total current density due to the reaction steps (k_1, k_2, k_3, k_4, k_5, and k_6) is as follows

$$J = nF\left[k_1\left(1-\theta_1-\theta_2-\theta_3-\theta_4\right)+k_3\theta_1+k_2\left(1-\theta_1-\theta_2-\theta_3-\theta_4\right)-k_4\theta_2\right] \quad 7.5$$

Under steady state conditions, the current density will be expressed as

$$J_{ss} = nF\left[2\left(k_5\theta_{3ss}+k_6\theta_{4ss}\right)\right] \quad 7.6$$

The unsteady state mass balance due to the adsorbed species θ_1, θ_2, θ_3 and θ_4 are given as,

$$\tau\frac{\mathrm{d}\theta_1}{\mathrm{d}t} = k_1\left(1-\theta_1-\theta_2-\theta_3-\theta_4\right)-k_3\theta_1 \quad 7.7$$

$$\tau\frac{\mathrm{d}\theta_2}{\mathrm{d}t} = k_2\left(1-\theta_1-\theta_2-\theta_3-\theta_4\right)-k_4\theta_2 \quad 7.8$$

$$\tau\frac{\mathrm{d}\theta_3}{\mathrm{d}t} = k_3\theta_1+k_5\theta_3 \quad 7.9$$

$$\tau\frac{\mathrm{d}\theta_4}{\mathrm{d}t} = k_4\theta_2+k_6\theta_4 \quad 7.10$$

Where, τ is the active sites available for dissolution per unit area of carbon steel; θ_1, θ_2 θ_3 and θ_4 indicates the surface coverage of Fe^{+}_{ad1}, Fe^{+}_{ad2}, Fe^{+}_{ad3} and Fe^{+}_{ad4} species respectively; $(1-\theta_1-\theta_2-\theta_3-\theta_4)$ indicates the unoccupied site.

At steady state conditions, $\tau\frac{d\theta_1}{dt}, \tau\frac{d\theta_2}{dt}$, $\tau\frac{d\theta_3}{dt}$ and $\tau\frac{d\theta_4}{dt}$ will be equal to 0. The fractional surface coverage at steady state after simplification can be expressed as,

$$\theta_{1ss} = \frac{\varepsilon + \eta\gamma}{(1-\eta\delta)} \quad 7.11$$

$$\theta_{2ss} = \gamma + \delta\theta_{1ss} \quad 7.12$$

$$\theta_{3ss} = \alpha\theta_{1ss} \quad 7.13$$

$$\theta_{4ss} = \beta(\gamma + \delta\theta_{1ss}) \quad 7.14$$

Where,

$$\alpha = \frac{k_3}{k_5} \quad 7.15$$

$$\beta = \frac{k_4}{k_6} \quad 7.16$$

$$\gamma = \frac{k_6}{k_4 + k_6} \quad 7.17$$

$$\delta = \frac{-[k_1 + k_1\alpha + k_3]}{k_1(1+\beta)} \quad 7.18$$

$$\varepsilon = \frac{1}{1+\alpha} \quad 7.19$$

$$\eta = \frac{-[k_2 + k_2\beta + k_4]}{k_2(1+\alpha)} \quad 7.20$$

The faradic impedance at the metal-electrolyte interface is found by differentiating the current density equation with respect to voltage, given as,

$$\frac{dJ}{dV} = (Z_{F,m/s})^{-1} = nF\left[\frac{d(k_1+k_2)}{dV}(1-\theta_{1ss}-\theta_{2ss}) - (k_1+k_2)\left(\frac{d\theta_1}{dV}+\frac{d\theta_2}{dV}\right) - \frac{dk_3}{dV}\theta_{1ss} - k_3\frac{d\theta_1}{dV} + \frac{dk_4}{dV}\theta_{2ss} + k_4\frac{d\theta_2}{dV}\right] \quad 7.21$$

On further rearrangement, the total impedance can be expressed as

$$(Z_{F,m/s})^{-1} = R_{ct}^{-1} - F\left[\frac{d\theta_1}{dV}(k_1+k_2-k_3) + \frac{d\theta_2}{dV}(k_1+k_2-k_4) + \frac{d\theta_3}{dV}(k_1+k_2) + \frac{d\theta_4}{dV}(k_1+k_2)\right]$$

7.22

Where, the charge transfer resistance is expressed as

$$R_{ct}^{-1} = F\left[(k_1b_1+k_2b_2)(1-\theta_{1ss}-\theta_{2ss}-\theta_{3ss}-\theta_{4ss}) - k_3b_3\theta_{1ss} + k_4b_4\theta_{2ss}\right] \quad 7.23$$

$\frac{d\theta_1}{dV}$, $\frac{d\theta_2}{dV}$, $\frac{d\theta_3}{dV}$ and $\frac{d\theta_4}{dV}$ are determined by applying Taylor's approximation and expanding the mass balance equations. The higher order terms appearing in the equation were neglected to avoid non-linearity in the system.

$$\frac{d\theta_1}{dV} = \frac{AB_2 - B_2B}{CB - B_2D} \quad 7.24$$

$$\frac{d\theta_2}{dV} = \frac{E - D\left(\frac{d\theta_1}{dV}\right)}{B2} \quad 7.25$$

$$\frac{d\theta_3}{dV} = \frac{E_3 - A_3\left(\frac{d\theta_1}{dV}\right)}{C_3} \quad 7.26$$

$$\frac{d\theta_4}{dV} = \frac{E_4 - B_4\left(\frac{d\theta_2}{dV}\right)}{D_4} \quad 7.27$$

Where, at $n=1$

$$A=C_1-\frac{B_1A_4B_3-A_3B_1B_4}{A_4A_3} \quad 7.28$$

$$B=C_2-\frac{A_2C_3}{A_3}-\frac{A_2B_4}{A_4} \quad 7.29$$

$$C=A_1-\frac{C_1A_3}{B_3} \quad 7.30$$

$$D=A_2-\frac{A_2A_3}{B_3} \quad 7.31$$

$$A_1=k_1+k_3+i\omega\tau \quad 7.32$$

$$B_1=k_1 \quad 7.33$$

$$C_1=k_1b_1(1-\theta_{1ss}-\theta_{2ss}-\theta_{3ss}-\theta_{4ss})-k_3b_3\theta_{1ss} \quad 7.34$$

$$A_2=k_2 \quad 7.35$$

$$B_2=k_2+k_4+i\omega\tau \quad 7.36$$

$$C_2=k_2b_2(1-\theta_{1ss}-\theta_{2ss}-\theta_{3ss}-\theta_{4ss})+k_4b_4\theta_{2ss} \quad 7.37$$

$$A_3=-k_3$$

$$B_3=i\omega\tau \quad 7.38$$

$$C_3=k_3b_3\theta_{1ss} \quad 7.39$$

$$A_4=k_6+i\omega\tau \quad 7.40$$

$$B_4 = k_4 b_4 \theta_{2ss} - k_6 b_6 \theta_{4ss} \quad 7.41$$

Eventually, the overall impedance of the system is ascertained by the following equation,

$$Z_{\text{total}} = R_{\text{sol}} + \frac{1}{\left(Z_{\text{F,m/s}}\right)^{-1} + Y_0 (j\omega)^{n_1}} \quad 7.42$$

Where, R_{sol} is the solution resistance; Y_0 and n_1 are the CPE parameters; j equals to $\sqrt{-1}$ and represents angular frequency, which is related to frequency as $\omega = 2\pi f$. The best-fit parameters obtained from RMA simulation are shown in Tables 7.4-7.5, and the simulated impedance patterns from RMA are shown in Figures 7.14-7.17. In spite of having quantitative differences in the impedance values between the experimental and the simulated data, the patterns from the experimental data were well captured by the proposed model. The decrease in impedance with increasing overpotential values and the decrease in impedance with increasing acetic acid concentration at corresponding overpotentials were expressed well by the model. Besides, the number of time constants and their nature (whether capacitive/inductive loop) are captured by the suggested mechanism. The quantitative difference is relatively higher at 0.05 V than at higher overpotentials. The possible reason could be, only considering the anodic dissolution steps and at lower overpotentials, cathodic steps are also relatively predominant compared to those at higher overpotentials. From RMA parameters, it is found that (i) τ value is higher for X52 at both the 0 ppm and 1000 ppm acetic acid conditions, (ii) the rate of dissolution at step 1 is higher compared to dissolution at step 2 for both the steels at 0 ppm and 1000 ppm, and (iii) at the dissolution path 2, the k_6 is higher for X60 at both acetic acid concentrations.

Table 7.4 RMA parameters for 0 ppm acetic acid solution with CO_2-H_2S in the presence of 3.5 wt. % NaCl at 40 °C

Parameters	X52	X60	Units
$\mathbf{R_{sol}}$	18	4	Ω cm^2
k1	4×10^{-08}	8×10^{-08}	mol s^{-1} cm^{-2}
b1	7	7	V^{-1}
k2	2×10^{-12}	6×10^{-12}	mol s^{-1} cm^{-2}
b2	2	5	V^{-1}
k3	2×10^{-04}	6×10^{-04}	mol s^{-1} cm^{-2}
b3	6	5	V^{-1}
k4	2×10^{-07}	6×10^{-07}	mol s^{-1} cm^{-2}
b4	5	10	V^{-1}
k5	6×10^{-07}	9×10^{-07}	mol s^{-1} cm^{-2}
k6	2×10^{-09}	4×10^{-09}	mol s^{-1} cm^{-2}
$\mathbf{Yo}_{OCP+0.05}$	7.9×10^{-05}	2×10^{-06}	Ω^{-1} cm^{-2} s^n
$\mathbf{n1}_{OCP+0.05}$	0.92	0.93	
$\mathbf{Yo}_{OCP+0.15}$	8.9×10^{-05}	8.9×10^{-05}	Ω^{-1} cm^{-2} s^n
$\mathbf{n1}_{OCP+0.15}$	0.93	0.94	
$\mathbf{Yo}_{OCP+0.25}$	9.9×10^{-05}	9.9×10^{-05}	Ω^{-1} cm^{-2} s^n
$\mathbf{n1}_{OCP+0.25}$	0.95	0.96	
T	1×10^{-06}	4×10^{-07}	mol cm^{-2}

Table 7.5 RMA parameters for 1000 ppm acetic acid solution with CO_2-H_2S in the presence of 3.5 wt. % NaCl at 40 ℃

Parameters	X52	X60	Units
$\mathbf{R_{sol}}$	10	7.8	Ω cm^2
k1	2×10^{-08}	3×10^{-08}	mol s^{-1} cm^{-2}
b1	14	12	V^{-1}
k2	1×10^{-09}	1×10^{-09}	mol s^{-1} cm^{-2}
b2	8	8	V^{-1}
k3	1×10^{-06}	1×10^{-06}	mol s^{-1} cm^{-2}
b3	5	5	V^{-1}
k4	1×10^{-08}	1×10^{-08}	mol s^{-1} cm^{-2}
b4	9	9	V^{-1}
k5	1×10^{-06}	2×10^{-06}	mol s^{-1} cm^{-2}
k6	5×10^{-09}	5×10^{-08}	mol s^{-1} cm^{-2}
$\mathbf{Yo}_{OCP+0.05}$	7.9×10^{-05}	7.9×10^{-05}	$Ω^{-1}$ cm^{-2} s^n
$\mathbf{n1}_{OCP+0.05}$	0.9	0.91	
$\mathbf{Yo}_{OCP+0.15}$	8.9×10^{-05}	8.9×10^{-05}	$Ω^{-1}$ cm^{-2} s^n
$\mathbf{n1}_{OCP+0.15}$	0.91	0.92	
$\mathbf{Yo}_{OCP+0.25}$	9.9×10^{-05}	9.9×10^{-05}	$Ω^{-1}$ cm^{-2} s^n
$\mathbf{n1}_{OCP+0.25}$	0.94	0.95	
T	1×10^{-06}	1×10^{-07}	mol cm^{-2}

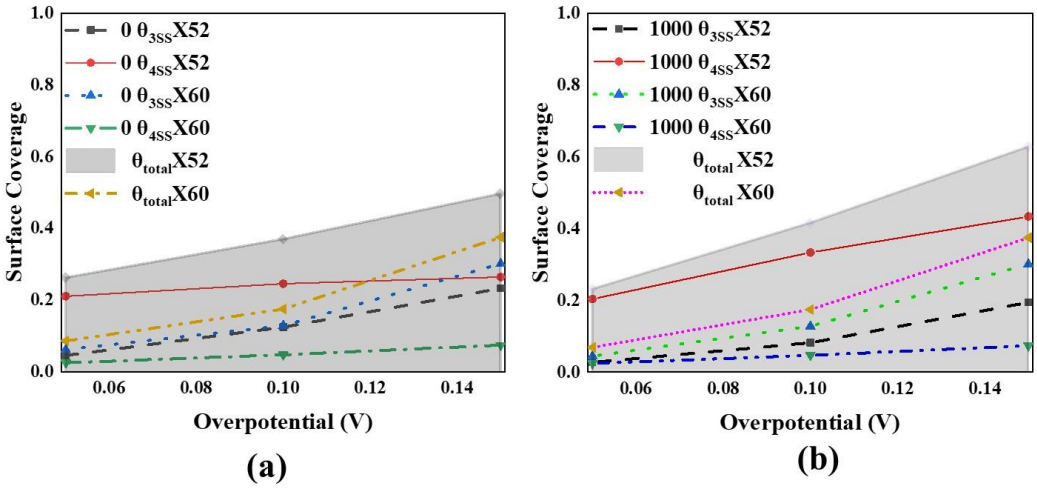

Figure 7.18 Surface coverage at acetic acid concentrations (0 ppm and 1000 ppm) in 3.5 wt. % NaCl in the presence of CO_2-H_2S at 40 °C for carbon steel (a) 0 ppm and (b) 1000 ppm

The surface coverage of adsorbed species (θ_{3ss}, θ_{4ss}, and θ_{total}) was calculated from the RMA analysis as shown in Figure 7.18. The θ_{3ss} and θ_{4ss} values increase with overpotential for both the steels. However, θ_{4ss} value is higher for X52 compared to that of X60 which is mainly due to the high k_6 value. The total surface coverage value is also higher for X52 than for X60. This is true for both the concentrations of acetic acid (0 and 1000 ppm). In summary, $FeCO_3$ covers the surface more than FeS for X52 and vice-versa for X60.

7.2.8. Suggested Mechanism for Carbon Steels (X52 and X60) Dissolution in CO_2-H_2S-Acetic Acid Solution

The total number of active/ nucleation sites are likely to be higher for X52 as predicted by RMA. Further, the contact angle is lower for X52 (more wetting of surface) compared to that of X60. Thus, the dissolution of Fe and eventually the formation of corrosion product on the X52 is very rapid. It leads to a greater number of corrosion product particles present on the carbon steel X52. Since, X60 is more hydrophobic, the surface wetting is less and also having

lower number of active sites. Thus, the surface is covered with lower number of corrosion product particles and coarse in nature. FESEM image also confirms that the corrosion product is fine for X52. Besides the rate of dissolution of $FeCO_3$ is less compared to FeS dissolution for both the steels (k_6 value is high compared to k_5) and the rate of formation of $FeCO_3$ is higher on X52 (due to high k_2, k_4 and low k_6 value for X52 at 0 ppm; low k_6 value for X52 at 1000 ppm). So, the X52 is covered with more $FeCO_3$ particles. XPS analysis also confirms that C/S ratio is more for X52.It is widely reported in the literature that $FeCO_3$ is more stable compared to FeS (Choi et al. 2011; Wei et al. 2016; Liu et al. 2017). Thus, the $FeCO_3$ layer on X52 gives more protection efficiency and eventually the corrosion rate is less for X52. The presence of acetic acid in CO_2-H_2S system increases the corrosion rate via increasing the cathodic reaction rate as observed by the polarization measurement. However, it does not alter the corrosion mechanistic reaction pathway as the similar behaviour is observed in cases: in the presence (1000 ppm) and absence (0 ppm) of acetic acid. The mechanism is shown in Figure 7.19.

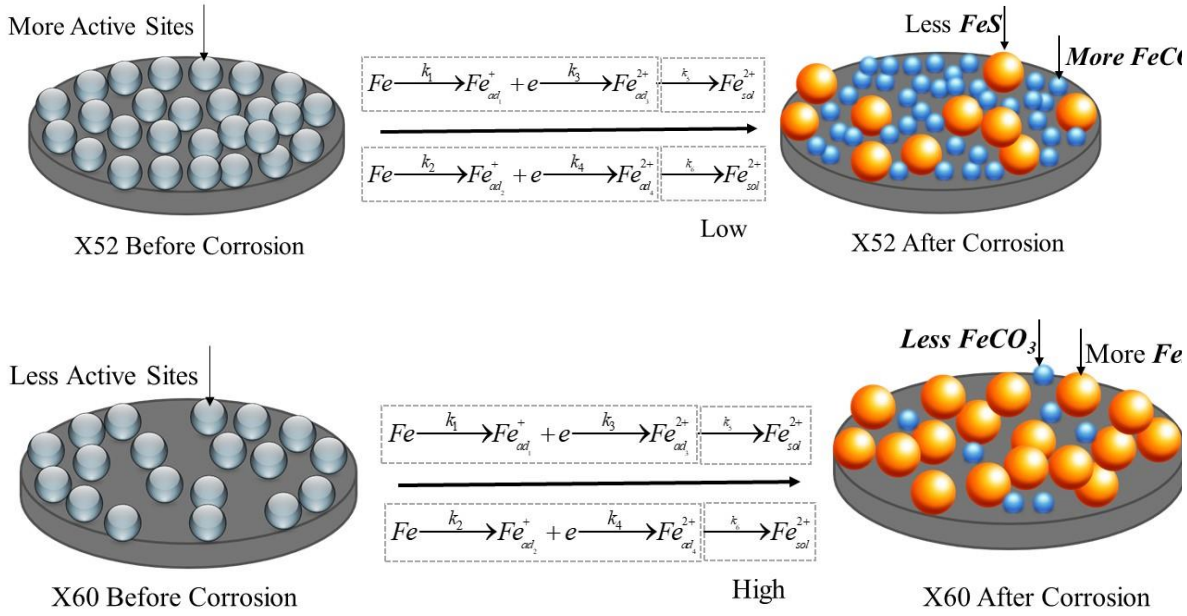

Figure 7.19 Schematic representation of the proposed corrosion mechanism when metal is exposed to a corrosion environment

CHAPTER 8

CHAPTER VIII: SUMMARY

8.1. SUMMARY OF THE PRESENT WORK

Corrosion is having an impact in almost all fields, including industries, our daily lives, and also the impact on the world economy; a lot of research is going on to control and mitigate corrosion. The corrosion behavior varies under different conditions and industries. Likely, the corrosion scenario is a bit different for semiconductor industries. In order to fabricate a well-organized planarized surface, the metal in IC chips is polished using the CMP process. The process involves oxidation of the metal surface using a suitable slurry and removal of the oxide layer using the physical process to achieve a desired polished surface. The slurry is mainly comprised of oxidizers, complexing agents, and abrasives. Hence, the design of a suitable slurry is necessary to achieve the desired surface. Thus, to prepare a suitable slurry, a study of the dissolution mechanism of the metal in the presence of oxidizers is necessary. Cu, Ta/TaN is being used for interconnect and barrier, which is being replaced by Mo due to its properties.

Some slurries are reported for the CMP of Mo metal, but a detailed explanation of the dissolution behavior has not been reported yet. Hence, the present work investigates the dissolution behavior of Mo in the presence of an oxidizer, H_2O_2, in an alkaline medium. It was also observed that in the presence of H_2O_2, a high etch rate is achieved, whereas in the presence of $KMnO_4$, the etch rate is significantly low, but the polish rate is considerably high. Hence, in the latter part of the work, we compared the dissolution behavior of Mo-H_2O_2 and Mo-$KMnO_4$ systems to analyze this contrasting behavior.

On the other hand, carbon steel corrosion is the most pertinent for the oil and gas industries because it is used as the material of construction in the majority of the processes. Carbon steel corrosion takes place due to the presence of gases, acids, chlorides, and sulfides, which are

mostly transported using pipelines over a large distance. However, to mitigate corrosion, it is very important to understand the factors affecting corrosion and the corrosion mechanism.

A considerable amount of work has been carried out on the corrosion behavior of various grades of carbon steel in several corrosive environments. The carbon steel grade varies due to the composition of the various alloying materials used, and the susceptibility towards corrosion of the carbon steel is decided based on its physical properties. Based on the physical factors, the carbon steel API 5L X60 should perform well in a corrosive environment compared to API 5L X52. However, some literature reported a higher corrosion rate of carbon steel X60. There is a lot of literature reported on the corrosion behavior of various grades of carbon steel in the presence of gases, and acids containing chlorides, sulfides, and volatile fatty acids. However, the synergistic effect of sulfides, carbon dioxide, and acetic acid is very limited. Also, there is only one study that reported the comparison of the corrosion behavior of X52 and X60 in the presence of CO_2 and acetic acid. However, there is no proper explanation of the corrosion mechanism. Hence, the present work is carried out systematically to investigate and compare the corrosion behavior of carbon steels X52 and X60 in the CO_2-H_2S-acetic acid system in the presence of NaCl at higher temperatures.

The first aim is the mechanistic investigation of anodic dissolution of molybdenum (Mo) in 2.5 wt. % hydrogen peroxide (H_2O_2) solution at pH 10 (Chapter 5). The etch rate (Figure 5.1) of Mo was observed to increase with increasing H_2O_2 concentration. It is evident from the OCP experiment shown in Figure 5.2 that the OCP value increases with increasing H_2O_2 concentration. This is mainly due to the formation of oxide species on the metal surface. The anodic polarization of Mo at various H_2O_2 concentrations (Figure 5.3) showed active dissolution at all concentrations. Also, the current density increased at respective overpotentials for all concentrations. The passivation was not observed in the potential regime being

investigated, as the constant current regime is not evident in these curves. The Eh-pH plot (Pourbaix plot) illustrated in Figure 5.4 revealed the stability of Mo in the H_2O system over a potential range with respect to pH. From the Eh-pH plot, Mo is observed to dissolve in the form of $HMoO_4^-$ and MoO_4^{2-} ions or get passivated in the form of MoO_3 and MoO_4 depending upon the pH value and equilibrium potential. Mo dissolves as MoO_4^{2-} (the oxidation state changes from 0 to +6) in the solutions containing H_2O_2. The oxidation and reduction potentials were determined via a cyclic voltammetry (CV) experiment, as shown in Figure 5.5. Two oxidation peaks were obtained at 0.05 V and 0.24 V in the forward scan. The reverse scan obtained two reduction peaks at 0.21 V and -0.05 V, however the second reduction peak was not prominent. Hence square wave voltammetry experiment was performed where the reduction peaks were captured well (Figure 5.6). The FESEM images (Figure 5.7) of the metal surface revealed uniform corrosion in the H_2O_2 system. There was no corrosion observed in the blank metal surface. The FESEM image of the corrosion product (Figure 5.8) resembled Mo (VI) as compared to the reported literature. XPS (Figure 5.9) confirmed the presence of Mo (IV) and Mo (VI). There were no other oxides of Mo found, since the $HMoO_4^{2-}$ is soluble and could not be collected as a corrosion product. EIS experiments were performed to further predict the dissolution mechanism of Mo in H_2O_2 solution. The EIS experiments were performed at higher overpotentials, 0.1V, 0.2 V, and 0.3 V, as shown in Figure 5.11. The overall impedance was observed to decrease with increasing overpotentials, indicating an increase in the dissolution rate of Mo. At all three overpotentials, the Nyquist plot obtained showed a capacitive loop at a higher frequency followed by a pseudo-capacitive loop at a lower frequency. The EIS data was analyzed using EEC circuit fitting using the circuit represented in Figure 5.12. From the EEC parameters produced in Table 5.1, the charge transfer resistance decreased with increasing overpotential, whereas the constant phase element was increased. The EIS data was further analyzed using RMA to get more detailed information on the dissolution behavior of Mo. A

five-step reaction mechanism was proposed with three intermediates. A mathematical model was formulated to calculate impedance based on the proposed mechanism and the parameters were obtained by optimization using sequential quadratic programming in MATLAB. The RMA model was validated with the EIS experimental data, as shown in Figure 5.19, and the anodic polarization data (Figure 5.20). The best-fit parameters are produced in Table 5.2. Also, the steady state surface coverage values and dissolution rates were obtained from the RMA analysis as shown in Figure 5.22. The surface coverage was increased with an increase in overpotential from 60 % to 95 %, and the majority was [Mo (VI)]; the presence of Mo (IV) and Mo (II) was negligible. Also, it was observed that the dissolution via the electrochemical step was predominant compared to the chemical step. Based on all the results obtained, a dissolution mechanism was proposed as shown in Figure 5.23 and Figure 5.24.

The third aim focuses on the dissolution behavior of Mo in the presence of $KMnO_4$ solution under alkaline conditions (Chapter 6). It also compares the dissolution behavior with the H_2O_2 solution, as reported in Chapter 5. The etch rate and polish rate study shows a low etch rate and a very high polish rate (Figure 6.1). The etch rate of Mo in $KMnO_4$ is lower than the etch rate of Mo in H_2O_2. However, the polish rate is significantly high. The FESEM analysis resembled Mo (IV) and Mo (VI) with the literature, as shown in Figure 6.2. Further XPS analysis was performed, and the peaks obtained confirmed the presence of oxides of Mo, Mo (IV), and Mo (VI) (Figure 6.3). The potentiodynamic polarization showed active dissolution behavior, as shown in Figure 6.5. However, at lower overpotential (till 0.2 V), the rate of increase in current density with respect to potential was slightly low, as observed in the plot. A drastic increase in the current density was observed with a steeper slope at a higher potential (after 0.3 V). There was no sign of passivation. Comparatively, in the case of Mo dissolution in the presence of H_2O_2, the rate of increase in current density was almost uniform from low to higher potential. To understand the dissolution mechanism, EIS measurement was performed for Mo in $KMnO_4$

solution at higher overpotentials, 0.1 V, 0.2 V, and 0.3 V. The Nyquist plots (Figure 6.6 - 6.8) obtained showed a capacitive loop at a higher frequency, followed by Warburg impedance at a lower frequency, indicating diffusion behavior. The EEC fitting of the impedance data showed a decrease in charge transfer resistance and Warburg impedance, indicating an increase in dissolution rate. Also, with an increase in overpotential, the charge transfer resistance increased. The EIS data were further analyzed using RMA. The reaction mechanism proposed in Chapter 5 is used for the $KMnO_4$ system to compare the behavior of Mo dissolution using the same mechanism. The RMA data validation is shown in Figure 6.10. The RMA simulated plot was found to match the pattern of the experimental data plot. However, there was a quantitative difference in the impedance values at lower frequencies. This is because the reaction pathway proposed could not predict the diffusion behavior. Also, the surface coverage decreased with increasing overpotential, though the difference is marginal. This corresponds with the anodic dissolution behavior of Mo in the presence of H_2O_2 (Figure 5.3). From all the experimental and RMA observations, it can be concluded that the oxide formation for Mo is rapid (significantly high dissolution rate) in the presence of KMnO4, and the oxide layer covers the metal surface, which hinders the contact of the metal with the oxidizer. However, when the oxide layer is removed due to external force (higher overpotential or physical action), the dissolution of Mo is very rapid, resulting in a high polish rate value.

The final objective of the present work is to compare the corrosion behavior of carbon steels API 5L X52 and X60 in the simulated solution containing CO_2-H_2S-acetic acid in the presence of 3.5 wt. % NaCl (Chapter 7). The corrosion rate was measured via the immersion test method (Figure 7.1), and an increase in corrosion rate was observed with an increase in acetic acid concentration. Also, the corrosion rate for X60 was higher than that of X52. The potentiodynamic polarization plots, as shown in Figure 7.2 and Figure 7.3, showed an increase in the cathodic current with an increase in acetic acid concentration. A similar trend was

observed for all concentrations. No significant change was observed in the anodic current under all conditions. Thus, the increase in corrosion rate with respect to acetic acid concentration is mainly due to the increase in cathodic reaction rate. From the corrosion current (I_{corr}) and potential (E_{corr}) values obtained from Tafel fit parameters (Table 7.1), the increase in corrosion rate was evident with an increase in acetic acid concentration. An increase in both E_{corr} and I_{corr} values clearly suggests that acetic acid strongly influences the cathodic reaction rates for both steel samples as per mixed potential theory. The EIS measurement was performed to understand the corrosion kinetics in the system mentioned earlier (Figures 7.4-7.5). The total impedance was observed to decrease with an increase in acetic acid concentration, which explains the increase in corrosion rate as was observed in the immersion test and potentiodynamic polarization experiments. The Nyquist plots obtained when further analyzed, three loops were observed for both the steels, however, with a different trend. In the case of X52, a capacitive loop followed by an inductive loop was observed in the high to mid-frequency range, whereas, towards low frequency, a third pseudo-capacitive loop was observed. For X60, in lower acetic acid concentrations, a capacitive loop was observed at a higher frequency, followed by an inductive loop towards mid-frequency, and another capacitive loop at a lower frequency. Whereas, at high acetic acid concentration (1000 ppm), three capacitive loops were observed. Quantitative analysis of the EIS data was performed with EEC fitting. The charge transfer decreased with increasing acetic acid concentration, indicating an increase in corrosion rate. The microstructure analysis of the carbon steels revealed more ferrite content for X52 and less ferrite content for X60. Further, the FESEM images revealed increased corrosion behavior towards increasing acetic acid concentration (Figures 7.6-7.8). The contact angle study revealed a more hydrophobic surface for X60. X52, being more hydrophilic towards the system, has a greater number of nucleation sites. XPS study confirms similar corrosion products for both the steels; however, the fraction of S was higher for X60,

and C was higher for X52 (Figures 7.9-7.12). This explains that the formation of FeS is predominant for X60, and the presence of $FeCO_3$ in the corrosion product of X52 is prevalent. Further, the corrosion reaction mechanism was proposed, and a mathematical model for calculating the impedance was formulated for EIS data at higher overpotentials (0.05, 0.15, and 0.25 V) for 0 and 1000 ppm acetic acid concentrations (Figures 7.14-7.17). Three-time constants were observed in the Nyquist plot, and a six-step reaction mechanism was proposed with 4 intermediate adsorbates and two dissolution paths, k_5 and k_6. The parameters were optimized using sequential quadratic programming using MATLAB. From the RMA parameters, the active sites available for dissolution per unit area of carbon steel (τ) obtained was higher for X52 in the absence and presence of acetic acid. This agrees with the contact angle study. Also, the surface coverage was found to be higher for X52 compared to X60 for both acetic acid concentrations. Hence, it can be concluded that for X52, the surface is mainly covered with $FeCO_3$, whereas for X60, the surface coverage is mainly by FeS. Also, since $FeCO_3$ is forming in a rapid way and is fine in nature, the carbon steel surface is more protected from corrosion for X52. Hence, the corrosion rate of X60 is higher than that of X52.

Chapter IX: Conclusions and Future Recommendations

The principal findings of this research work are presented hereafter.

9.1. Conclusion on Chapter 5: The anodic dissolution of Mo in the presence of hydrogen peroxide at an alkaline pH.

a) The etch rate experiment revealed an increase in the etch rate with an increase in H_2O_2 concentration at pH 10. Active dissolution was observed in anodic potentiodynamic polarization experiments across all H_2O_2 concentrations.

b) The EIS data were analyzed, and a mechanistic reaction pathway was proposed. The suggested mechanism qualitatively predicted both the impedance and polarization behavior for Mo in the H_2O_2 solution. The kinetic parameters were also retrieved.

c) Through the RMA analysis, the dissolution rates of both electrochemical and chemical pathways were calculated. Dissolution rate via the electrochemical route was found to be relatively higher, and it increased towards higher overpotential, while the dissolution rate via the chemical reaction was very low and remained almost constant with increasing overpotential.

d) It was also observed that at any respective overpotential, the surface was mostly occupied by Mo (VI) oxides, as confirmed by the XPS analysis.

9.2. Conclusion on Chapter 6: The anodic dissolution of Mo in the presence of potassium permanganate at an alkaline pH.

a) Low etch rate and high polish rate observed for Mo in $KMnO_4$ at pH 10.

b) In this case, active dissolution was observed in anodic potentiodynamic polarization at higher overpotentials. However, the change in current density with respect to increasing

potential was significantly low at low overpotentials. It is likely to be the reason for low etch rate.

c) The impedance data at low frequency clearly shows the diffusion resistance offered by oxides on Mo surface which is not likely the case in H_2O_2 solution.

d) RMA analysis suggests a high dissolution rate via the electrochemical step. Though the dissolution rate is high, due to the presence of Mo oxides on the surface, there is very little contact between the metal surface and the oxidizer. Hence, the etch rate was observed to be low, but during polishing, due to physical action, the oxide layer is removed, resulting in a high polish rate

Thus, analysis of EIS data at various overpotentials via the RMA approach helps us to suggest the dissolution mechanism, obtain the kinetic parameters, and compare both systems being studied. The plausible reason for the low etch rate and high polish rate observed for Mo in 2.5 wt. % $KMnO_4$ solution at pH 10 was also elucidated using this approach. We can, therefore, conclude that based on the above-mentioned experimental observations of the mechanistic behavior of Mo dissolution in alkaline H_2O_2 and $KMnO_4$ media, one can prepare an optimized slurry to be used in CMP applications, taking the dissolution mechanism into account, i.e., the dissolution of Mo in presence of both the oxidizers is predominant through electrochemical reaction pathway and majority of the corrosion product is Mo (VI). There is a contrast in the dissolution behavior of Mo in the presence of $KMnO_4$ in terms of etch rate and polish rate. The etch rate of Mo observed in the presence of $KMnO_4$ is less than that in H_2O_2; however, the polish rate of Mo in $KMnO_4$ is significantly higher. The surface coverage of Mo oxides in the H_2O_2 system follows an increasing trend from 60 % to 97 % as the overpotential increases. In the $KMnO_4$ system, the surface coverage decreases from higher to lower overpotential (99.7 % to 99.3 %), though the change is insignificant. From all the experimental as well as RMA observations, it can be concluded that the oxide formation for Mo is rapid (significantly high

dissolution rate) in the presence of $KMnO_4$, and the oxide layer covers the metal surface, which hinders the contact of the metal with the oxidizer. However, when the oxide layer is removed due to external force (higher overpotential or physical action), the dissolution of Mo is very rapid, resulting in a high polish rate value.

9.3. Conclusion on Chapter 7: The comparison of corrosion behavior of carbon steel API 5L X52 and X60 in CO_2-H_2S-acetic acid solutions in the presence of NaCl.

a) The weight loss study, as well as electrochemical studies, including potentiodynamic polarization and electrochemical impedance spectroscopy measurements, revealed an increase in corrosion rate of both grades of carbon steel with increasing acetic acid concentration. The corrosion rate of X60 was higher than that of X52 across all concentrations of acetic acid.

b) The FESEM analysis of the metal surface revealed a more corroded steel surface towards higher acetic acid concentrations, and the microstructure of both the steels revealed higher ferrite content for X52, producing a corrosion product which is fine in nature.

c) The X60 surface was observed to be more hydrophobic than X52, as observed from the contact angle study. The corrosion product formed for both the steels was the same as observed from XPS analysis; however, the S content was found to be higher for X60, and the C content was higher for X52. Hence, it confirms that the formation of FeS is predominant for X60 and $FeCO_3$ is predominant for X52.

d) Through the RMA analysis, it was found that the surface coverage for X52 is higher than that of X60. Hence, this confirmed that more nucleation sites for corrosion product formation were available for X52 than for X60. Also, since $FeCO_3$ forms more in X52 and is fine in nature, the corrosion product layer provides more corrosion protection for

the carbon steel, resulting in a lower corrosion rate for X52. Correspondingly, since FeS formation is more in X60 and due to its unstable nature, the corrosion protection due to the product layer is less, resulting in a higher corrosion rate.

In general, through the reaction mechanism analysis performed, one can get a vivid picture of the corrosion behavior of the two different carbon steel grades. This outcome will provide support in deciding on the choice of material for pipeline constructions or planning for corrosion mitigation strategies.

The above-mentioned research outcomes and conclusions have been made to substantiate our research hypotheses stated in Chapter 1.

9.4. SUGGESTIONS FOR FUTURE WORK

a) To investigate the reaction mechanism for Mo in the $KMnO_4$ system by including the diffusion behavior in the mathematical model.
b) To formulate the technoeconomic evaluation considering economics, safety considerations, environmental footprint, and efficiency of both H_2O_2 and $KMnO_4$ for the proper choice of oxidizer.
c) Understanding the nucleation and growth rate of $FeCO_3$ and FeS in the presence of CO_2-H_2S at any given conditions for carbon steel X52 and X60 can be considered for future studies, so as to control the corrosion rate via enhancing the formation of fine $FeCO_3$ particles on the carbon steel surface.
d) Performing Aspen model simulation of corrosion in an oil and gas industry scenario in the CO_2-H_2S-acetic acid system, considering carbon steels API 5L X52 and X60.

REFERENCES

Adelmann C, Wen LG, Peter AP, (2014) Alternative metals for advanced interconnects. IEEE Int Interconnect Technol Conf / Adv Met Conf 173–176. https://doi.org/10.1109/IITC.2014.6831863

Adhikari S, Dhongde NR, Talukdar MK, et al (2024) Investigation of Carbon Steels (API 5L X52 and API 5L X60) Dissolution CO_2–H_2S Solutions in the Presence of Acetic Acid: Mechanistic Reaction Pathway and Kinetics. Arab J Sci Eng 49:8363–8381. https://doi.org/10.1007/s13369-024-08812-1

Ahmed Z (2006) Principles of Corrosion Engineering and Corrosion Control. Elsevier, Amsterdam.

Akeer E, Brown B, Nesic S (2013) The Influence of Mild Steel Metallurgy on the Initiation of Localized CO_2 Corrosion in Flowing Conditions. NACE - Int Corros Conf Ser 1–16

Aksu S, Wang L, Doyle FM (2003) Effect of hydrogen peroxide on oxidation of copper in CMP slurries containing glycine. J Electrochem Soc 150:G718

Al-janabi YT (2020) An Overview of Corrosion in Oil and Gas Industry: Upstream, Midstream and Downstream Sectors. Corros Inhib Oil Gas Ind 1–39 https://doi.org/10.1002/9783527822140.ch1

Al-Mansour M, Alfantazi AM, El-boujdaini M (2009) Sulfide stress cracking resistance of API-X100 high strength low alloy steel. Mater Des 30:4088–4094. https://doi.org/10.1016/j.matdes.2009.05.025

Alam MT, Chan EWL, De Marco R (2016) Electrochemical and Surface Analysis Studies on the Carbon Dioxide Corrosion of X-65 Carbon Steel. Electroanalysis 28:2910–2921. https://doi.org/10.1002/elan.201600309

Alkalah C (2004) Chemical-Mechanical Planarization of Semiconductor Materials. Springer Berlin Heidelb.

Amrutha MS, Fasmin F, Ramanathan S (2017) Effect of HF Concentration on Anodic Dissolution of Titanium. J Electrochem Soc 164:H188–H197. https://doi.org/10.1149/2.0501704jes

Amrutha MS, Rao MT, Ramanathan S (2018) Mechanistic Analysis of Anodic Dissolution of Zr in Acidic Fluoride Media. J Electrochem Soc 165:C162–C170. https://doi.org/10.1149/2.0851803jes

Arne Dugstad (2006) Fundamental Aspects of CO_2 Metal Loss Corrosion Part1_Mechanism.pdf. Corros Nace Expo 06111

Askari M, Aliofkhazraei M, Ghaffari S, Hajizadeh A (2018) Film former corrosion inhibitors for oil and gas pipelines - A technical review. J Nat Gas Sci Eng 58:92–114. https://doi.org/10.1016/j.jngse.2018.07.025

Bai P, Zheng S, Chen C (2015) Electrochemical characteristics of the early corrosion stages of API X52 steel exposed to H_2S environments. Mater Chem Phys 149:295–301. https://doi.org/10.1016/j.matchemphys.2014.10.020

Baltrusaitis J, Mendoza-Sanchez B, Fernandez V (2015) Generalized molybdenum oxide surface chemical state XPS determination via informed amorphous sample model. Appl Surf Sci 326:151–161. https://doi.org/10.1016/j.apsusc.2014.11.077

Baranwal PK, Prasanna Venkatesh R (2017) Investigation of carbon steel anodic dissolution in ammonium chloride solutions using electrochemical impedance spectroscopy. J Solid State Electrochem 21:1373–1384. https://doi.org/10.1007/s10008-016-3497-8

Baranwal PK, Rajaraman PV (2019) Kinetics of carbon steel dissolution in ammonium chloride

solution containing sodium thiosulfate. Int J Chem Kinet 51:497–510. https://doi.org/10.1002/kin.21272

Basics of Electrochemical Impedance Spectroscopy. https://www.gamry.com/application-notes/EIS/basics-of-electrochemical-impedance-spectroscopy/. Accessed 24 Feb 2021

Bechet B, Epelboin I, Keddam M (1977) New data from impedance measurements concerning the anodic dissolution of iron in acidic sulphuric media. J Electroanal Chem 76:129–134. https://doi.org/10.1016/S0022-0728(77)80013-2

Behera SK, Kumar P A, Dogra N (2019) Effect of Microstructure on Contact Angle and Corrosion of Ductile Iron: Iron-Graphite Composite. Langmuir 35:16120–16129. https://doi.org/10.1021/acs.langmuir.9b02395

Bernard P, Valette S, Daveau S (2008) Nature and removal of the modified layer in Cu CMP with ferric nitrate as oxidizer. Tribol Int 41:416–424. https://doi.org/10.1016/j.triboint.2007.09.009

Bhaskaran R, Bhalla L, Rahman A (2014) An analysis of the updated cost of corrosion in India. Mater Perform 53:56–65

Boyle R (1675) The Mechanical Origine or Production of Corrosiveness and Corrosibility. Flesher, London.

Brondel D, Edwards R, Hayman A, Hill D, Mehta S, Semerad T (1994) Corrosion in the oil industry. Oilf Rev 4-18.

Caique D.A. Lima, Jo˜ao Victor Barbosa Moura, Alexandre de Castro Maciel, Cleˆanio Luz-Lima, Lanna I.M. Sinimbu, Jo˜ao F. Chaves, Jonatas D.S. Oliveira, Adnan R. Syed, Rubem L. Sommer, Anupama Ghosh, Carlos L.R. Fragoso, Marco Cre JFDFA (2023) Synthesis and magnetic characterization of iron-doped molybdenum trioxide (α-

MoO_3_xFe). Solid State Sci 145:107313. https://doi.org/https://doi.org/10.1016/j.solidstatesciences.2023.107313

Calan-Canche D, García-Hernández R, Dzib-Pérez L, et al (2019) Susceptibility to the Absorption of Atomic Hydrogen in API 5L X60 Steels with Unconventional Heat Treatment. Mater Sci 54:573–581. https://doi.org/10.1007/s11003-019-00220-3

Callister W D Jr., Rethwisch D G, Materials Science and Engineering (2020), John Wiley and Sons, USA.

Camacho B, Gloria A (2005) Nanostructured Molybdenum Chalcogenides : Synthesis , Structure and Catalytic Properties. 113

Carpio R, Farkas J, Jairath R (1995) Initial study on copper CMP slurry chemistries. Thin Solid Films 266:238–244

Choi YS, Nesic S, Ling S (2011) Effect of H_2S on the CO_2 corrosion of carbon steel in acidic solutions. Electrochim Acta 56:1752–1760. https://doi.org/10.1016/j.electacta.2010.08.049

Clover D, Kinsella B, Pejcic B, De Marco R (2005) The influence of microstructure on the corrosion rate of various carbon steels. J Appl Electrochem 35:139–149. https://doi.org/10.1007/s10800-004-6207-7

Coetsier CM, Testa F, Carretier E(2011) Static dissolution rate of tungsten film versus chemical adjustments of a reused slurry for chemical mechanical polishing. Appl Surf Sci 257:6163–6170. https://doi.org/10.1016/j.apsusc.2011.02.023

Cui H, Park J H, Park J G (2012) Study of Ruthenium Oxides Species on Ruthenium Chemical Mechanical Planarization Using Periodate-Based Slurry. J Electrochem Soc 159:H335–H341. https://doi.org/10.1149/2.103203jes

Cui ZD, Wu SL, Zhu SL, Yang XJ (2006) Study on corrosion properties of pipelines in simulated produced water saturated with supercritical CO_2. Appl Surf Sci 252:2368–2374. https://doi.org/10.1016/j.apsusc.2005.04.008

Dai C, Zhao T, Du C (2020) Effect of molybdenum content on the microstructure and corrosion behavior of FeCoCrNiMox high-entropy alloys. J Mater Sci Technol 46:64–73. https://doi.org/10.1016/j.jmst.2019.10.020

Das Chagas Almeida T, Bandeira MCE, Moreira RM, Mattos OR (2015) The role of CO_2 on carbon steel corrosion. NACE - Int Corros Conf 5807.

DeNardis D, Rosales-Yeomans D, Borucki L, Philipossian A (2010) A three-step copper chemical mechanical planarization model including the dissolution effects of a commercial slurry. Thin Solid Films 518:3910–3916

Deshpande S, Kuiry SC, Klimov M (2004) Chemical mechanical planarization of copper: role of oxidants and inhibitors. J Electrochem Soc 151:G788

Devi YG, Adhikari S, Pulikkal AK, Rajaraman PV (2024) Impacts of pyridinium gemini surfactants on corrosion inhibition of carbon steel. Surfaces and Interfaces 45:103796. https://doi.org/10.1016/j.surfin.2023.103796

Dey S, Mishra V, Dhakar N (2024) Probing defect induced room temperature ferromagnetism in Chemical Vapor Deposition grown MoO_3 flakes: A correlation with electronic structure and first principle-based calculations. J Alloys Compd 980. https://doi.org/10.1016/j.jallcom.2024.173650

Dhongde NR, Baranwal PK, Rajaraman PV (2023) Functionalization of graphene oxide with an ionic liquid (1-butyl-3-methylimidazolium acetate): Preparation of epoxy-based coating on carbon steel for anticorrosive applications. J Appl Polym Sci.

https://doi.org/10.1002/app.54026

Dhongde NR, Das NK, Banerjee T, Rajaraman PV (2024) Synthesis of carbon quantum dots from rice husk for anti-corrosive coating applications : Experimental and theoretical investigations. Ind Crop Prod 212:118329. https://doi.org/10.1016/j.indcrop.2024.118329

Du T, Vijayakumar A, Desai V (2004) Effect of hydrogen peroxide on oxidation of copper in CMP slurries containing glycine and Cu ions. Electrochim Acta 49:4505–4512. https://doi.org/10.1016/j.electacta.2004.05.008

Dwivedi D, Lepková K, Becker T (2017) Carbon steel corrosion: a review of key surface properties and characterization methods. RSC Adv 7:4580–4610. https://doi.org/10.1039/C6RA25094G

Dwivedi D, Rowles MR, Becker T, Lepkova K (2020) The role of ferrite-cementite interface in formation of hierarchical film on carbon steel in CO_2-saturated brine. Appl Surf Sci 509:145107. https://doi.org/10.1016/j.apsusc.2019.145107

Ein-Eli Y, Abelev E, Rabkin E, Starosvetsky D (2003) The compatibility of copper CMP slurries with CMP requirements. J Electrochem Soc 150:C646

Elgaddafi R, Naidu A, Ahmed R (2015) Modeling and experimental study of CO_2 corrosion on carbon steel at elevated pressure and temperature. J Nat Gas Sci Eng 27:1620–1629. https://doi.org/10.1016/j.jngse.2015.10.034

Epelboin I, Joussellin M, Wiart R (1981) Impedance measurements for nickel deposition in sulfate and chloride electrolytes. J Electroanal Chem 119:61–71. https://doi.org/10.1016/S0022-0728(81)80124-6

Evans UR (1948) An Introduction to Metallic Corrosion. https://corrosion-doctors.org/Corrosion-History/Theories.htm

Fatah MC, Ismail MC, Ari-Wahjoedi B, Kurnia KA (2011) Effects of sulphide ion on the corrosion behaviour of X52 steel in a carbon dioxide environment at temperature 40 °c. Mater. Chem. Phys. 127:347–352

Fei Chen, Xu Zeng, Jing-Bo Xu, Hai- Sheng Lu X-PQ (2012) The effect of H_2O_2 and ammonia sulphate on the CMP of Molybdenum. ieeexplore.ieee.org 15–17

Fei Chen, Xu Zeng, Jing-Bo Xu, Hai-Sheng Lu X-PQS (2012) The effect of H_2O_2 and Ammonia sulfate on the CMP of Molybdenum. 15–17

Feng H, Cao LA, Feng JY, Qu XP (2015) Effects of colloidal silica on the CMP of Molybdenum in the alkaline slurry. Proc Int Conf Planarization/CMP Technol 66–69. https://doi.org/10.1109/ICPT.2014.7017248

Feng H, Cao LA, Qu XP (2014) Effect of glycine on CMP process of molybdenum. IEEE ICSICT 1–3. https://doi.org/10.1109/ICSICT.2014.7021189

Gao M, Pang X, Gao K (2011) The growth mechanism of CO_2 corrosion product films. Corros Sci 53:557–568

Gao Z, Sun B, Yu Y, (2024) Microstructure, Mechanical, and Tribological Properties of CoCrFeNi-Ag-Mo Self-lubricating Composite. J Mater Eng Perform 33:1704–1717. https://doi.org/10.1007/s11665-023-08085-z

George KS, Nešic S (2007) Investigation of carbon dioxide corrosion of mild steel in the presence of acetic acid - Part 1: Basic mechanisms. Corrosion 63:178–186. https://doi.org/10.5006/1.3278342

Ghelichkhah Z, Srinivasan R, Macdonald DD, Ferguson GS (2023) Anion-catalyzed active dissolution model for the electrochemical adsorption of bisulfate, sulfate, and oxygen on gold in H_2SO_4 solution. Electrochim Acta 439:141515.

https://doi.org/10.1016/j.electacta.2022.141515

Hazarika J, Talukdar A, Rajaraman PV (2023) Effect of oxalic acid (complexing agent) on anodic dissolution of Cobalt in hydrogen peroxide solutions: mechanism and kinetic analysis by electrochemical impedance spectroscopy. J Solid State Electrochem 27:895-909. https://doi.org/10.1007/s10008-023-05379-z

Hazarika J, Talukdar A, Rajaraman PV (2023) Effect of Potassium Iodate-Based Slurry for Polishing of Ruthenium (Ru) as Advanced Interconnects. J Electron Mater 52:6551–6565. https://doi.org/10.1007/s11664-023-10585-6

Hinode K, Owada N, Nishida T, Mukai K (1987) Stress-induced grain boundary fractures in Al–Si interconnects. J Vac Sci Technol B Microelectron Process Phenom 5:518–522. https://doi.org/10.1116/1.583942

Ishfaq M, Rizwan Khan M, Bhopal MF (2014) 1.5MeV proton irradiation effects on electrical and structural properties of TiO_2/n-Si interface. J Appl Phys 115. https://doi.org/10.1063/1.4874942

Itagaki M, Suzuki T, Watanabe K (1998) Anodic dissolution of Fe-Mo in sulfuric acid solution as investigated by electrochemical impedance spectroscopy combined with channel flow double electrode. Corros Sci 40:1255–1265. https://doi.org/10.1016/S0010-938X(97)00121-2

Jeevan Maddala, Krishnaraj Sambath, Vinod Kumar, Ramanathan S (2010) Identification of reaction mechanism for anodic dissolution of metals using Electrochemical Impedance Spectroscopy. J Electroanal Chem 638:183-188. https://doi.org/10.1016/j.jelechem.2009.11.021

Jiang L, He Y, Li Y (2014) Synergetic effect of H_2O_2 and glycine on cobalt CMP in weakly

alkaline slurry. Microelectron Eng 122:82–86. https://doi.org/10.1016/j.mee.2014.02.002

Jiang L, He Y, Li Y, Luo J (2014) Effect of ionic strength on ruthenium CMP in H_2O_2 -based slurries. Appl Surf Sci 317:332–337. https://doi.org/10.1016/j.apsusc.2014.08.063

Jiang L, He Y, Li Y, Luo J (2014) Effect of ionic strength on ruthenium CMP in H_2O_2-based slurries. Appl Surf Sci 317:332–337

Jubault M, Ribeaucourt L, Chassaing E (2011) Optimization of molybdenum thin films for electrodeposited CIGS solar cells. Sol Energy Mater Sol Cells 95:S26–S31. https://doi.org/10.1016/j.solmat.2010.12.011

Kahyarian A, Brown B, Nešić S (2016) Mechanism of cathodic reactions in acetic acid corrosion of iron and mild steel. Corrosion 72:1539–1546

Kahyarian A, Brown B, Nešić S (2020) The Unified Mechanism of Corrosion in Aqueous Weak Acids Solutions: A Review of the Recent Developments in Mechanistic Understandings of Mild Steel Corrosion in the Presence of Carboxylic Acids, Carbon Dioxide, and Hydrogen Sulfide. Corrosion 76:268–278. https://doi.org/10.5006/3474

Kahyarian A, Nesic S (2020) On the mechanism of carbon dioxide corrosion of mild steel: Experimental investigation and mathematical modeling at elevated pressures and non-ideal solutions. Corros Sci 173:108719. https://doi.org/10.1016/j.corsci.2020.108719

Kahyarian A, Nesic S (2019) H_2S corrosion of mild steel: A quantitative analysis of the mechanism of the cathodic reaction. Electrochim Acta 297:676–684. https://doi.org/10.1016/j.electacta.2018.12.029

Kaisare NS, Ramani V, Pushpavanam K, Ramanathan S (2011) An analysis of drifts and nonlinearities in electrochemical impedance spectra. Electrochim Acta 56:7467–7475. https://doi.org/10.1016/j.electacta.2011.06.112

Karimi Abadeh H, Javidi M (2019) Assessment and influence of temperature, NaCl and H_2S on CO_2 corrosion behavior of different microstructures of API 5L X52 carbon steel in aqueous environments. J Nat Gas Sci Eng 67:93–107. https://doi.org/10.1016/j.jngse.2019.04.023

Kelly RG, Scully JR, Shoesmith D, Buchheit RG (2002) Electrochemical Techniques in Corrosion Science and Engineering. Taylor and Francis, Switzerland.

Kermani MB, Harrop D (1996) The impact of corrosion on the oil and gas industry. SPE Prod Facil 11:186–190. https://doi.org/10.2118/29784-PA

Khademi A, Azimirad R, Zavarian AA, Moshfegh AZ (2009) Growth and field emission study of molybdenum oxide nanostars. J Phys Chem C 113:19298–19304. https://doi.org/10.1021/jp9056237

Koch G (2017) Cost of corrosion. Trends in Oil and Gas Reas Tech 3-30. https://doi.org/10.1016/B978-0-08-101105-8.00001-2

Krishnan M, Nalaskowski JW, Cook LM (2010) Chemical mechanical planarization: Slurry chemistry, materials, and mechanisms. Chem Rev 110:178–204. https://doi.org/10.1021/cr900170z

Kumar A, Das C (2024) Corrosion inhibition of mild steel by Praecitrullus fistulosus (tinda fruit and peel) extracts. Sci Total Environ 929:172569. https://doi.org/10.1016/j.scitotenv.2024.172569

Kumar A, Das C (2023) A novel eco-friendly inhibitor of chayote fruit extract for mild steel corrosion in 1 M HCl: Electrochemical, weight loss studies, and the effect of temperature. Sustain Chem Pharm 36:101261. https://doi.org/10.1016/j.scp.2023.101261

Kvarekval J, Dugstad A, Omar IH, Gunaltun Y (2005) H_2S corrosion of carbon steel under

simulated kashagan field conditions. In: NACE CORROSION 05300.

Kvarekvål J, Svenningsen G (2017) Effect of acetic acid on sour corrosion of carbon steel. In: NACE International Corrosion Conference Proceedings 1–14.

Lei Zhang, Wen Zhong, Jianwei Yang, Tan G (2011) Effects Of Temperature And Partial Pressure On H_2S/CO_2 Corrosion Of Pipeline Steel In Sour Conditions. Nace International 1-9. https://doi.org/10.5006/C2011-11079

Li DP, Zhang L, Yang JW (2014) Effect of H2S concentration on the corrosion behavior of pipeline steel under the coexistence of H_2S and CO_2. Int J Miner Metall Mater 21:388–394. https://doi.org/10.1007/s12613-014-0920-y

Li S, Zeng Z, Harris MA (2019) CO_2 corrosion of low carbon steel under the joint effects of time-temperature-salt concentration. Front Mater 6:1–17. https://doi.org/10.3389/fmats.2019.00010

Lianjun Hu, Guofeng Pan, Yi Xu, Hao Wang, Yiwen Zhang, Ru Wang and CW (2020) The Effect of Hydroxyethylidene Diphosphonic Acid on the Chemical Mechanical Polishing of Cobalt in H_2O_2 Based Alkaline Slurries. J Solid State Sci Technol 9. https://doi.org/DOI 10.1149/2162-8777/ab80b2

Lin S, Li H, Xu L (2017) A novel experimental device for electrochemical measurements in supercritical fluids up to 700 °c/1000 bar and its application in the corrosion study of superalloy Inconel 740H. RSC Adv 7:33914–33920. https://doi.org/10.1039/c7ra04054g

Lin Y, Ta L, Meng J (2023) Electrodepositing amorphous molybdenum oxides for aqueous NH^{4+} storage. Chem Commun 59:1481–1484. https://doi.org/10.1039/d2cc06450b

Liu H, Fu C, Gu T (2015) Corrosion behavior of carbon steel in the presence of sulfate reducing bacteria and iron oxidizing bacteria cultured in oilfield produced water. Corros Sci

100:484–495. https://doi.org/10.1016/j.corsci.2015.08.023

Liu J, Yang X, Guo X, Jin Z (2024) Flowered molybdenum base trimetallic oxide decorated by CdS nanorod construct S-scheme heterojunctions for efficient photocatalytic hydrogen evolution. J Mater Sci Technol 196:112–124. https://doi.org/10.1016/j.jmst.2024.01.058

Liu M, Wang J, Ke W (2013) Corrosion behaviour of X52 pipeline steel in high H_2S concentration solutions at temperatures ranging from 25°C to 140°C. Corros Eng Sci Technol 48:380–387. https://doi.org/10.1179/1743278213Y.0000000095

Liu QY, Mao LJ, Zhou SW (2014) Effects of chloride content on CO_2 corrosion of carbon steel in simulated oil and gas well environments. Corros Sci 84:165–171. https://doi.org/10.1016/j.corsci.2014.03.025

Liu Y, Zhong X, Wang Z (2023) Permeating hydrogen generated from the elemental sulfur corrosion of low carbon steel. Corros Sci 213:110987. https://doi.org/10.1016/j.corsci.2023.110987

Liu Z, Gao X, Du L (2017) Comparison of corrosion behaviour of low-alloy pipeline steel exposed to H_2S/CO_2-saturated brine and vapour-saturated H_2S/CO_2 environments. Electrochim Acta 232:528–541. https://doi.org/10.1016/j.electacta.2017.02.114

López DA, Schreiner WH, De Sánchez SR, Simison SN (2003) The influence of carbon steel microstructure on corrosion layers: An XPS and SEM characterization. Appl Surf Sci 207:69–85. https://doi.org/10.1016/S0169-4332(02)01218-7

Losey MW, Kelly JJ, Badgayan ND, Sahu S K, Rama Sreekanth R (2017) Electrodeposition. Ref Mof Mat Sc Mat Eng 271-292. https://doi.org/10.1016/B978-0-12-803581-8.10137-7

Lukács Z, Kristóf T (2020) A generalized model of the equivalent circuits in the

electrochemical impedance spectroscopy. Electrochim Acta 363:. https://doi.org/10.1016/j.electacta.2020.137199

M. Ürgen,U Stolz, R Kirchheim (1990) ESCA measurements of films on molybdenum formed in the passive and transpassive region. Corros Sci 30:377–391. https://doi.org/https://doi.org/10.1016/0010-938X(90)90045-7

Ma H, Cheng X, Li G (2000) The influence of hydrogen sulfide on corrosion of iron under different conditions. Corros Sci 42:1669–1683

Madani Sani F, Brown B, Nesic S (2021) An Electrochemical Study of the Effect of High Salt Concentration on Uniform Corrosion of Carbon Steel in Aqueous CO_2 Solutions . J Electrochem Soc 168:051501. https://doi.org/10.1149/1945-7111/abf5f9

Maheswari N, Muralidharan G (2017) Controlled synthesis of nanostructured molybdenum oxide electrodes for high performance supercapacitor devices. Appl Surf Sci 416:461–469. https://doi.org/10.1016/j.apsusc.2017.04.094

Mars G. Fontana (1987) Corrosion Engineering. Mc Graw Hill, Singapore.

Micheal N Hull (1972) on the Anodic Dissolution of Molybdenum in Acidic and Alkaline Electrolytes. J Electroanal chem interf electrochem 38:143–157. https://doi.org/https://doi.org/10.1016/S0022-0728(72)80100-1

Morgan DJ (2021) Comments on the XPS Analysis of Carbon Materials. C 7:51. https://doi.org/10.3390/c7030051

Mueller-Harvey I, John Parkes R (1987) Measurement of volatile fatty acids in pore water from marine sediments by HPLC. Estuar Coast Shelf Sci 25:567–579. https://doi.org/10.1016/0272-7714(87)90115-6

Elaine B, (2016) International Measures of Prevention, Application, and Economics of Corrosion Technologies Study. NACE International 3.

Nagendra Prasad Y, Vinod Kumar V, Ramanathan S (2009) Electrochemical impedance spectroscopic studies of copper dissolution in arginine-hydrogen peroxide solutions. J Solid State Electrochem 13:1351–1359. https://doi.org/10.1007/s10008-008-0682-4

Nam T, Colleran TA, Partridge JL (2024) Thermal Atomic Layer Etching of Molybdenum Using Sequential Oxidation and Deoxychlorination Reactions. Chem Mater 36:1449–1458. https://doi.org/10.1021/acs.chemmater.3c02606

Nešić S, Li H, Huang J, Sormaz D (2009) An open source mechanistic model for CO_2 / H_2S corrosion of carbon steel. NACE - Int Corros Conf Ser 1-19. https://doi.org/10.5006/C2009-09572

Nor AM, Suhor MF, Mohamed MF, Nesic S (2011) Corrosion of carbon steel in high CO_2 environment: flow effect.Nace International 1-18. https://doi.org/10.5006/C2011-11242

Obot IB, Onyeachu IB (2018) Electrochemical frequency modulation (EFM) technique: Theory and recent practical applications in corrosion research. J Mol Liq 249:83–96

Ochoa N, Vega C, Pébère N (2015) CO_2 corrosion resistance of carbon steel in relation with microstructure changes. Mater Chem Phys 156:198–205. https://doi.org/10.1016/j.matchemphys.2015.02.047

Okafor PC, Brown B, Nesic S (2009) CO_2 corrosion of carbon steel in the presence of acetic acid at higher temperatures. J Appl Electrochem 39:873–877. https://doi.org/10.1007/s10800-008-9733-x

Okafor PC, Nesic S (2007) Effect of acetic acid on CO_2 corrosion of carbon steel in vapor-water two-phase horizontal flow. Chem Eng Commun 194:141–157.

https://doi.org/10.1080/00986440600642975

Okonkwo PC, Shakoor RA, Benamor A (2017) Corrosion behavior of API X100 steel material in a hydrogen sulfide environment. Metals (Basel) 7:8–11. https://doi.org/10.3390/met7040109

Olvera-Martínez ME, Mendoza-Flores J, Rodríguez-Gómez FJ (2018) Assessment of the effects of acetic acid and turbulent flow conditions on the corrosion of API 5L X52 steel in aqueous CO_2 solutions. Mater Corros 69:376–385. https://doi.org/10.1002/maco.201709736

Ozawa K (1993) Mechanical properties of Al and Al alloys and their relationship to interconnection reliability. J Appl Phys 73:977–985. https://doi.org/10.1063/1.353312

Palaparthi R, Muldowney G (2006) An Experimental Characterization of Dissolution and Complexation Kinetics in Copper CMP. ECS Meet Abstr MA2006-01:475–475. https://doi.org/10.1149/ma2006-01/10/475

Pan Y, Sun B, Chen H (2024) Stress corrosion cracking behavior and mechanism of 2205 duplex stainless steel under applied polarization potentials. Corros Sci 231:. https://doi.org/10.1016/j.corsci.2024.111978

Paul E, Kaufman F, Brusic V (2005) A model of copper CMP. J Electrochem Soc 152:G322

Paul T, Srinivasan R (2020) Mechanistic analysis of anodic dissolution of cobalt in alkaline glycine solution. J Sol. St Electrochem 1291–1304.

Peethala BC, Babu S V. (2011) Ruthenium Polishing Using Potassium Periodate as the Oxidizer and Silica Abrasives. J Electrochem Soc 158:H271. https://doi.org/10.1149/1.3528942

Pensado O, Urquidi-Macdonald M, Macdonald DD (2001) Electrochemical Behavior of Lithium in Alkaline Aqueous Electrolytes: III. Impedance Model. J Electrochem Soc 148:B386. https://doi.org/10.1149/1.1401085

Perez N Nestor Perez (2004) Electrochemistry and Corrosion Science. Springer, Switzerland.

Pessu F, Hua Y, Barker R, Neville A (2016) An investigation of the overall corrosion behaviour of X65 (UNS K03014) carbon steel in different H_2S-CO_2-containing environments. NACE CORROSION 7643.

Prasad YN, Ramanathan S (2007) Chemical mechanical planarization of copper in alkaline slurry with uric acid as inhibitor. Electrochim Acta 52:6353–6358. https://doi.org/10.1016/j.electacta.2007.04.044

Qi Y, Luo H, Zheng S (2014) Effect of H_2S partial pressure on the tensile properties of A350LF2 steel in the absence and presence of pre-immersion. Mater Sci Eng A 609:161–167. https://doi.org/10.1016/j.msea.2014.04.068

Qi Y, Luo H, Zheng S (2014) Effect of temperature on the corrosion behavior of carbon steel in hydrogen sulphide environments. Int J Electrochem Sci 9:2101–2112.

Qu X-P, Yang G, He P, Feng H (2017) Chemical Mechanical Polishing of Mo Using H_2O_2 as Oxidizer in Colloidal Silica Based Slurries. ECS J Solid State Sci Technol 6:P470–P476. https://doi.org/10.1149/2.0351707jss

Quej-Ake LM, Contreras A, Liu HB (2018) Assessment on external corrosion rates for API pipeline steels exposed to acidic sand-clay soil. Anti-Corrosion Methods Mater 65:281–291. https://doi.org/10.1108/ACMM-12-2017-1874

Ramanathan Srinivasan, Fathima F (2021) An Introduction to Electrochemical Impedance Spectroscopy. CRC Press, Boca Raton.

Ranjith PM, Rao MT, Sapra S (2018) On the Anodic Dissolution of Tantalum and Niobium in Hydrofluoric Acid. J Electrochem Soc 165:C258–C269. https://doi.org/10.1149/2.0691805jes

Reddy RKK, Kailasa S, Rani BG (2019) Hydrothermal approached 1-D molybdenum oxide nanostructures for high-performance supercapacitor application. SN Appl Sci 1:1–9. https://doi.org/10.1007/s42452-019-1295-5

Ren C, Liu D, Bai Z, Li T (2005) Corrosion behavior of oil tube steel in simulant solution with hydrogen sulfide and carbon dioxide. Mater Chem Phys 93:305–309

Revilla RI, Wouters B, Andreatta F (2020) EIS comparative study and critical Equivalent Electrical Circuit (EEC) analysis of the native oxide layer of additive manufactured and wrought 316L stainless steel. Corros Sci 167:108480. https://doi.org/10.1016/j.corsci.2020.108480

Rihan RO (2013) Electrochemical corrosion behavior of X52 and X60 Steels in carbon dioxide containing saltwater solution. Mater Res 16:227–236. https://doi.org/10.1590/S1516-14392012005000170

Rizzo R, Gupta S, Rogowska M, Ambat R (2020) Corrosion of carbon steel under CO_2 conditions: Effect of $CaCO_3$ precipitation on the stability of the $FeCO_3$ protective layer. Corros Sci 162:. https://doi.org/10.1016/j.corsci.2019.108214

Rustandi A, Adhika N, Prima T, Aziz N (2013) Behavior of CO_2 corrosion of API 5L X52 steel in NaCl solution under turbulent flow condition. Adv Mater Res 789:476–483. https://doi.org/10.4028/www.scientific.net/AMR.789.476

Ryu H-Y, Teugels L, Devriendt K (2021) Effects of H_2O_2 and pH on the Chemical Mechanical Planarization of Molybdenum. ECS J Solid State Sci Technol 10:094001.

https://doi.org/10.1149/2162-8777/ac26d3

Sagi K V., Amanapu HP, Alety SR, Babu S V. (2016) Potassium Permanganate-Based Slurry to Reduce the Galvanic Corrosion of the Cu/Ru/TiN Barrier Liner Stack during CMP in the BEOL Interconnects. ECS J Solid State Sci Technol 5:P256–P263. https://doi.org/10.1149/2.0141605jss

Sahrani FK, Aziz M, Ibrahim Z, Yahya A (2008) Open circuit potential study of stainless steel in environment containing marine sulphate-reducing bacteria. Sains Malaysiana 37:359–364

Saji VS, Lee CW (2012) Molybdenum, molybdenum oxides, and their electrochemistry. ChemSusChem 5:1146–1161. https://doi.org/10.1002/cssc.201100660

Santos R., Lo (2014) An overview of heavy oil properties and its recovery and transportation methods. Brazilian J Chem Eng 31:571–590

Schonbein C (1936) Schönbein C. Pogg Ann 390:37

Schroeder T, Zegenhagen J, Magg N (2004) Formation of a faceted MoO_2 epilayer on Mo(112) studied by XPS, UPS and STM. Surf Sci 552:85–97. https://doi.org/10.1016/j.susc.2004.01.010

Seo HS, Bae JU, Kim DH (2009) Reliable bottom gate amorphous indium-gallium-zinc oxide thin-film transistors with TiOx passivation layer. Electrochem Solid-State Lett 12:348–351. https://doi.org/10.1149/1.3168522

Seo YJ, Lee WS (2005) Effects of different oxidizers on the W-CMP performance. Mater Sci Eng B Solid-State Mater Adv Technol 118:281–284. https://doi.org/10.1016/j.mseb.2004.12.064

Shoesmith DW, Taylor P, Bailey MG, Owen DG (1980) The Formation of Ferrous Monosulfide Polymorphs during the Corrosion of Iron by Aqueous Hydrogen Sulfide at 21°C. J Electrochem Soc 127:1007–1015. https://doi.org/10.1149/1.2129808

Singh A, Ansari KR, Chauhan DS (2020) Comprehensive investigation of steel corrosion inhibition at macro/micro level by ecofriendly green corrosion inhibitor in 15% HCl medium. J Colloid Interface Sci 560:225–236. https://doi.org/10.1016/j.jcis.2019.10.040

Singh MM, Gupta A (2000) Corrosion behavior of mild steel in acetic acid solutions. Corrosion 56:371–379

Singh SK, Mukherjee AK (2010) Kinetics of mild steel corrosion in aqueous acetic acid solutions. J Mater Sci Technol 26:264–269. https://doi.org/10.1016/S1005-0302(10)60044-8

Song X, Chen Q, Shen E, Liu H (2019) Supercapacitive performances of few-layer MoS_2 on reduced graphene oxides. J Solid State Electrochem 23:911–923. https://doi.org/10.1007/s10008-019-04195-8

Steigerwald JM, Murarka SP, Gutmann RJ (1997) Chemical Mechanical Planarization of Microelectronic Materials. Wiley, Germany.

Talukdar A, Baranwal PK, Rajaraman PV (2022) Kinetics and mechanistic reaction pathway of carbon steel dissolution in simulated CO_2-H_2S medium in the presence of formic acid. Corros Rev 40:159–172. https://doi.org/10.1515/corrrev-2021-0062

Talukdar A, Baranwal PK, Talukdar MK, Rajaraman PV (2023) Synergistic Effect of H_2S and Acetic Acid on CO_2 Corrosion of Carbon Steel at Elevated Temperature. Jom 75:3757–3770. https://doi.org/10.1007/s11837-023-05952-x

Talukdar A, Rajaraman PV (2020) Investigation of Acetic Acid Effect on Carbon Steel

Corrosion in CO_2-H_2S Medium: Mechanistic Reaction Pathway and Kinetics. ACS Omega 5:11378–11388. https://doi.org/10.1021/acsomega.0c00387

Tang J, Shao Y, Guo J (2010) The effect of H_2S concentration on the corrosion behavior of carbon steel at 90 °C. Corros Sci 52:2050–2058. https://doi.org/10.1016/j.corsci.2010.02.004

Tibbetts PJC, Buchanan IT, Gawel LJ, Large R (1992) A Comprehensive Determination of Produced Water Composition. Prod Water 97–112. https://doi.org/10.1007/978-1-4615-2902-6_9

Tran T, Brown B, Nesic S, Tribollet B (2013) Investigation of the mechanism for acetic acid corrosion of mild steel. NACE - Int Corros Conf Ser 1–12

Tran T, Brown B, Nešić S, Tribollet B (2014) Investigation of the electrochemical mechanisms for acetic acid corrosion of mild steel. Corrosion 70:223–229. https://doi.org/10.5006/0933

Turk MC, Rock SE, Amanapu HP (2013) Investigation of Percarbonate Based Slurry Chemistry for Controlling Galvanic Corrosion during CMP of Ruthenium. ECS J Solid State Sci Technol 2:P205–P213. https://doi.org/10.1149/2.009305jss

Varol Özkavak H (2024) Wear Resistance, Hardness, and Residual Stress of Shot-Peened and Heat-Treated 8620 Nickel-Chromium-Molybdenum Steel. J Mater Eng Perform. https://doi.org/10.1007/s11665-023-09110-x

Veloz MA, González I (2002) Electrochemical study of carbon steel corrosion in buffered acetic acid solutions with chlorides and H_2S. Electrochim Acta 48:135–144. https://doi.org/10.1016/S0013-4686(02)00549-2

Venkatesh RP, Ramanathan S (2010) Electrochemical characterization of Cu dissolution and

chemical mechanical polishing in ammonium hydroxide-hydrogen peroxide based slurries. J Appl Electrochem 40:767–776. https://doi.org/10.1007/s10800-009-0055-4

Walser H, Knabl W, McCrossan S (2011) Traditional and new applications of Molybdenum metal and alloys. Proc 8th Int Conf Tungsten, Refract Hardmaterials 108:81–811

Walsh FC (1992) Faraday and his laws of electrolysis: An appreciation. Bull Electrochem 7:481–484

Wang J (2006) Analytical electrochemistry. Wiley, Canada.

Wang L, Peng F, Chen H (2023a) The influence of pH and H_2O_2 on surface quality and material removal rate during W-CMP. Int J Adv Manuf Technol 127:4097–4110. https://doi.org/10.1007/s00170-023-11805-3

Wang L, Wang H, Seyeux A (2023) Adsorption mechanism of quaternary ammonium corrosion inhibitor on carbon steel surface using ToF-SIMS and XPS. Corros Sci 213:110952. https://doi.org/10.1016/j.corsci.2022.110952

Wang S, Chen L, Wang H (2024) The synthesis and tribological behaviour of a phosphorus-free triazine organic molybdenum as friction modifier. J Mol Liq 409:125498. https://doi.org/10.1016/j.molliq.2024.125498

Wei L, Pang X, Gao K (2016) Effect of small amount of H_2S on the corrosion behavior of carbon steel in the dynamic supercritical CO_2 environments. Corros Sci 103:132–144

Wen X, Bai P, Luo B (2018) Review of recent progress in the study of corrosion products of steels in a hydrogen sulphide environment. Corros Sci 139:124–140. https://doi.org/10.1016/j.corsci.2018.05.002

Xie F, Choy WCH, Wang C (2013) Low-temperature solution-processed hydrogen

molybdenum and vanadium bronzes for an efficient hole-transport layer in organic electronics. Adv Mater 25:2051–2055. https://doi.org/10.1002/adma.201204425

Xu G, Liang H, Zhao J, Li Y (2004) Investigation of copper removal mechanisms during CMP. J Electrochem Soc 151:G688

Xu M, Liang H, Liu Y, Asselin E (2021) Predicting the external corrosion rate of X60 pipeline steel: A mathematical model. Metals (Basel) 11:1–19. https://doi.org/10.3390/met11040583

Xu Q, Chen L, Yang F, Cao H (2017) Influence of slurry components on copper CMP performance in alkaline slurry. Microelectron Eng 183:1–11

Yang G, He P, Qu XP (2018) Inhibition effect of glycine on molybdenum corrosion during CMP in alkaline H_2O_2-based abrasive-free slurry. Appl Surf Sci 427:148–155. https://doi.org/10.1016/j.apsusc.2017.08.140

Yang S, Zhang K, Wang C(2017) Hierarchical 1T-MoS_2 nanotubular structures for enhanced supercapacitive performance. J Mater Chem A 5:23704–23711. https://doi.org/10.1039/c7ta08115d

Yaro AS, Abdul-Khalik KR, Khadom AA (2015) Effect of CO_2 corrosion behavior of mild steel in oilfield produced water. J Loss Prev Process Ind 38:24–38. https://doi.org/10.1016/j.jlp.2015.08.003

Yin ZF, Feng YR, Zhao WZ (2009) Effect of temperature on CO_2 corrosion of carbon steel. Surf Interface Anal 41:517–523. https://doi.org/10.1002/sia.3057

Yin ZF, Zhao WZ, Bai ZQ (2008) Corrosion behavior of SM 80SS tube steel in stimulant solution containing H_2S and CO_2. Electrochim Acta 53:3690–3700

Yoshida Y, Uemura T (1994) Properties and Applications of Molybdenum. ASTM Int 443–450. https://doi.org/10.1016/b978-0-444-81708-2.50049-x

Yu Z, Yan H, Wang C (2023) Oxygen-deficient MoOx/Ni_3S_2 heterostructure grown on nickel foam as efficient and durable self-supported electrocatalysts for hydrogen evolution reaction. Front Chem Sci Eng 17:437–448. https://doi.org/10.1007/s11705-022-2228-1

Zachowski EJ, Wojciechowski M, Osteryoung J (1985) Analytical Application of Square Wave Voltammetry. Electrochem Soc Ext Abstr 85–1:877

Zaludin MAF, Jamal ZAZ, Derman MN, Kasmuin MZ (2019) Corrosion analysis of hydroxyapatite coated magnesium in simulated body fluid (SBF), phosphate buffered saline (PBS), and Ringer's solution. Mater Today Proc 16:1686–1691

Zhang S, Li Y, Liu B (2022) Understanding the synergistic effect of CO_2, H_2S and fluid flow towards carbon steel corrosion. Vacuum 196:110790. https://doi.org/10.1016/j.vacuum.2021.110790

Zhao MC, Tang B, Shan YY, Yang K (2003) Role of microstructure on sulfide stress cracking of oil and gas pipeline steels. Metall Mater Trans A Phys Metall Mater Sci 34 A:1089–1096. https://doi.org/10.1007/s11661-003-0128-7

(2012) Standard guide for laboratory immersion corrosion testing of metals. ASTM NACE

Appendix

The reaction of generation of H_2S gas from thiosulfate

$$S_2O_3^{2-} + H^+ + e^- \rightarrow S + 3HSO_3^{2-} \quad \textbf{(A1)}$$

$$S_2O_3^{2-} + 6H^+ + 4e^- \rightarrow 2S + 3H_2O \quad \textbf{(A2)}$$

$$S + 2H^+ + 4e^- \rightarrow H_2S \quad \textbf{(A3)}$$

$$4S + 4H_2O \rightarrow H_2S + HSO_4^- + H^+ \quad \textbf{(A4)}$$

Bode-phase plots

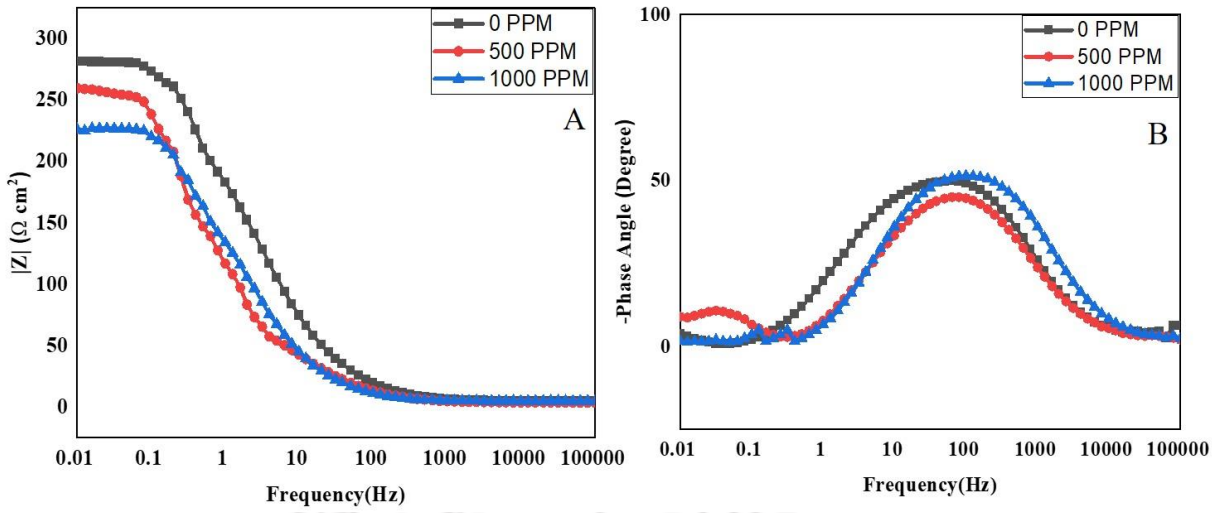

Figure A1 (A) Bode plot and (B) phase angle plot obtained from EIS for carbon steel X52 obtained in 3.5 wt. % CO_2-H_2S system at varying acetic acid concentrations (0,500,1000 ppm) at 40 ºC

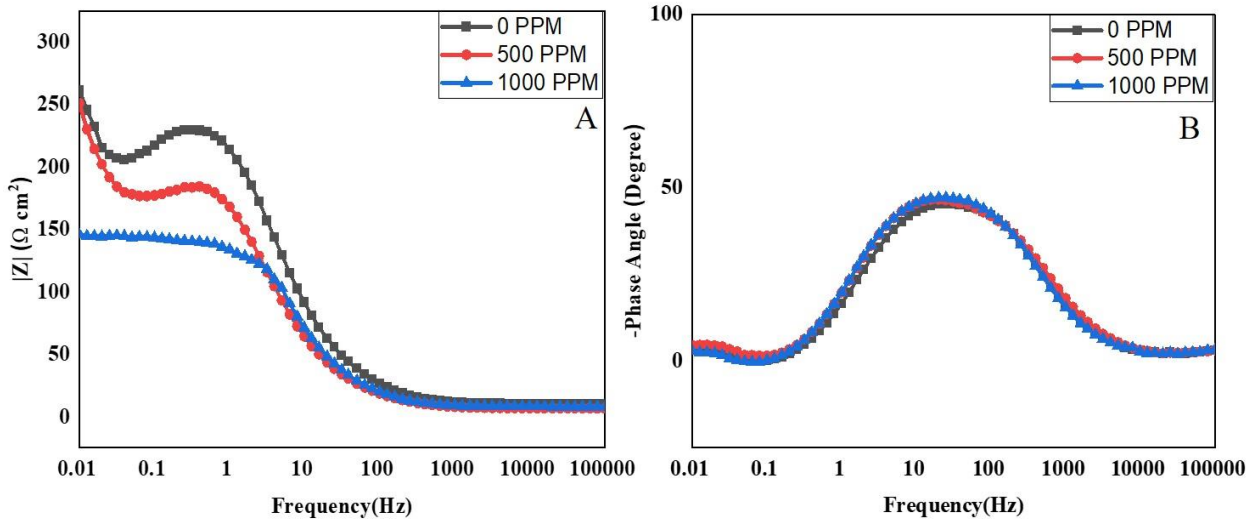

Figure A2 (A) Bode plot and (B) phase angle plot obtained from EIS for carbon steel X60 obtained in 3.5 wt. % CO_2-H_2S system at varying acetic acid concentrations (0,500,1000 ppm) at 40 ºC

RESEARCH OUTCOME FROM THE THESIS

In Journals from this work

1. **Sayani Adhikari,** Nikhil Dhongde, Mausmi Kakoti Talukdar, Srimoyee Khan, Prasanna Venkatesh Rajaraman, Investigation of carbon steels (API 5L X52 and API 5L X60) dissolution CO_2- H_2S solutions in the presence of acetic acid: mechanistic reaction pathway and kinetics, **Arabian Journal of Science and Engineering** 49 (2024): 8363-8381.
2. **Sayani Adhikari,** Prasanna Venkatesh Rajaraman, Investigation on Anodic Dissolution of Mo in alkaline solutions containing Oxidizer (H_2O_2) via Electrochemical Impedance Spectroscopy: Mechanistic and Kinetic Analysis, **Journal of Materials Performance and Engineering**, (2025): 1-13.
3. **Sayani Adhikari,** Prasanna Venkatesh Rajaraman, Anodic Dissolution of Molybdenum in Potassium Permanganate Solution by Electrochemical Impedance Spectroscopy: Reaction Kinetics. (Manuscript under preparation)

In Journals from other work:

4. Yumnam Gyani Devi, **Sayani Adhikari**, Ajmal Koya Pulikkal, Prasanna Venkatesh Rajaraman, Impacts of pyridinium gemini surfactants on corrosion inhibition of carbon steel, **Surfaces and Interfaces** 45 (2024): 103796.
5. Nikhil Rahul Dhongde, **Sayani Adhikari**, Prasanna Venkatesh Rajaraman, Anticorrosion properties of ionic liquid functionalized graphene oxide epoxy composite coating on the carbon steel for CCUS environment, **Environmental Science and Pollution Research** 32 (2025), 4511-4522.

In Conference

1. **Sayani Adhikari**, Vinay Kumar, Prasanna Venkatesh Rajaraman, Dissolution mechanism analysis of molybdenum in KMnO4 solution, International conference on corrosion and coatings (December, 7-8 2022), Jamshedpur, India
2. **Sayani Adhikari**, Prasanna Venkatesh Rajaraman, Anodic dissolution mechanism of molybdenum in the presence of oxidizer by reaction mechanism analysis, International conference on petroleum, hydrogen and decarbonization, (November, 3-5 2023), IIT Guwahati, India
3. **Sayani Adhikari**, Nikhil Dhongde, Mausmi Kakoti Talukdar, Srimoyee Khan, Prasanna Venkatesh Rajaraman, Carbon Steels (API 5L X52 And API 5L X60) Sweet Corrosion in the Presence of Acetic Acid: Kinetic Parameters Determination from EIS Data at Lower Overpotentials, 3rd International Conference on New Frontiers in Chemical, Energy and Environmental Engineering (November 23-24, 2023), NIT Warangal, India

Workshop

1. Applied statistical modelling and data analytics for petroleum engineering and related applications held at Indian Institute of Technology Guwahati, Assam, India from 22-24 November 2022, and sponsored by SPE IIT Guwahati student chapter.